Quantitative measurements of temperature using laser-induced thermal grating spectroscopy in reacting and non-reacting flows

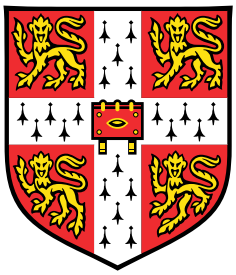

Steven M. Lowe

Department of Engineering

University of Cambridge

This dissertation is submitted for the degree of

Doctor of Philosophy

Clare College June 2018

Declaration

I hereby declare that except where specific reference is made to the work of others, the contents of this dissertation are original and have not been submitted in whole or in part for consideration for any other degree or qualification in this, or any other university. This dissertation is my own work and contains nothing which is the outcome of work done in collaboration with others, except as specified in the text and Acknowledgements. This dissertation contains fewer than 65,000 words including appendices, bibliography, footnotes, tables and equations and has fewer than 150 figures.

Steven M. Lowe

June 2018

Acknowledgements

I would like to take this opportunity to thank the great many people who have been so instrumental in helping me through this research endeavour.

First and foremost, I would like to express my gratitude to my supervisor, Prof. Simone Hochgreb, for providing me with the opportunity to gain this invaluable experience under her tutelage. Her guidance and support during this challenging and exciting research project has been hugely appreciated. I also thank my advisor, Prof. Stuart Cant, for his additional support, insight and calming perspective. I am extremely grateful to Prof. Hideaki Kobayashi, Dr. Akihiro Hayakawa and other members of the Kobayashi group in the Institute of Fluid Sciences for their great effort in making our collaboration a success and giving me the opportunity to perform experiments in Japan. My thanks is also extended to our collaborators at Oxford University – Prof. Paul Ewart, Dr. Ben Williams and Andrew Leurs for introducing our lab to the science of laser induced gratings and the stimulating discussions on the topic.

To all my friends and colleagues in the Hopkinson laboratory, thank you for the added insight, motivation and support over the years. In particular, I thank Yi Gao for her great patience and the many memories in the lab. I'd also like to thank Saravannan, Bo, Francesca, Luming, Lee, Erwan, Cen, James, Nick, Golnoush, Jenni, Pedro, Patton and Anh-Koa for all their support in various forms. Our discussions on topics ranging from spectroscopy to Spurs have kept me going. To the workshop staff (Mick, Roy, Rob, John, Ken and Mark), thank you for putting up with me and for the relentless banter. I also reserve a special thank you for the one they call my 'chuckle brother' – Mustafa Kamal. The late night talks and endless cups of tea were as motivating as they were memorable and I am grateful for your friendship.

To my close friends outside of the lab who have provided me with incredible support over the last few years, I can't thank you enough. Navjot Sawhney and Robyn Skelton, vast geographical distances and awkward time-zones have never been a match for your care. The 4am calls helped me through some tough times and won't be forgotten. Felix Stein, thank you for the constant encouragement. I know you've always wanted to visit Sendai. Christian Hampel, thanks for never failing to make me laugh and always providing me with wise words over the years. Freddie Dudbridge, thanks for dragging me back to Tottenham whenever I've needed it (COYS). Rebecca Broome, your understanding and uplifting nature has really made this process that little bit easier. Thank you so much.

Finally, thanks to my grandparents, Manoli and Najieh Oweis and Jillian Smith; my brother, Samuel Lowe, and his wife, Laura; and my parents, Andrew and Naziha Lowe. Your immeasurable love and inspiration have carried me through this and whilst I can never truly express what you have done for me, at least this work bears each of your names. I dedicate this thesis to you.

Contributions to this thesis

The following is a list of the significant areas where I have used the results of (or otherwise incorporated) work done by others:

- ChemKin flame simulations were performed by Hayakawa A. (IFS, Tohoku University).
- OH-PLIF data in Chapter 5 was provided by Hayakawa, A. and Yamagami, T.

Abstract

Title: Quantitative measurements of temperature using laser-induced thermal grating spectroscopy in reacting and non-reacting flows

Name: Steven M. Lowe

This thesis is concerned with the development and application of laser induced thermal grating spectroscopy (LITGS) as a tool for thermometry in reacting and non-reacting flows. LITGS signals, which require resonant excitation of an absorbing species in the measurement region to produce a thermal grating, are acquired for systematic measurements of temperature in high pressure flames using OH and NO as target absorbing species in the burned gas. The signal obtained in LITGS measurements appears in the form of a time-based signal with a characteristic frequency proportional to the value or the sound speed of the local medium. With knowledge of the gas composition, the temperature can be derived from the speed of sound measurement.

LITGS thermometry using resonant excitation of OH in the burned gas region of in oxygen enriched $CH_4/O_2/N_2$ and CH_4/air laminar flames was performed at elevated pressure (0.5 MPa) for a range of conditions. Measurements were acquired in oxygen enriched flames to provide an environment in which to demonstrate LITGS thermometry under high temperature conditions (up to 2900 K). The primary parameters that

influence the quality of LITGS signal were also investigated. The signal contrast, which acts as a marker for the strength of the frequency oscillations, is shown to increase with an increase in the burnt gas density at the measurement point.

LITGS employing resonant excitation of NO is also demonstrated for quantitative measurements of temperature in three environments – a static pressure cell at ambient temperature, a non-reacting heated jet at ambient pressure and a laminar premixed CH_4/NH_3/air flame operating at 0.5 MPa. Flame temperature measurements were acquired at various locations in the burned gas close to a water-cooled stagnation plate, demonstrating the capability of NO-LITGS thermometry for measuring the spatial distribution of temperature in combustion environments.

In addition, the parameters that influence the local temperature rise due to LITGS were also investigated in continuous vapour flows of acetone/air and toluene/air mixtures at atmospheric conditions. Acetone and toluene are commonly targeted species in previous LITGS measurements due to their favourable absorption characteristics. Results indicate that LITGS has the potential to produce accurate and precise measurements of temperature in non-reacting flows, but that the product of the pump intensity at the probe volume and the absorber concentration must remain relatively low to avoid significant localised heating of the measurement region.

Table of contents

List of figures

List of tables

Nomenclature

Symbols

σ	Absorption cross section
τ	Acoustic wave transit time
$\mathbf{E}$	Applied electric field
z	Axial distance from base of burner
d_f	Beam diameter at focal point
θ_{br}	Bragg angle
k_B	Boltzmann's constant
ρ	Density (kgm^{-3})
ρ_0	Density at static (non-excited state) conditions (kgm^{-3})
d	distance between pump beams, beam spot size
A	Einstein coefficient for absorption
B	Einstein coefficient for spontaneous emission
Φ	Equivalence ratio
v	Frequency of associated electromagnetic wave
Λ	Grating fringe spacing
I_R	Intensity of scattered Rayleigh signal
I_0	Incident laser intensity

L	Length g Laser pulse temporal profile
E_p	Laser energy per pulse
τ_L	Laser pulse duration
f	Lens focal length
ΔT_m	Maximum temperature rise
W	Mean molecular weight
X_v	Mole fraction of absorbing species
ζ	Non-dimensional time
ξ	Non-dimensional length or flow rate ratio
ρ'	Normalized density fluctuation
P'	Normalized pressure fluctuation
u'	Normalized velocity fluctuation
N^*	Number density of excited molecules
$N_{\alpha 0}$	Number density of absorbing species
f	Oscillation frequency
ε_0	Permittivity of free space
$\mathbf{P}$	Polarization vector
θ	Pump beam crossing angle
λ_1	Pump beam wavelength
λ_2	Probe beam wavelength
P_0	Pressure at static (non-excited state) conditions (Pa)
p	Pressure (Pa)
h	Planck's constant
Pr	Prandtl number
τ_L	Pulse duration
Q	Quenching rate

γ	Ratio of specific heat capacities
σ_i	Rayleigh cross-section for species, i
Re	Reynolds number
C_p	Specific heat at constant pressure
χ	Susceptibility
c	Speed of light
c_s	Speed of sound
t	Time (s)
T	Temperature (K)
T_0	Thermocouple temperature
ΔT	Temperature rise
$W(\zeta)$	Temporal response of the medium to an instantaneous input of thermal energy
Vu	Velocity
ω	Wavelength
$\vec{k_i}$	Wave vector of ith electromagnetic field

Chapter 1

Introduction

1.1 Motivation

One of the greatest social, environmental and economic challenges that mankind is currently facing is the nature of energy conversion and efficiency. Power generation by means of burning fossil fuels hinges on the energy conversion process - or more specifically (for most industrial applications), combustion. Whilst a great deal of attention has been focused on renewable energy resources by means of solar and wind power [102] [115], it is clear that combustion systems will remain a dominant source of power generation for a significant period of time.

Combustion systems are intrinsically linked to environmentally harmful emissions, including greenhouse gases (such as CO_2), nitric oxides (NO_x), sulphuric oxides (SO_x), unburned hydrocarbons and particulate matter. Increased scientific, social and political awareness surrounding the environmental impact of such emissions has led to progressively more stringent emissions targets, with the most recent major political

negotiations held in Paris leading to ambitious global warming and air quality targets [133].

These increasingly stringent targets have prompted research, in both academic and industrial settings, into the development of combustion systems that improve fuel efficiency, leading to more sustainable consumption of fossil fuels, and minimise pollutant emissions. A knowledge of the fundamental processes that influence combustion physics is of crucial importance for informing how to go about improving such systems. Understanding the complex nature of combustion requires an understanding of how combustion chemistry, fluid mechanics and heat and mass transfer interact to influence important parameters that define how clean and efficient the system is [86]. Influential parameters can include the flame structure, stability, temperature and species concentration, to name just a few. Whilst approaches to theoretical and computational modeling have improved vastly in recent decades, there is still a significant need for accurate and precise experimental data to validate models and inform future approaches to simulating reacting flows.

This thesis is primarily concerned with the development of non-intrusive, laser-based diagnostics, specifically in the context of improved measurements of temperature in both non-reacting flows and high temperature, high pressure combustion. Temperature is considered to be one of the most important scalar parameters in combustion research given its strong influence on most chemical reactions in a flame, which ultimately govern heat release and the formation of pollutants, particularly nitric oxide [126].

Furthermore, in high temperature combustion applications (e.g. oxygen-enriched combustion [123], rocket motor combustion [120], discussed in further detail in Chapter 5), the peak temperature gives rise to thermal stresses which affect the mechanical structure of the combustion chamber. Hence, accurate and precise measurements of

temperature are of vital importance in informing a number of aspects of the next generation of combustor design.

1.2 Objectives

The overall objective of this project is to demonstrate the potential for accurate and precise measurements of temperature using laser induced thermal grating spectroscopy (LITGS) in both reacting and non-reacting flows. More specifically, the project aims to both investigate the parameters that affect the LITGS signal and measurement accuracy, and demonstrate the capability of the technique in obtaining accurate measurements in under a range of high temperature and high pressure combustion conditions using various absorbing species.

In summary, the objectives are to:

(i) Demonstrate the LITGS technique for quantitative measurements of temperature in both non-reacting and reacting flows.

(ii) Quantify the parameters that affect the local temperature rise within the probe volume associated with LITGS measurements for popular absorbing species.

(iii) Investigate the potential for LITGS measurements using absorbing species that are found in flames (i.e. OH, NO) under a range of temperatures and pressures.

(iv) Demonstrate the capability of OH-LITGS for measurements of temperature in oxygen-enhanced (high temperature), high pressure flames.

(v) Demonstrate the capability of NO-LITGS for measurements of temperature in methane-ammonia (low CO_2) flames at high pressure.

1.3 Thesis structure

The present chapter provides a general introduction to the importance of precise and accurate temperature measurements in combustion as a motivation for work on developmental diagnostics. Chapter 2 contains a discussion of the relevant literature associated with the LITGS technique, starting with a review of the established laser based methods for temperature measurements in flames, including details of their benefits and limitations. The specific theoretical operating principles behind the LITGS technique are then introduced, along with a review of the literature that presents the implementation of the technique in both reacting and non-reacting flows thus far. An overview of the experimental method (equipment, alignment procedure, general optical geometry etc.) is detailed in Chapter 3.

Chapter 4 gives an account of the implementation of the LITGS technique for quantitative measurements of temperature in continuously flowing vapor flows of acetone and toluene. An experimental study of the various parameters that affect the local temperature rise (within the probe volume) associated with acetone- and toluene-LITGS measurements is presented, along with an absorption model for this temperature rise.

Chapter 5 presents a demonstration of LITGS measurements in high pressure, high temperature combustion environments where OH in the burned gas is the target absorbing species. Details of the implementation procedure for 283 nm excitation are presented, along with a description of the pressurized combustion facility used to produce oxygen enriched $CH_4/O_2/N_2$ flames at 5 bar. Results and analysis showing the effectiveness of OH-LITGS measurements under a range of high temperature conditions are presented, along with a discussion on the primary parameters that influence the quality of the LITGS signal at high temperature. The results also prompt a discussion

on the potential for the implementation of OH-LITGS under extremely high pressures and temperatures, such as those found in H_2/O_2 rocket motor combustion.

LITGS measurements where nitric oxide (NO) is targeted as the absorbing species are presented in Chapter 6. Non-reacting measurements are demonstrated in two environments (a static pressure cell and a continuously flowing heated jet) to assess the influence of pressure and temperature on the NO-LITGS signal. Finally, NO-LITGS thermometry is performed through the burned gas region of a stagnation-plate stabilized high pressure, premixed CH_4/NH_3/air flame operating under lean conditions.

Chapter 2

Background

2.1 Overview

This chapter covers the motivation for optical diagnostics and reviews a number of optical techniques used in measuring temperature. The essential theory that governs non-linear optical techniques is presented, specifically detailing the operating principles behind laser induced thermal grating spectroscopy for thermometry (LITGS). Finally, a discussion is provided of the conditions under which the LITGS technique has been applied as a diagnostic tool, specifically for temperature measurements.

2.2 Flame thermometry

In combustion, the flame temperature is considered to be a key controlling scalar due to its influence on reaction rates and pollutant formation (e.g. thermal NO_x formation, unburnt hydrocarbons etc.) [83]. Non-intrusive, spatially and temporally resolved mea-

surements of temperature are essential requirements for improving our understanding of combustion phenomena and validating advanced computational models. The need for accurate and precise data has prompted an extensive research effort in developing methods for quantitative measurements of flame temperatures using a number of experimental tools, including thermocouples [118, 64, 152], Rayleigh scattering [76, 37], two-line LIF [153, 79, 40, 54], Coherent Anti-Stokes Raman Spectroscopy (CARS) [23, 38, 39, 65], Laser Induced Breakdown Spectroscopy (LIBS) [69] and Laser Induced Thermal Grating Spectroscopy (LITGS) [148, 82].

Prior to the development of more sophisticated optical methods, the most common approaches to gas-phase thermometry in both reacting and non-reacting flows have used thermocouple probes. These devices still remain useful for a number of applications where time resolution and durability are not significant [28].

Thermocouple probes provide a simple and affordable option for measuring temperature but have significant limitations. Thermocouples are intrusive probes as the metallic beads perturb the flow field, subsequently influencing the region that is being measured. Secondly, thermocouples have a relatively slow response time (ranging from a few milliseconds to a few seconds, depending on the wire size). This places a limit on the temporal resolution, which is particularly problematic for transient problems (i.e. unsteady flows). Furthermore, in some applications (e.g. highly sooting flames), the accuracy of thermocouple measurements can suffer due to radiative effects. Finally, whereas thin thermocouples can overcome time resolution problems to an extent, these are not durable at high temperatures.

Optical methods for temperature measurement offer improved spatial and temporal resolution. The simplest examples include chemiluminescence and two-color pyrometry [61, 81]. Optical emissions methods rely on capturing natural flame emissions and

therefore require significant optical access. They are also limited in that they are line-of-sight based measurements in nature. Therefore, inhomogeneous effects through the flame are spatially averaged, again limiting spatial resolution.

2.2.1 Laser based approaches to thermometry

A number of laser-based measurement methods have been explored with a view to overcoming some of the limitations associated with optical emissions based techniques. Laser diagnostics tools exploit the molecular processes that result from interaction between incident laser light and the molecules present in the probing region. Some popular laser-based methods that have been used to measure temperature in combustion environments are presented in the next section. Such methods are split between two classes: *linear* and *non-linear* optical diagnostics.

2.2.2 Linear optical diagnostics

The distinction between linear and non-linear spectroscopy is defined by the difference in how the targeted medium (e.g. OH molecules in a flame) responds to incident laser radiation [116].

In linear optical spectroscopy, where the magnitude of the applied electric field is relatively weak, the *polarization vector,* $\boldsymbol{P}$ (the dipole moment per unit volume) and the applied electric field, $\mathbf{E}$ are related by:

$$\mathbf{P}(\omega) = \chi(\omega)\varepsilon_0\mathbf{E}(\omega) \tag{2.1}$$

The constants, $\chi(\omega)$ and ε_0 represent the susceptibility and the permittivity of free space, respectively.

A number of popular laser-based techniques used in measuring temperature fall under the category of *linear* optical diagnostics and are reviewed in the rest of this section.

Rayleigh scattering

Rayleigh scattering measurements are based on the elastic scattering (i.e. no net energy transfer) of incident laser light off a molecule, such that the signal is dependent on both the number density of the molecules within the probe volume and a quantity that describes the likelihood of scattering (unique for each species) known as the Rayleigh cross-section. The likelihood of scattering is inversely proportional to the fourth power of the incident wavelength, so the signal is generally higher in the UV region.

For a mixture with a fixed cross-section, the measurement reflects the local density, which may be translated into a temperature measurement via the ideal gas law.

$$I_R = C I_0 N \sum_{i=1}^{j} X_i \sigma_i \tag{2.2}$$

I_R is the intensity of the scattered signal, I_0 is the incident laser intensity, N is the number density of the probed mixture, X_i is the mole fraction of each constituent species and σ_i is the Rayleigh cross section for each species, i. C is a correction factor, based on the efficiency of the optics used.

Rayleigh scattering suffers from a number of limitations. Any elastic scattering from larger particles causes significant interference in the Rayleigh signal [156]. The technique is therefore limited to extremely clean environments, *i.e.* in the case of combustion,

burners with very little soot production or dust particles [157]. Further, as shown in Eq. 2.2, to determine the number density (and thus, the temperature) from Rayleigh measurements, knowledge of the composition of the species is required. Finally, the signal is scattered in all directions, so that only a small solid angle of the total energy is collected. This is contrast to methods which yield a coherent signal (discussed further in section 2.2.3), which can be collected with much higher efficiency in a particular direction.

Raman scattering

Raman scattering is another popular and relatively simple linear optical diagnostic technique. Unlike Rayleigh, Raman scattering involves a transfer of energy between the incident photon and interacting molecule, resulting in a change in wavelength of the scattered light. Scattering processes that involve energy transfer and a subsequent shift in the wavelength of the incident light are said to be *inelastic*.

Raman scattering is classified into two categories depending on the nature of the energy exchange between the incident photon and the probed molecule. When energy is transferred from the photon to the molecule, the emitted photon exists at a longer wavelength and the scattering is said to be *Stokes shifted* [29]. If the reverse is true, where energy is transferred from the molecule to the scattered photon, then the wavelength of the scattered photon is shorter than the incident wavelength, and the scattering is termed *anti-Stokes shifted*. The process is represented in the energy-level diagram in Fig. 2.1.

Raman signals are orders of magnitude weaker than elastically scattered signals, so high power laser beams are required for single shot gas measurements. The resulting

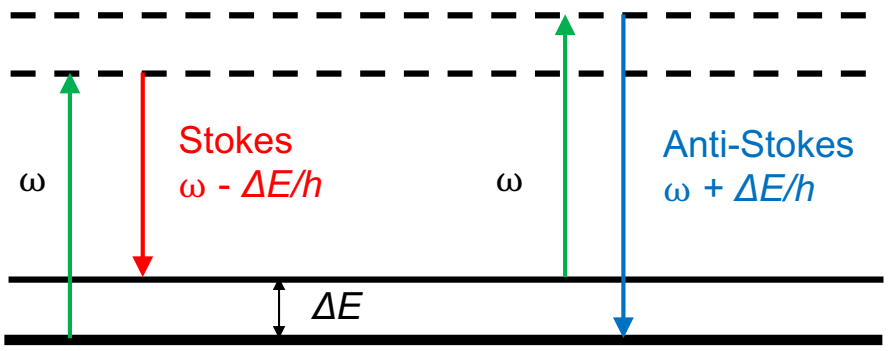

Fig. 2.1 Energy-level representation of Stokes and anti-Stokes shifted raman. Solid lines represent real energy levels, dashed lines represent virtual energy levels.

signal is measured using a spectrometer and is composed of peaks that correspond to the wavelength of the shifted Stokes or anti-Stokes emitted photons. The relative strengths of the spectral lines can then be used to derive the molecule temperature according to the ratio of the Boltzmann distributions for each state [114].

Absorption spectroscopy

Absorption spectroscopy is a well established absorption-based flame thermometry technique. The technique is underpinned by the Beer-Lambert law, which gives the transmitted intensity of monochromatic radiation, I_T, that passes through an absorbing medium by the following relation:

$$\frac{I_T}{I_0} = \exp^{\sigma(T,P,\ldots)n_v\ L} \tag{2.3}$$

$$\tag{2.4}$$

where I_0 is the incident pump power intensity, n_v is the number density of the absorbing vapour molecules, ΔL is the path length associated with the probe volume, and σ is

the absorption cross section. The product of the absorption cross section and the gas density is referred to as the absorption coefficient, α. The molecule-specific 'absorption coefficient' is a function of temperature, pressure and gas composition. The technique therefore determines the properties of a sample by measuring the the transmitted intensity of one or multiple probe beams through an absorbing medium.

Similarly to Raman, the relative strengths of the spectral lines can then be used to derive the molecule temperature according to the ratio of the Boltzmann distributions for each state. The technique exploits the relationship between Boltzmann distributions for thermometry by measuring the relative transmitted intensity, I_T, (and hence, the relative absorption strength) of two or more absorption transitions. Where temporal resolution is not required, the simplest variant of spectroscopy for temperature measurements simply uses a tunable diode laser - referred to as a Tunable Diode-Laser Absorption Spectroscopy (TDLAS).

Absorption spectroscopy measurements are 'line-of-sight' by nature, and are thus limited to integrated measurements along the optical path of the probing beams through the medium of interest. As such, the technique lacks spatial resolution along the propagation direction. This places an important limitation on the applicability of this diagnostic approach, particularly in practical combustors where varying densities and absorber concentration conditions typically exist. Furthermore the presence of particulate matter such as soot, which acts as a black-body absorber, may adversely affect the measurement of transmitted light.

Two-line LIF

Laser Induced Fluorescence (LIF) is a species-selective technique, widely used in combustion diagnostics for both qualitative and quantitative measurements. For a comprehensive review of flame thermometry applications using LIF, the reader is referred to [20]. In LIF measurements, fluorescence is generated using resonant laser excitation to target specific molecules within the measurement region (e.g. OH molecules in a flame using 283 nm excitation). When target molecules absorb the incident laser light, they transition to and populate higher energy levels. The initial, lower state is usually the ground electronic level. Once in the excited state, molecules can relax to the ground state by emitting a photon at a different wavelength, which is collected as LIF signal.

Two-line LIF is an extension of LIF that has been used in flame thermometry [9, 132]. Here, molecules are excited sequentially by two lasers at different wavelengths to a common upper energy level (as shown in Fig. 2.2) to produce fluorescent signal at two intensities ($I_{F,1}$ and $I_{F,2}$) down to two different energy levels [131].

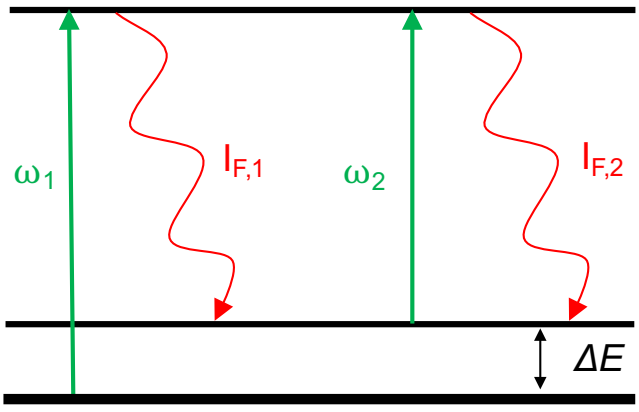

Fig. 2.2 Energy-level representation of molecular excitation and fluorescence process with two-line LIF

Once obtained, the ratio of $I_{F,1}$ and $I_{F,2}$ is used to derive the temperature, based on the Boltzmann equation. If the excitation schemes to produce both $I_{F,1}$ and $I_{F,2}$ share a common upper level, the quench rates are identical and therefore not required to derive the temperature. Like all linear optical techniques, the the signal is scattered in all directions (i.e. it is incoherent in nature), which results in low signal-noise levels, relative to non-linear techniques (discussed in section 2.2.3). Most notably, LIF-based measurement techniques suffer from collisional quenching effects - that is, the fluorescent signal is quenched due to collisional de-activation. As a result, the signal suffers with an increase in pressure. It also suffers when the gas composition contains high quantities of strongly quenching molecules, such as O_2, which limits the techniques capability to obtain signal is lean flames.

2.2.3 Non-linear optical diagnostics

When the magnitude of the electric field ($\mathbf{E}$) is increased, the relationship described by Eq. 2.1 becomes non-linear:

$$\begin{aligned}\mathbf{P}(\omega) = \chi^{(1)}(\omega)\varepsilon_0\mathbf{E}_1(\omega_1) &+ \chi^{(2)}(\omega)\varepsilon_0\mathbf{E}_1(\omega_1)\mathbf{E}_2(\omega_2) \\ &+ \chi^{(3)}(\omega)\varepsilon_0\mathbf{E}_1(\omega_1)\mathbf{E}_2(\omega_2)\mathbf{E}_3(\omega_3)... \end{aligned} \tag{2.5}$$

where $\chi^{(i)}$ is the i^{th} *linear susceptibility*. The difference between the second and third order polarization vector terms is significant. Molecules that have a centre of symmetry directly at their centre (as is the case for all gases [45]) are known as *centrosymmetric*. When the lasing medium consists of centrosymmetric molecules, the second order

susceptibility becomes zero (i.e. the second order process does not exist). In LITGS measurements, which will be described later, only the details of related third order processes are relevant.

Considering the third order terms alone, we have:

$$\mathbf{P}_3(\omega_l) = \chi^{(3)}_{ijkl}(\omega)[\varepsilon_0 \mathbf{E}_i(\omega_i)\mathbf{E}_j(\omega_j)]\mathbf{E}_k(\omega_k) \tag{2.6}$$

A polarization oscillating at a frequency ω_l may be created as a response to the three driving fields at frequencies ω_i, ω_j and ω_k. Field E_k can be thought of as a field that acts on a medium whose refractive index is altered by fields E_i and E_j.

The first two fields create a temporal variation on the optical properties (specifically, the refractive index) at frequencies ω_i and ω_j. Superimposing the frequencies creates a detectable signal, by introducing the third field, E_k (at a known frequency, ω_k) to probe the interacting fields in which the difference between the frequencies is observed. The polarization, P, creates a fourth field (E_l). The frequency of polarization may take on any value associated with the addition/subtraction of the incident frequencies, depending on the configuration.

$$\omega_l = \omega_i \pm \omega_j \pm \omega_k \tag{2.7}$$

This interaction phenomenon whereby two photons are converted into two new photons (when incident on a non-linearly responding medium) is known as *four wave mixing*. The rest of this section examines some of the more common four-wave mixing processes used in combustion diagnostics before reviewing LITGS in more detail.

Degenerate Four wave mixing (DFWM)

Degenerate four wave mixing (DFWM) is a relatively well-established resonant four-wave mixing technique first proposed for combustion diagnostics in the early 1980s to detect the presence of OH in a laminar, premixed methane-air flame [32]. It has since been used to target other minor species found in combustion, including NO [125, 35] and C_2 [62].

In DFWM, all incident beams are degenerate (i.e. equal wavelength), making it easier to meet the phase-matching condition required to produce four-wave mixing signal. When the wavelength is tuned to match a wavelength of molecular resonance for an absorbing medium in the measurement location (e.g. NO at $\approx$ 226 nm), a fourth (signal) beam is produced at the same wavelength. A DFWM spectrum is produced by scanning a tunable laser (often operating in the UV or IR, where molecular resonances usually exist). The spectrum, composed of distinct peaks that correspond to molecular resonance, may be used to make inferences regarding the temperature of the gas being probed by comparing peak intensities in relation to the ratio of the Boltzmann distribution, as is the case in Raman spectroscopy [52].

DFWM measurements are typically limited to stable flames, where the conditions at the measurement volume do not vary in the time taken to produce a DFWM spectrum (i.e. scanning and acquisition time are typically of order of minutes)[68] [26]. However, advances in multiplex DFWM [33], where the spectral information required to derive the temperature can be obtained in a single laser pulse, have meant that the technique has been used to demonstrate measurements of temperature in flames with OH [7, 88], C_2 [63, 62], and NO excitation [34].

DFWM measurements are subject to a few disadvantages. Unlike Coherent anti-Stokes Raman spectroscopy (CARS), DFWM measurements require a resonant molecule, limiting pump lasers to the UV and infra-red and lasers must be tunable, or have a large enough spectral bandwidth to capture multiple resonance transitions for temperature measurements. Whilst the signal beam is coherent, making it relatively easy to isolate, the spectral degeneracy of the pump, probe and signal beams can result in some background interference. Finally, the DFWM signal suffers from an increase in pressure where thermal grating effects due to collisional de-activation start to contaminate the DFWM signal [21]. This is a notable disadvantage against the LITGS technique (which is based on the thermal grating effects that arise from the DFWM approach) employed in this work and is discussed further in 2.5.

Coherent anti-Stokes Raman spectroscopy (CARS)

To date, CARS is the most popular of the established four-wave mixing techniques to be applied to combustion diagnostics for the measurement of temperature and minor species detection. CARS has been used in a variety of forms and used extensively as a diagnostic tool. This section will provide a brief introduction to the technique. For a comprehensive review of the use of CARS in combustion diagnostics, the reader is referred to [109].

Unlike DFWM, the probe volume generated in CARS measurements is composed of three overlapping beams operating at two different wavelengths. The frequencies are selected such that the frequency difference between two laser sources corresponds to Raman coherences to induce an oscillating polarization of the molecule. One laser source is termed the pump beam (ω_1), with the other named the Stokes beam (ω_2). When a third beam is introduced and scatters off the prepared states, like DFWM, it

produces a coherent laser-like signal beam, termed the anti-Stokes shifted beam (ω_3). This arrangement is illustrated in the energy diagram in Fig. 2.3.

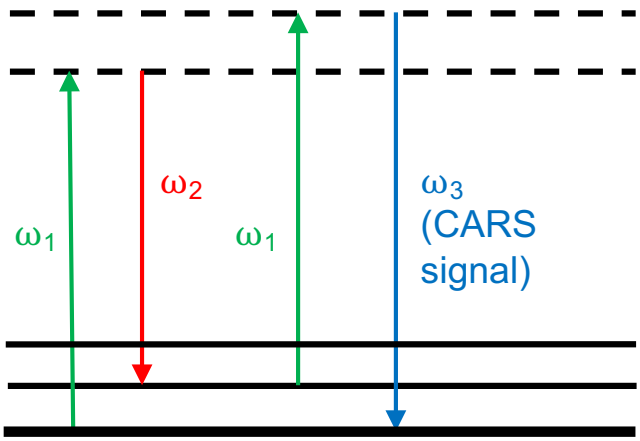

Fig. 2.3 Energy-level representation of the CARS process. Solid lines represent real energy levels, dashed lines represent virtual energy levels.

Once spectrally isolated, the signal beam is collected into a spectrometer. The resulting spectral line widths and intensities are dependent on temperature and species concentration (under some conditions). If, under the conditions of interest, the CARS spectrum can be modelled, the model can be fitted to the spectrum with temperature used as an isolated fitting parameter as a means of extracting it. CARS thermometry has been widely applied as a diagnostic tool in flames with single shot accuracies reported to be around 2 – 6 % [1, 10, 12, 110, 38] and has also been demonstrated in sooting flames [13].

CARS measurements have proven to be popular for a number of reasons. First, like DFWM, the signal is coherent (i.e. beam-like), making it easier to isolate the signal from background interference. Second, signal detection occurs at shorter wavelengths than the pump wavelength, reducing potential interference from LIF. Also, CARS measurements do not require knowledge of the gas composition. Hence, in a flow with unknown species concentrations, CARS can provide highly accurate measurements (so

long as knowledge of a CARS spectrum can be used for fitting). This is in contrast to LITGS where knowledge of the gas composition is essential in yielding accurate results.

However, CARS measurements are particularly challenging to set up given that three pump beams must be tuned to resonance, requiring stable equipment and fine alignment. Furthermore, CARS is usually limited to major species and temperature measurements require difficult and time consuming fitting of the CARS spectrum. Until recently, most CARS measurements used Nd:YAG/dye laser set-ups, producing measurements based on nanosecond laser pulse durations. The development of short-pulse (femtosecond/picoseconds) laser sources have addressed a number of the limitations associated with conventional nanosecond-CARS measurements, including suppression of non-resonant interference , and allowed for more meaningful turbulent flame measurements with kHz repetition rates [105]. The development of more advanced CARS techniques (e.g. hybrid rotational ps/fs-CARS [65]) does, however, add complication and significant cost to the experimental set-up.

Laser induced grating spectroscopy (LIGS)

Laser induced grating spectroscopy (LIGS) has been demonstrated as an effective, non-intrusive gas phase diagnostic tool. The technique has been used in various configurations to measure gas dynamic properties (e.g. sounds speed and thermal diffusivity) [18], temperature [5] [145], pressure [82], velocity [141] and species concentration [27].

Laser induced gratings can be formed via two mechanisms: electrostriction or absorption. Both processes begin with an optical interference pattern produced by two crossing coherent beams in the medium of interest. In electrostriction, the density of the material changes due to the adiabatic compression by the work done by the laser electric field [53].

In absorption, energy is absorbed from a short laser pulse into molecular excitation of the absorbing species, and redistributed into a local temperature change by collisional deactivation (quenching), leading to a local change in density of much higher magnitude than in electrostriction [68]. The rapid local density change generates a pressure wave, which propagates locally along a plane parallel to the local perturbation.

The overall density gradient generated is the sum of those produced by the sound wave plus the local density change. In the case of electrostriction, the local density change is negligible compared to that produced by the sound waves, whilst in the case of thermal gratings, the change produced is the sum of the counter propagating travelling sound waves plus the stationary grating [53]. This change in gradient is detected by means of a probe laser directed to the grating at a Bragg angle for maximum scattering efficiency. The signal obtained from the interference of the probe laser and the density gradient is in theory proportional to the square of the local density perturbation created, and appears in the form of a time-based signal with a characteristic frequency equal to the value or the sound speed of the local medium in the case of an absorbing medium, for laser induced thermal grating spectroscopy (LITGS), or twice that value in the case of pure electrostriction, as laser induced grating electrostrictive spectroscopy (LIEGS). Electrostriction does not require a resonant excitation wavelength for absorption, but the signal obtained can be least one order of magnitude lower than offered by resonant signals with absorption, thus limiting its use in practice.

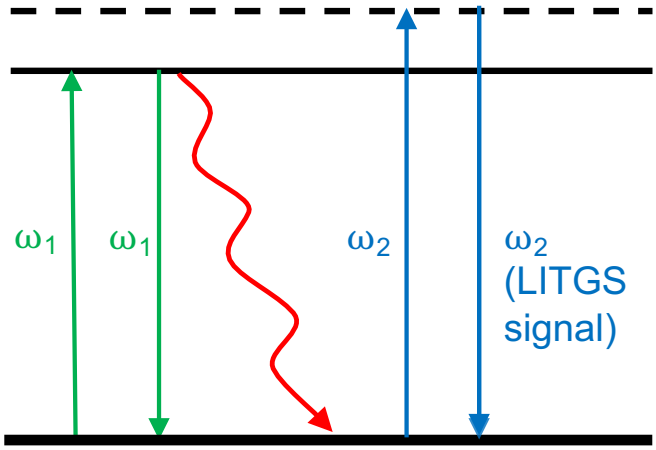

Fig. 2.4 Energy-level representation of LITGS excitation and signal generation process. Solid and dashed lines represent real and virtual energy levels, respectively. Green arrows represent pump excitation, the red, wavy arrow represents quenching transition and blue arrows represent probe and signal beams.

2.3 LITGS - Operating principles

2.3.1 Generating optical gratings

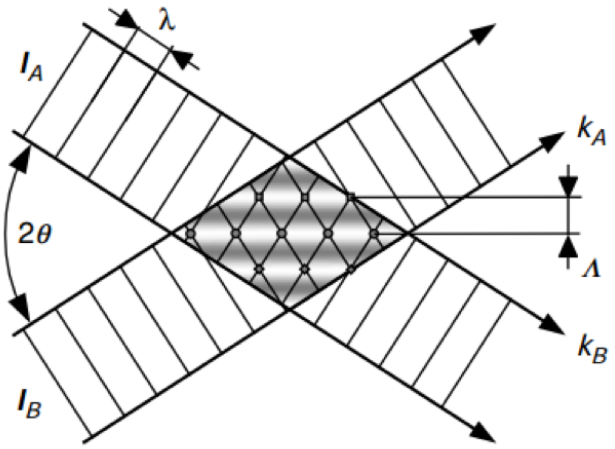

Fig. 2.5 Illustration of grating produced as a result of superposition of two incident laser beams [30]

One of the most important considerations associated with four-wave mixing techniques is the fact that they are *phase sensitive*. A *phase matching* condition must be satisfied in order to achieve efficient mixing. Phase matching is achieved when the wave vectors (descriptors of the nature of the wave, i.e. magnitude and direction) satisfy the condition:

$$\vec{k_l} = \vec{k_i} \pm \vec{k_j} \pm \vec{k_k} \tag{2.8}$$

which represents the conservation of momentum of the incident photons.

Therefore, a geometrical arrangement with the phase must be considered to produce phase matching. In the case of LITGS, the geometrical arrangement consists of two

pulsed laser beams that are focused in a co-propagating manner with the intersection of a probe beam at some angle, θ. The result is a grating based on a variation in intensity over a period in space. This grating generates a number of 'fringes', shown in the Fig. 2.5.

The fringe spacing is given by Eq 2.9.

$$\Lambda = \frac{\lambda_1}{2\sin(\frac{\theta_1}{2})} \tag{2.9}$$

where λ_1 is the pump beam wavelength and θ_1 is the crossing angle, given by:

$$\theta_1 = 2\tan^{-1}\left(\frac{\lambda_1}{2f_l}\right) \tag{2.10}$$

where f_l is the crossing lens focal length.

In the LITGS technique light from the driving pulsed laser must be absorbed by the local medium where species are targeted via molecular excitation. The excited state molecules then re-distribute the absorbed energy into the bulk gas via collisional quenching, which creates a time and space modulation in density within the medium (local change in density). The spatial modulation in density produced by the absorption and redistribution process produces a local stationary thermal grating. The pulsed energy addition creates a thermoacoustic pulse propagating at the local speed of sound.

The intersection of the two pulses produces a local density change propagating at the speed of sound, which can be probed by optical means.

2.3.2 LITGS signal analysis for temperature

The LITGS signal is produced by introducing a continuous probe beam which is scattered off the thermal grating at the Bragg angle (for maximum scattering efficiency), given by:

$$\theta_{Br} = \sin^{-1}\left(\frac{\lambda_2}{2\Lambda}\right) \tag{2.11}$$

Where λ_2 is the probe wavelength and Λ is the grating spacing. If the probe beam intensity is essentially constant through the grating lifetime, the temporal variation of the scattered beam gives the temporal variation of the grating. This scattered signal is collected by a detector for interpretation.

Figure 2.6 shows a typical single-shot LITGS signal trace.

The modulation of the signal in the case of LITGS has been shown to appear at a frequency determined as [68]:

$$f = \frac{c_s}{\Lambda} = 2\frac{c_s}{\lambda_1}\sin\left(\frac{\theta}{2}\right) \tag{2.12}$$

where c_s is the local speed of sound.

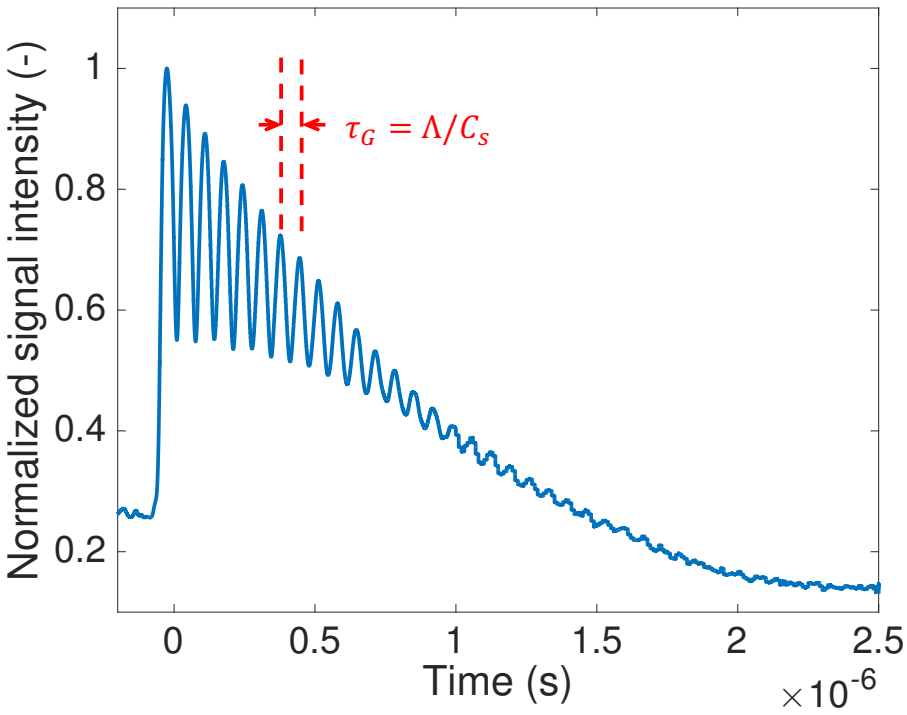

Fig. 2.6 Typical LITGS signal

The local temperature can be determined from the measured speed of sound via the frequency:

$$T = \frac{W}{\gamma \mathcal{R}} c_s^2 = \frac{W}{\gamma \mathcal{R}} \left(\frac{\lambda_1 f}{2 \sin\left(\frac{\theta}{2}\right)} \right)^2 \tag{2.13}$$

where W is the mean molar mass, γ the ratio of specific heats, and $\mathcal{R}$ the universal gas constant.

2.4 LITGS as a diagnostic tool

LITGS was first identified as an interference in degenerate four-wave mixing measurements, and its contribution to the diffraction signal was quantified for the case of resonant and non-resonant excitation in air-water mixtures [42]. The potential for

using the temporal evolution of the signal produced via laser induced thermal gratings for gas-phase thermometry was first recognized using NO_2 as the absorbing species at atmospheric conditions [17]. Initial studies focussed on exploring the behaviour of the diffracted signal in time using a continuous-wave (cw) probe and the signal response to changes in gas dynamic parameters [68]. The first application of LITGS thermometry using a cw probe laser was demonstrated by Latzel *et al.* [82], using OH excitation at 308 nm with a 488 cw probe laser in a high pressure flame. Later, Stevens *et al.* [124] performed temperature measurements in gas mixtures of NO_2 and NO in a static pressure cell (up to 40 bar) using a long pulsed probe laser, significantly boosting the probe power with 2 μs pulses of 200 mJ per pulse. Their results produced temperature measurements with a precision of up to 0.1%. Hemmerling et al. [51] later applied the LITGS technique to excitation of H_2O molecules through rovibrational bands at 820 nm. Measurements were performed in a cell containing humid air and in the vicinity of a premixed atmospheric air flame.

More recently, Williams *et al.* [147] used characteristics of the temporal evolution of the LITGS signal to make inferences regarding the photo-physics of acetone and toluene, which are used as absorbers. More specifically, they obtained signal in a static pressure cell containing varying mixtures of O_2 and N_2 for a fixed absorber concentration to investigate the effect of the concentration of the primary quencher (O_2) on the signal contrast, defined as the modulation depth of the signal (i.e. relative peak-trough intensity). Measurements were performed at pressures ranging from 1 - 8 bar and showed that the signal contrast increases with total pressure in the case of acetone, but decreases in the case of toluene. This is attributed to the differing photo-physics and relaxation dynamics associated with the two molecules. Williams *et al.* [145] then employed LITGS with toluene absorption for temperature measurements under evaporative cooling conditions in an optically accessible GDI engine.

2.5 Technique Selection

Whilst non-linear techniques typically require rather complex alignment of at least three beams, as well as additional experimental components, the coherent nature of the signal beam is distinctly advantageous over scattered signal produced in Rayleigh, Raman and LIF measurements in that it is typically stronger and can be transferred over long distances away from the probe region, making it relatively easy to isolate the signal from interference.

Whilst TC-LIF has been employed for temperature measurements in high pressure combustion, the fluorescent signal suffers in high density mixtures due to the increased number of collisions which de-activate the excited state molecules, limiting the achievable SNR and accuracy. The ability to effectively measure the spatial and temporal distribution of burned gas temperatures in flames is important, particularly in the context of NO_x emissions which are most prevalent at high temperatures [75]. Over the last three decades, CARS has been established as a popular laser diagnostic technique for accurate, non-intrusive measurements of temperature due to its strong, coherent signal output and robustness in harsh combustion environments [56, 139]. Typical nano-second CARS measurements rely on acquiring well defined spectral information to derive the temperature and can suffer from line broadening at high pressure. Obtaining spectral information also requires tunable lasers and a spectrometer to image the CARS spectrum, adding some cost and a little more complexity to the experimental configuration.

LITGS offers the potential to provide precise temperature data using a simpler experimental configuration and data processing techniques. LITGS signals are expected to strengthen with pressure given that the strength of the thermal grating relies on

collisional de-activation (i.e. quenching) of the excited state molecules. Unlike CARS measurements, LITGS thermometry is based on a frequency measurement rather than an intensity ratio measurement. Since time measurements are routinely more accurate than intensity measurements, LITGS can potentially offer greater precision. Note that one of the primary limitations associated with LITGS measurements is that, unlike, say, N_2-CARS, they require knowledge of the gas composition to yield accurate measurements.

The advantages and disadvantages associated with LITGS and each of the relatively well-established techniques are summarized in table 2.1.

Technique	Advantages	Disadvantages
Rayleigh	Requires only one laser source	Incoherent signal Accuracy limited by knowledge of multi-species cross-sections Requires very clean measurement environment
LIF	Can provide temperature imaging High spatial resolution	Incoherent signal Intensity based Suffers with collisional quenching (and hence pressure)
Raman	Not sensitive to collisional quenching Requires only one laser source	Incoherent signal Relatively weak signal (small cross-sections) Intensity-based (difficult to separate signal from noise)
CARS	Coherent signal (hence improved SNR) Accurate (typically 2 – 3 %)[137] Suitable for harsh combustion environments Signal increases with pressure	Requires multiple laser sources Intensity-based (difficult to separate signal from interference) Sensitive to line broadening at high pressure
LITGS	Coherent signal (hence improved SNR) Simple data processing (relative to CARS) Frequency-based temperature measurements Signal expected to improve with pressure	Requires multiple laser sources Typically point-based Requires absorbing species Requires knowledge of gas composition

Table 2.1 Pros and cons of temperature measurement techniques

2.6 Theoretical model for LITGS Signal

Paul *et al.* [99] proposed a theoretical model for the temporal behaviour of the LITGS signal, based on the evolution of the gas density after a laser pulse which is probed by the continuous laser. The model starts by considering the evolution of the number density of excited molecules N^* [68]:

$$\frac{dN^*}{dt} = E_p B N_{\alpha 0} 2[1 + \cos(2\pi x/\Lambda)] g(t, \tau_L) f(x, d) - (A + Q)N^* + D\frac{\partial^2 N^*}{\partial x^2} \qquad (2.14)$$

where Q is the quenching rate, D is the molecular diffusivity for the excited molecule, E_p is the laser energy flux per pulse, $N_{\alpha 0}$ is the number density of absorbing species at static conditions (*i.e.* without molecular excitation) and A and B represent the Einstein coefficients for absorption and spontaneous emission. These simply represent the probability per unit time that a molecule in a particular energy state will emit or absorb a photon. The functions $f(x, d)$ and $g(t, \tau_L)$ represent the laser spatial and normalised temporal profiles respectively where τ_L is the pulse duration and d is the laser spot size.

The temporal profile which represents the driving energy pulse is assumed to take the form of a rapidly decaying exponential:

$$g(t) = \frac{2t}{\tau_L^2} \exp\left[-\left(\frac{t}{\tau_L}\right)^2\right] \qquad (2.15)$$

and $f(x, d)$ is also assumed to be to be Gaussian.

The following linearized hydrodynamic equations (2.16 - 2.18) form the governing equations for an assessment of the evolution of the pressure and density perturbations in the probed region, as formulated by Paul *et al.* [99]. They are non-dimensionalised in space and time via a characteristic length (fringe spacing, Λ) and time (the acoustic wave transit time, $\tau = \frac{\Lambda}{c_0}$). The non-dimensional quantities are defined by $\zeta(t) = \frac{c_0 t}{\Lambda}$ and $\xi(x) = \frac{x}{\Lambda}$.

The density, ρ, pressure, P, and velocity, u are linearised according to static and fluctuating components by $\rho = \rho_0 + \Delta\rho$, $P = P_0 + \Delta P$ and $u = \Delta u$ (given that at static conditions, $u_0 = 0$).

The linearised, normalised continuity equation becomes:

$$\boxed{\frac{\partial \rho'}{\partial \zeta} + \frac{\partial u'}{\partial \xi} = 0} \tag{2.16}$$

Applying the same rationale to the momentum and energy equations with normalised variables u' and P' we have:

$$\boxed{\frac{\partial u'}{\partial \zeta} + \frac{1}{\gamma}\frac{\partial P'}{\partial \xi} - \frac{4}{3Re}\frac{\partial^2 u'}{\partial \xi^2} = 0} \tag{2.17}$$

$$\boxed{\frac{1}{\gamma}\frac{\partial P'}{\partial \zeta} - \frac{\partial \rho'}{\partial \zeta} - \frac{1}{Re.Pr}\left(\frac{\partial^2 P'}{\partial \xi^2} - \frac{\partial^2 \rho'}{\partial \xi^2}\right) = \frac{\gamma - 1}{\gamma}\frac{\epsilon h v_\alpha Q \Lambda}{c_0}\frac{N^*(\zeta\xi)}{P_0}} \tag{2.18}$$

Where h is Planck's constant, γ is the ratio of specific heats, v_α is the frequency of the associated electromagnetic wave, Re is the Reynold's number and Pr is the Prandtl number.

Equation 2.17, which represents momentum transport through the medium, is set to zero as it is assumed that no net force is acting on the molecules in cases where the laser induced electric field is too weak to result in electrostriction. Eq. 2.18

Assuming that the problem is irrotational (i.e. $\nabla \times u = 0$) and the set of equations are separable in space and time, they can be combined to yield a single wave equation.

$$\rho'_{\xi\xi\xi} - \left[\frac{4}{3Re} + \frac{\gamma}{Re.Pr}\right]\rho'_{\xi\xi\zeta\zeta} - \rho'_{\xi\xi\zeta} + \frac{4\gamma}{3Re^2Pr}\rho'_{\zeta\xi\xi\xi\xi} + \frac{\gamma}{RePr}\rho'_{\xi\xi\xi\xi} = \frac{\gamma-1}{\gamma}\frac{\epsilon h v_a Q \tau N^*_{\xi\xi}}{P_0} \tag{2.19}$$

The solution to this equation is obtained via Fourier and Laplace transforms in space and time, respectively, leading to a single equation representing the density perturbation:

$$\rho' = -(2\pi^2)\frac{\gamma-1}{\gamma}\frac{\alpha}{P_0}\frac{8E_p}{\pi d^2}\cos(2\pi\xi)Z(\zeta) \tag{2.20}$$

which gives a cosinusoidal modulation in density in space and a separated temporal function, $Z(\zeta)$, which is proportional to the convolution of the temporal response of the gas density to an instantaneous input of thermal energy, $W(\zeta)$, the temporal profile of the laser pulse, $G(\zeta)$ and the temporal profile of the quenching process, $\mathrm{M}(\zeta)$.

The medium response, $W(\zeta)$, which corresponds to the linear superposition of stationary temperature wave decaying due to thermal diffusion, and of two counter-propagating acoustic waves decaying by viscous dissipation is defined with a constant phase shift, ϕ as:

$$W(\zeta) = a_1\exp(s_1\zeta) - 2a_2\exp(-b_1\zeta)\cos(b_2\zeta + \phi) \tag{2.21}$$

where the constants s_1, b_1 and b_2 are determined as part of the solution.

$$s_1 = -\frac{(2\pi)^2}{RePr} \tag{2.22}$$

$$b_1 = (\gamma - 1 + \frac{4Pr}{3})\frac{(2\pi)^2}{RePr} \tag{2.23}$$

$$b_2 = 2\pi \tag{2.24}$$

The medium response represented by Eq. 2.21 provides the mathematical justification for the qualitative description of the operating principles associated with LITGS. The equation is composed of two components. The first term represents the stationary thermal grating, which decays exponentially due to heat conduction to the surroundings with a time constant of $-s_1\zeta$. The second represents the contribution of the standing acoustic wave, which decays according to the time constant $b_2\zeta$.

2.7 Summary

The overview of laser-based approaches to thermometry in flames presented in this chapter provides the rationale behind the development of LITGS as a tool for temperature measurements in high pressure combustion systems. The theory laid out in this chapter, and specifically equation 2.21, allows us to understand the shape of the LITGS signal for a given optical geometry (i.e. the grating spacing, λ) and set of thermodynamic conditions. The overview of theoretical concepts and background literature presented here is intended to aid the interpretation of results shown in Chapter 4, where factors that affect the local temperature rise required to produce LITGS signal are investigated, and Chapters 5 and 6, where LITGS is demonstrated

in high pressure combustion scenarios. The next chapter details the experimental methods and equipment used to obtain LITGS data presented in the later chapters of this thesis.

Chapter 3

Experimental Methods

This chapter presents details of the experimental approach to the LITGS measurements reported in this thesis. A general overview of the optical geometry and essential experimental requirements for LITGS measurements (including a typical optical geometry and signal acquisition equipment) are given, along with details of the alignment procedure and data processing approach employed in this work. The specific optical parameters and essential features of the equipment used in each experiment are presented in greater depth in each of the following three chapters.

3.1 Lasers, optical geometry and acquisition

Figure 3.1 shows the general optical layout and equipment necessary to generate and acquire LITGS signals.

The optical set-up requires three laser sources. The pulsed pump beam is used to generate the thermal grating and the probe beam is scattered off the grating to produce

the LITGS signal beam. A tracking beam is used to track the path of the scattered signal during alignment so that the signal can be directed towards the PMT for collection and acquisition. Molecular excitation of the target absorbing species (e.g. acetone, toluene, OH or NO, depending on the application of interest) and resultant collisional quenching leads to a thermal grating induced via the two crossing pump laser beams.

The crossing geometry is generated by first directing the pump beam through a 50/50 beam splitter in order to create two parallel pulsed beams of equal intensity. A compensation plate (denoted CP in the diagram) is placed in front of the beam that has travelled the shorter path in order compensate for the longer path of the other. The beams are focused in the rear focal plane of the crossing lens. As the beams cross an interference pattern is created which defines the location of the grating. The pump beams and probe are then captured by a beam dump. The pump laser beam is monitored by collecting light scattered off the first mirror into a photo-diode in order to assess its quality (i.e. pulse shape, intensity, timing).

The cw probe beam is delivered by a diode-pumped solid state laser in parallel to the pump beams. The beam is deflected by the crossing lens at a pre-calculated Bragg angle to the grating plane. The largest fraction of the probe beam proceeds undeflected, whilst the coherently scattered Bragg-deflected fraction becomes the signal beam acquired by the photomultiplier. This characteristic allows unwanted secondary surface reflections to be blocked, allowing for stronger signal characteristics against any interference.

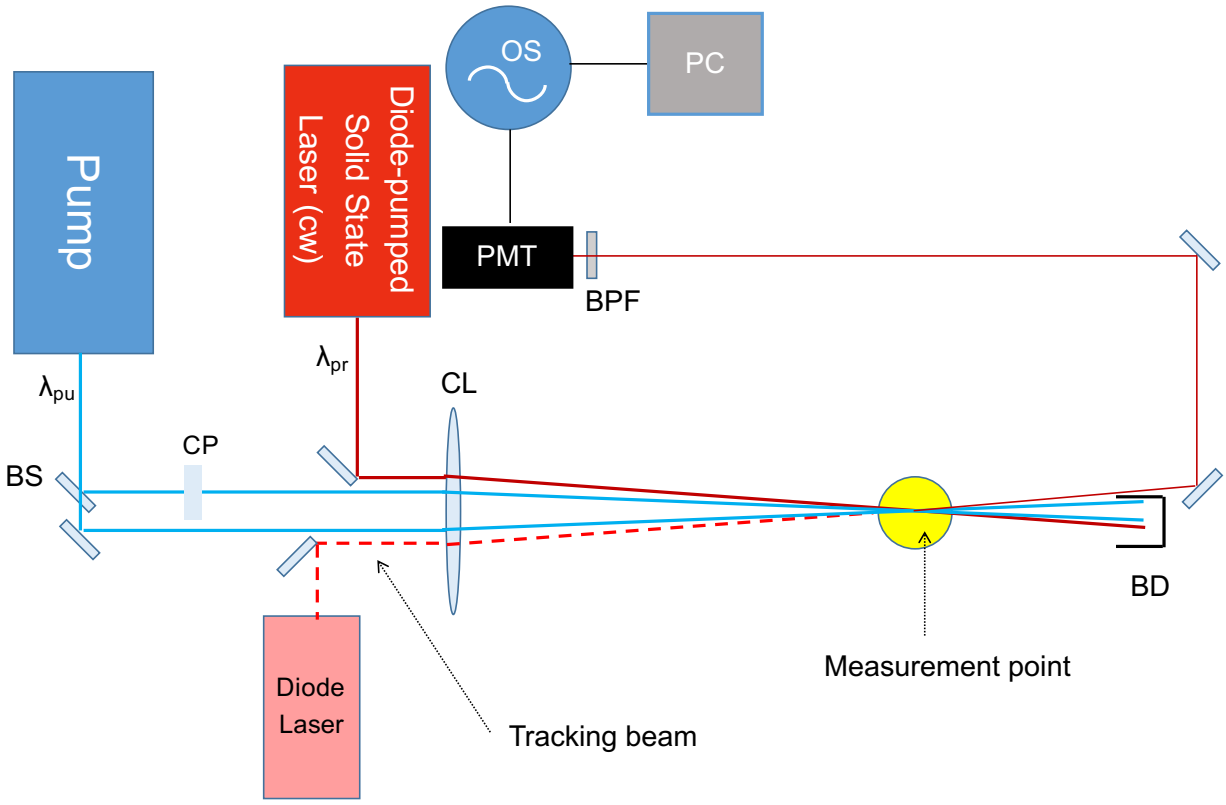

Fig. 3.1 General optical layout for LITGS experiments. BS: beam splitter, BD: beam dump, CP: compensator plate, OS: oscilloscope, PMT, BPF: band-pass filter: photomultiplier tube.

Details of the specific equipment used for each experiment presented in this thesis (including lasers, PMTs etc.) are provided in section 3.4. For most experiments reported in this thesis, pump pulses are generated using flashlamp pumped Nd:YAG lasers to pump a dye laser. The dye solution used is dependent on the required wavelength for the excitation of the target species. For example, for 226.9 nm excitation of nitric oxide (see Chapter 6), the dye solution used was Coumarin 47 in ethanol. Typical pump pulse energies range from around 100 to 200 mJ, depending on the selected harmonic of the fundamental laser wavelength advised in the scheme for the desired dye laser output (*e.g.* 532 nm, 355 nm etc.). Pulse durations are typically around 8 ns, and the spectral bandwidths are of order 1 cm^{-1}.

Continuous-wave (cw) lasers are used to probe the thermal grating as the probe duration must be at least as long as the duration of the LITGS signal, typically of the order of hundreds of nanoseconds. Long-pulsed lasers have been employed as probes for LITGS measurements in the past [124] (which provide much stronger probe intensities), however cw lasers, which are typically limited to 1 – 2 W, are preferred for their stable power characteristics and ease of alignment. In all cases, the probe wavelength is selected such that it is non-resonant, so that no further absorption of the target species (or any other species in the gas mixture) takes place.

The diffracted signal beam is collected into a photomultiplier tube (PMT). Whilst it is possible to use fast-response photo-diodes for signal collection, where the signal is particularly strong (e.g. where a long pulsed beam is used to probe high pressure, low temperature mixtures), PMTs are preferred here as the LITGS signal intensities produced using cw probe beams are relatively low. PMTs are also advantageous in that they are composed of sufficiently large active collection areas, such that the whole signal can be collected without employing a focusing lens to direct the signal onto the detection region. This reduces the amount of scattered light entering the detector.

Whilst the wavelength of the probe beam is selected to be different to that of the pump beams in order to spectrally isolate the signal, the PMT is sensitive to both wavelengths. Hence, a high transmission narrow bandpass filter is placed in the path of the signal beam to block scattered light from the pumps.

3.1.1 LITGS alignment

To obtain optimally strong and stable LITGS measurements, careful alignment is required to ensure good overlap between the two pumps and the probe beam. This section provides a brief summary of the alignment procedure. For a more detailed description the reader is referred to [144].

In order to position the laser beams appropriately a pair of masks are designed and placed in the near-field and far-field with respect to the measurement zone. The masks act as alignment guides as to where the pump, probe and tracking beams should be positioned relative to one another to ensure that a grating is produced in the intended measurement location and that the probe beam scatters off the grating at the Bragg angle. Fig. 3.2 is an illustrative example of the alignment masks used in LITGS experiments.

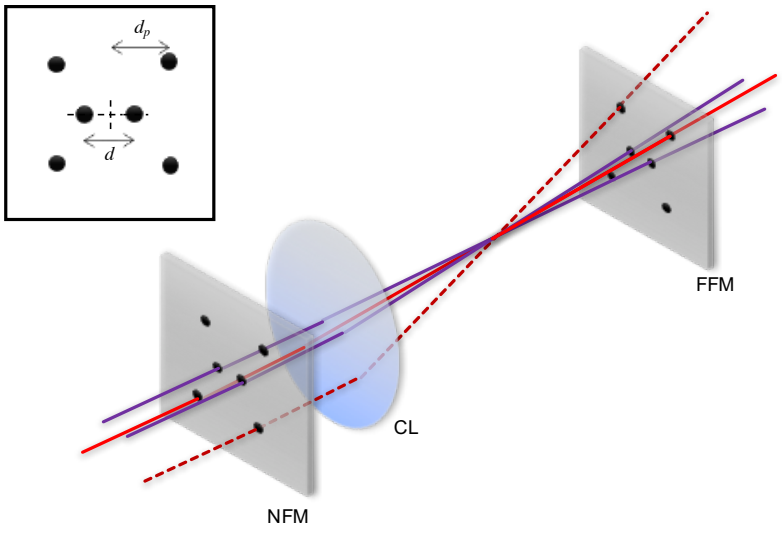

Fig. 3.2 Illustration of alignment masks for beam crossing as detailed in text. Purple, solid red and dashed red lines represent pumps, probe and tracking beams, respectively. NFM: near-field mask, FFM: far-field mask, CL: crossing lens

A simple set of equations, outlined in section 2.3, allows us to calculate basic geometrical properties of the grating. The fringe spacing, pump crossing angle and Bragg angle are given by Eq.'s 2.9, 2.10 and 2.11, respectively. A mask can be produced with the appropriate relative spacing between the output beams in mind. A diode laser was used to track the path of the diffracted signal beam and aid the alignment procedure. In order to accurately determine the *position* of maximum intensity (i.e. where the thermal grating is strongest), the light was collected into a pinhole as part of the fine-tuning of the alignment (*i.e.* laser light sent through pinhole and out onto mask). In all experiments presented in this thesis, where UV pumps are employed (i.e. 226 nm $> \lambda_1 >$ 308 nm), the alignment procedure provides adequate accuracy to produce LITGS signals in environments with relatively small concentrations of acetone vapour in air (i.e. a diluted jet or static pressure cell). Fine adjustments can then be made to the mirrors to optimize 'live' signal observable on an oscilloscope.

Chapters 4, 5 and 6 present data acquired for LITGS set-ups employing various geometric parameters, where the set-up depends on a number of factors including the target absorbing species, the degree of optical access etc. Table 3.1 summarises the main set of geometric and operating parameters for each geometric variation employed in this work, with more specific details presented in each of the following chapters. Acetone- and toluene-LITGS measurements were acquired using two different pump wavelengths (see Chapter 4) and NO-LITGS measurements were acquired under non-reacting and reacting (starred) conditions (see Chapter 6).

Chapter	**4**		**5**	**6**	
Absorber	**Acetone/Toluene**		**OH**	**NO**	
Pump wavelength, λ_1 (nm)	266	308	283*	226.2999	
Pump beam spacing, d (mm)	10		10*	10	15*
Probe wavelength, λ_2 (nm)	617		488*	617	488*
Crossing lens focal length, f (mm)	500		1000*	750	1000*

Table 3.1 Summary of operating parameters for LITGS systems presented in this thesis. Starred values represent parameters used in flame measurements

3.1.2 Grating geometry

Figure 3.3 gives a geometric representation of the interaction region of two crossing pump beams used to form a thermal grating.

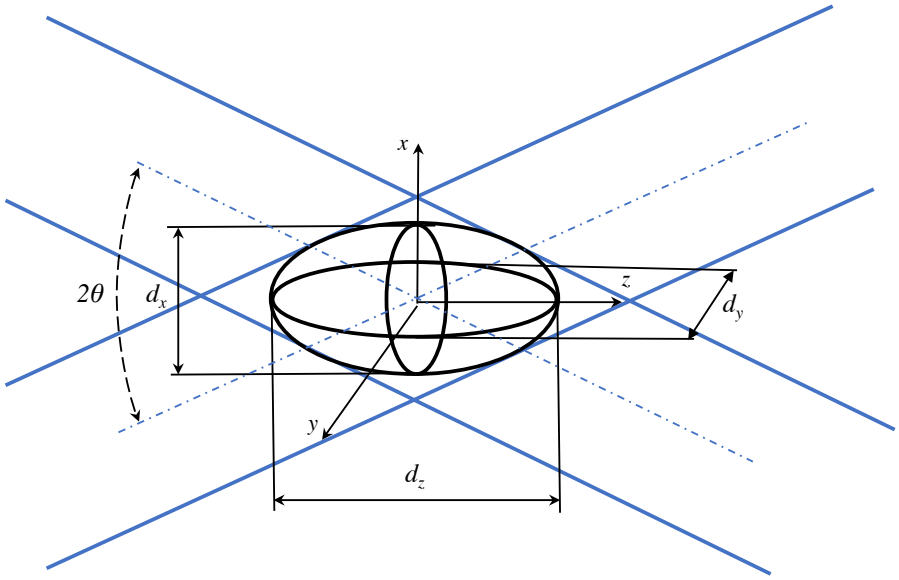

Fig. 3.3 Grating geometry based on [96]

The fringe spacing, Λ (see Eq. 2.9), is a function of the pump wavelength, λ_1, and the crossing angle, θ, which is also a function of the pump separation, d. In cases where optical access is highly restricted (e.g. Chapters 5 and 6, where beams must pass through small quartz windows) the focal length of the crossing lens and pump separation must be selected such that the fringe spacing is large enough to produce expected oscillation frequencies that are well below the bandwidth of the oscilloscope which is 500 MHz for all scopes used in experiments presented in this thesis.

We define the probe volume (based on Fig. 3.3) as:

$$\Delta V = \frac{4\pi}{3} d_x d_y d_z \tag{3.1}$$

The beam diameter at the focal point is:

$$d_f = \frac{4 f \lambda_1}{\pi d} \tag{3.2}$$

where f is the focal length and d is the distance between the two pump beams. d_x and d_y are given by:

$$d_x = \frac{d_f}{\cos\theta} \tag{3.3}$$

$$d_y = d_f \tag{3.4}$$

The length of overlapping region is given by:

$$d_z = \frac{d_f}{\sin\theta} \tag{3.5}$$

In LITGS thermometry, the *mean* temperature within the probe volume is assumed to be uniform (i.e. each single shot represents a single value for temperature). The probe volume length, d_z should be be large enough to obtain signal, but remain sufficiently small to avoid spatial averaging of temperature over inhomogeneous regions and ensure that measurements are accurate.

3.2 Oscillation frequency extraction

The signal delivered by the probe beam is modulated by the passage of the sound wave over the grating, thus containing information about the local speed of sound within the probe volume. Equation 2.13 shows that the derived LITGS temperature is proportional to the square of the oscillation frequency of the signal, f.

The frequency may be extracted from the short LITGS signal burst using a number of methods, with the most popular being direct peak detection in the time domain, or a Fast Fourier Transform (FFT) in the frequency domain. The present work uses direct measurement of the peak and trough location after signal smoothing, similar to the method presented by Stampanoni-Panariello *et al.* [122]. This was evaluated as the simplest and most robust method over a wide range of frequencies in cases where signals are strong. Alternative methods, such as frequency domain analysis using a Fast Fourier Transform (FFT), are effective in cases where signal levels are weak and where uncertainty in determining exact peak locations becomes significant [149]. However, frequency domain methods can lead to inaccurate results under conditions where the signals are noisy (i.e. fluctuations due to noise are close to signal oscillation frequency) and decay rapidly, as is the case in high temperature combustion. This is because accurate measurements in the frequency domain rely on identifying a distinct peak in the power spectrum, which can be broadened by interference or weakened due to too few LITGS oscillations in shorter signals. A detailed review of the various techniques used post-processing LITGS signal for frequency extraction can be found in [149].

The smoothing procedure was carried out based on the well-established moving weighted average polynomial method proposed by Savitzky and Golay [113] to determine the first derivative of the signal trace. The detailed procedure for signal smoothing using

the Savitzky-Golay method can be found in [113]. Figure 3.4 shows a single shot example of smoothed LITGS signal.

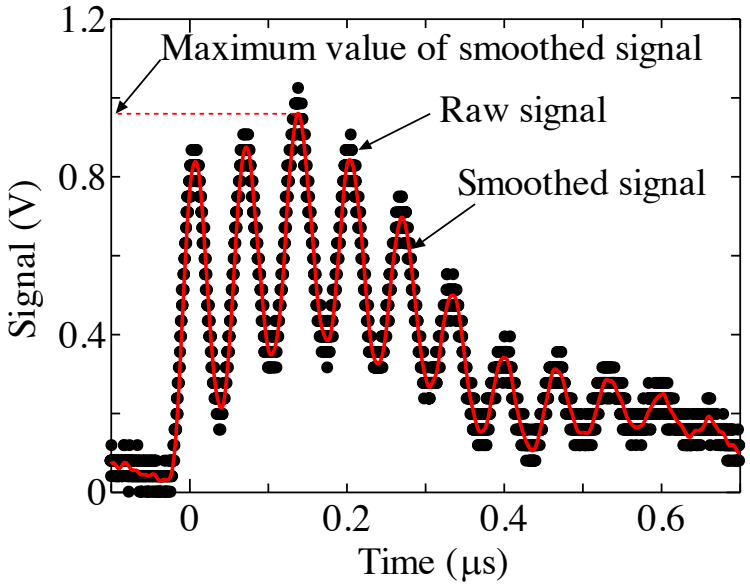

Fig. 3.4 Example of smoothed LITGS signal

Once smoothed, we identify the first derivative of the signal trace (i.e. the rate at which the signal intensity, V, changes in time dV/dt) to obtain the local peaks and troughs (i.e. where $dV/dt = 0$, see Fig. 3.5). This allows us to detect the local frequencies between each set of peaks and troughs within the signal trace. The average frequency is then calculated over the trace to obtain a single-shot average frequency.

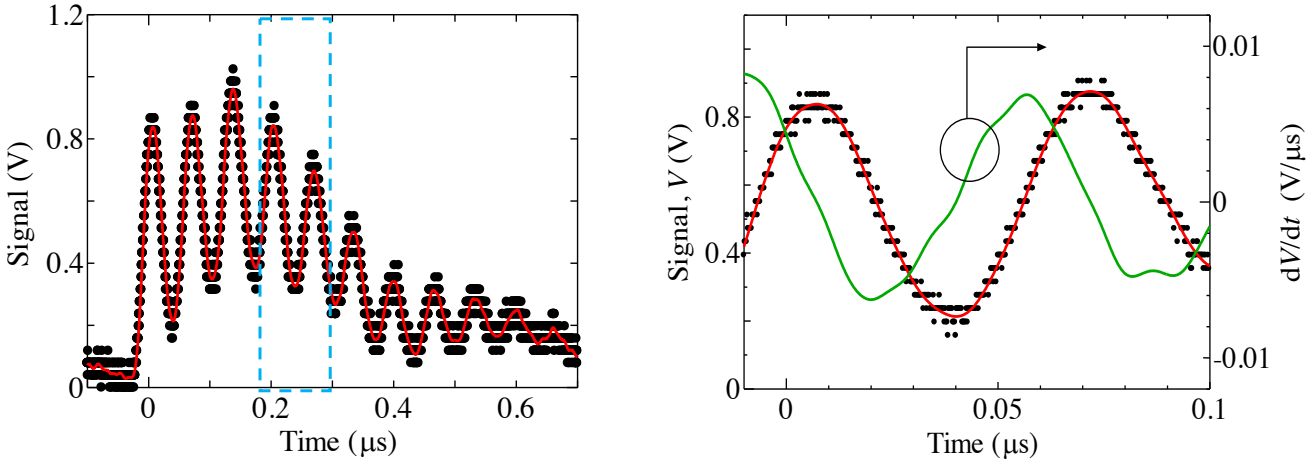

Fig. 3.5 Example of first derivative calculation (green line) over sample region of LITGS signal (encased by blue dashed line)

3.3 Sources of uncertainty in LITGS thermometry

Equation 2.13 shows that the accuracy in temperature depends on the uncertainties in frequency, grating spacing, molecular weight and ratio of specific heats. We consider these uncertainties below.

3.3.1 Grating spacing

The grating spacing, Λ can be obtained from a knowledge of the geometric parameters Eq. 2.9. However, misalignment, beam steering (e.g. through quartz glass or a flame) or the use of a non-achromatic crossing lens, with imperfect estimation of focal length for a given pump wavelength, can lead to significant error in the estimation of this parameter [149]. The alignment optimization procedure involves fine adjustment of mirrors that direct the pump and probe beams using live signal, which can lead to

slight changes in geometrical parameters like the pump spacing, altering the true value of Λ.

In most cases this source of error can be mitigated for using a simple calibration procedure at conditions where the temperature and gas composition are known, for example in a laminar, cold flow containing some absorber where the composition and temperature are known. Given a particular probe geometry, the temperature can be determined relative to the calibrated value, so that the precision can be high, but the accuracy becomes dependent on the accuracy of the original calibration measurement.

3.3.2 Gas composition

In all cases presented in this work, where measurements are performed in stable laminar jets, static pressure cells and in post-flame regions of laminar flames, the ratio of the molecular weight to specific heat ratio, M/γ, is assumed to be fixed during acquisition (for each condition). For flame measurements, the burned gas composition (dominated by H_2O, CO_2 and N_2) is determined using 1D flame simulations using ChemKin. Specific details of the simulations are discussed in further detail in Chapters 5 and 6. Brown *et al.* [14] performed an uncertainty analysis for LITGS measurements in the burned gas of stoichiometric and slightly rich hydrocarbon-air flame mixtures. The results showed that the relative sensitivity of M/γ values to variations in equivalence ratio and major species at a given condition were lower than than 1%.

3.4 Equipment

Table 3.2 shows the lasers and detection equipment used in each LITGS set-up presented in this thesis for the reader's reference. Further details of the individual set-ups are presented in each of the following chapters.

Chapter (Absorber)	**4 (Acetone/Toluene)**		**5 (OH)**	**6 (NO)**
λ_1 **(nm)**	266	308	283	226
Pump laser	Continuum Surelight III (266 nm)	Continuum Surelight II (355 nm)	Spectra-physics GCR-250 (355 nm)	Spectra-physics GCR-250 (355 nm)
Dye laser	N/A	Sirah cobra stretch (CSTR-9-2400)	Sirah PrecisionScan	Sirah PrecisionScan
Probe laser	Low noise solid-state (MLL-FN-671) 671 nm, Max. 1 W	Low noise solid-state (MLL-FN-671) 671 nm, max 1 W	NavoPro PB 445-1000 MM 445 nm max 800 mW	Omicron BrixX 445-2500 448 nm max 2.5 W
PMT	Hamamatsu H10721-20	Hamamatsu H10721-20	Hamamatsu R928	Hamamatsu R928
Oscilloscope	Picoscope 6404D (5 GS/s, 500 MHz bandwith)	Picoscope 6404D (5 GS/s, 500 MHz bandwith)	Tektronix (5 GS/s, 500 MHz bandwith)	Keysight DSOS054 20 GS/s, 500 MHz bandwith)

Table 3.2 Summary of lasers and signal acquisition equipment.

Chapter 4

LITGS measurements of temperature in acetone and toluene vapour flows

4.1 Chapter overview

In this chapter, laser induced thermal grating spectroscopy is employed to obtain quantitative measurements of temperature in continuous flows of both acetone/air and toluene/air mixtures under atmospheric conditions. As discussed in Chapter 2, the absorption and thermalisation process in LITGS measurements leads to a stationary thermal grating, and a subsequent rise in the local temperature within the probe volume. In this work, the local temperature rise due to LITGS has been measured as a function of the incident pump energy and the mole fraction of the absorbing species (i.e. acetone or toluene) in the mixture. Results indicate that LITGS has the potential to produce accurate and precise measurements of temperature under atmospheric

conditions, but that the product of the pump intensity at the probe volume and the absorber concentration must remain relatively low to avoid significant localised heating of the measurement region.

4.1.1 Motivation

The use of LITGS for detection of temperature relies on the requirement that the temperature rise (and density drop) be sufficiently high to allow for signal detection, yet sufficiently low so as not to affect the local temperature being probed.

The purpose of the investigation presented in this chapter is to evaluate the relationship between the local temperature rise in the LITGS probe volume detected by the absorption of energy as a function of the absorbing species mole fraction and laser pump intensity. Two popular species used for their favourable absorption characteristics in the near UV [72, 147] are considered: acetone and toluene.

The estimated energy absorbed is compared to theoretical considerations, and a practical guideline to the trade-off between signal strength and non-intrusivity is drawn.

4.2 Absorption model - quantifying local temperature rise

In order to understand the tradeoff between higher signal and intrusiveness via the energy absorbed by the probe volume, we consider the maximum power per unit time and area of energy that can be absorbed by the probe volume region using the

Beer-Lambert law [50]:

$$dI = -I\sigma n_v \, dx \tag{4.1}$$

$$\Delta I \approx I_0 \sigma n_v \Delta L \tag{4.2}$$

where I_0 is the incident pump power intensity, n_v is the number density of the absorbing vapour molecules, ΔL is the path length associated with the probe volume, and σ is the absorption cross section. The mean pulse intensity is estimated from the mean pulse energy, E_p, the pulse duration, τ_p, and the beam cross sectional area at the focal point, A, as $I_0 = E_p/(\tau_p A)$, so that :

$$\Delta I = \frac{E_p}{\tau A} \sigma n_v \Delta L \tag{4.3}$$

The power absorbed within that time can be converted into thermal energy or re-radiated. Therefore, the maximum temperature rise ΔT_m can be estimated from the energy balance for a rhomboidal probe volume of cross sectional area A and length ΔL over time τ:

$$\Delta E_T = \rho c_p \Delta T_m \, A \Delta L = \eta E_p \sigma n_v \Delta L \tag{4.4}$$

$$\frac{\Delta T}{T_0} = \eta \frac{E_p}{\rho c_p T_0} \frac{\sigma}{A} n_v = \eta \frac{E_p \mathcal{A}}{\bar{c}_p T_0} \frac{\sigma}{A} X_v \tag{4.5}$$

where $\bar{c}_p$ is the molar specific heat of the mixture, $\mathcal{A}$ Avogadro's number, and η is an overall efficiency of conversion of the incoming energy into thermal energy. In the next sections, we consider the measured temperature rise as a function of the pump energy, E_p, and absorber mole fraction, X_v.

4.3 Experimental set-up

4.3.1 Optical layout

The optical layout of the experiment is shown in Fig 4.1. Pump pulses of 8 ns duration at a frequency of 10 Hz from a frequency doubled Nd:YAG laser (Continuum Surelite I-10) pumping a Sirah dye laser at 308 nm delivered energies between 1 – 12 mJ over a diameter of 3.9 mm. The beam diameter was measured at the position of the crossing lens by recording the intensity of the beam using a photo-diode as a knife edge is translated through the beam using a calibrated translation stage. The pump beam was directed into a 50/50 beam splitter, which separated two pulses to generate the grating. A phase delay quartz plate of 12 mm thickness was inserted along the path of one of the beams to compensate for the longer pathlength. The pump beams separated by a distance of 7 mm were focused towards the probe volume using a single 500 mm focal length crossing lens for a crossing angle of 0.802°. Based on Eq. 3.5, the length of the interaction region is 7.2 mm. The cw probe beam (λ_2 = 671 nm, diameter around 1 mm) of power up to 1 W was provided by a diode-pumped solid state laser (CNI, MLL-III-300) at the Bragg angle ($\approx$ 0.88° from Eq. 2.11) to the midplane of the crossed beams.

The diffracted signal was collected at the corresponding Bragg angle via mirrors into a photomultiplier tube (Hamamatsu PMT), with the gain set to 0.55 for a sensitivity of 80 mA/W after spectral filtering with a narrow bandwidth around the probe wavelength. The signal, triggered from the rise in the collected pump signal itself with a threshold of 150 mV was collected using a PC oscilloscope (PicoScope 6000) at a maximum sampling rate of 5 GS/s and 8-bit precision.

Most measurements presented in this chapter were acquired at 308 nm pump excitation, where the absorption coefficients for acetone and toluene are close in magnitude (values are given in section 4.4.4). To supplement this dataset and investigate the effect of the grating excitation wavelength on the local temperature rise, further data points were acquired with 266 nm pump excitation where the absorption coefficient of acetone is an order of magnitude lower than that of toluene. Measurements are acquired using 266 nm pump excitation as it is a popular pump wavelength of choice for LITGS measurements using acetone or toluene as a target species [146, 145, 150] given that the beam can be produced without a dye laser.

To produce the 266 nm pump beam, the 4th harmonic output of the Continuum Surelight Nd:YAG laser was used in the absence of the dye laser. All other optical parameters (i.e. focal length of crossing lens, pump separation etc.) remained constant. The length of the interaction region under 266 nm excitation is 6.2 mm, based on Eq.3.5 and the beam diameter is 4.1 mm. The data acquired using 266 nm excitation is presented in section 4.4.3.

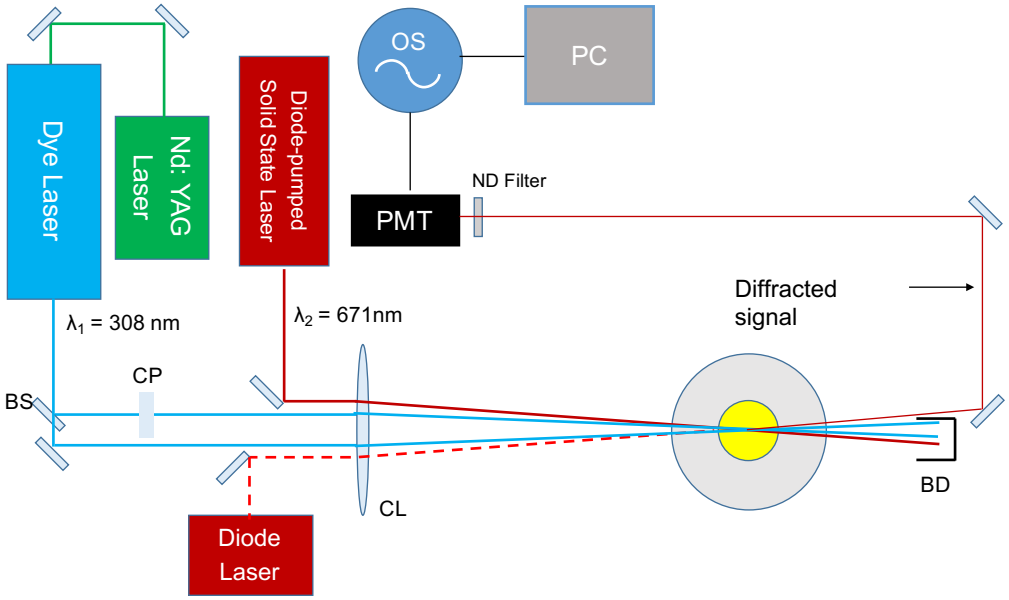

Fig. 4.1 Optical layout for LITGS acetone experiments. BS: beam splitter, BD: beam dump, f: focal length, OS: oscilloscope, PMT: photomultiplier tube.

4.3.2 Vapour/air jet

The target mixture was provided by a premixed jet of air and vapour, delivered by a laminar flow stream emerging from a 20 cm aluminium tube of 22 mm internal diameter. A primary flow line passed through a bubbler containing the vaporizing liquid at a measured temperature. The vapour concentration at the jet exit can be varied by changing the ratio between an additional dilution line flow rate and the bubbler line flow rate. The flow rates of both the primary and dilution air were controlled by Alicat mass flow controllers (20 slpm, ±0.2% full scale accuracy). The aluminium tube contains a wire-wool mesh at the base in order to enhance mixing of the saturated acetone-air and the diluent air mixture. The temperature of the jet, T_0, is measured using a K-type thermocouple and digital thermometer (RS 206-3744) 1 mm upstream of the jet exit. The temperature in the bubbler is also measured using a K-type thermocouple. The bubbler is kept in a constant temperature water bath at

293 K. Measurements are taken from the centre of the jet, about 2 mm from the jet exit, prior to any mixing with the surrounding air.

The mole fraction of the vapour at the jet exit is given by:

$$X_v = \frac{\xi X_{v,s}}{1 - X_{v,s} + \xi X_{v,s}} \tag{4.6}$$

where $X_{v,s}$ is the mole fraction of the vapour above the liquid, which is assumed to be saturated, and ξ is the ratio between the flow rate through the bubbler and the total flow rate. The derivation of Eq. 4.6 is given in Appendix 1. Saturated mole fractions at the liquid temperature are obtained from the vapour pressure values in [3] and [8], assuming atmospheric pressure.

In the present study we consider binary mixtures of acetone or toluene vapour with air, and the specific properties β for a mole fraction X_v in air are calculated as molar weighted averages:

$$\beta = \beta_v X_v + \beta_a (1 - X_v) \tag{4.7}$$

The properties used for the species considered at ambient temperature are listed in Table 4.1.

Property	Symbol	Air	Acetone	Toluene
Molecular weight (g/mol)	W	28.97	58.08	92.14
Specific heat (J/kg K)	c_p	1.005	126.60	157.15

Table 4.1 Table of properties for air [103], acetone [151] and toluene [143].

4.4 Results

Single shot LITGS signals with mixtures of air/acetone or air/toluene were recorded for a range of absorber concentrations and pump energies. The maximum pump energy available from the dye laser was 12 mJ. The minimum pump energies for which a clear LITGS signal could be obtained were 4 mJ and 1 mJ per pulse for toluene and acetone, respectively. The probe power was fixed at 300 mW for all cases, as a sensitivity analysis indicated saturation of the detector beyond that value. Sample single-shots at conditions are shown in Fig. 4.2, where pump pulse energy is changed at a fixed molar fraction of acetone. The raw signal was smoothed and the peaks and troughs identified using the procedure described in section 3.2. The period between each peak was then extracted, and an average frequency is calculated over all peaks in the signal to define a single shot frequency. For the case in Fig. 4.2, the frequency changes from 17.8 to 21.8 MHz as the pulse energy changes from 4 to 12 mJ.

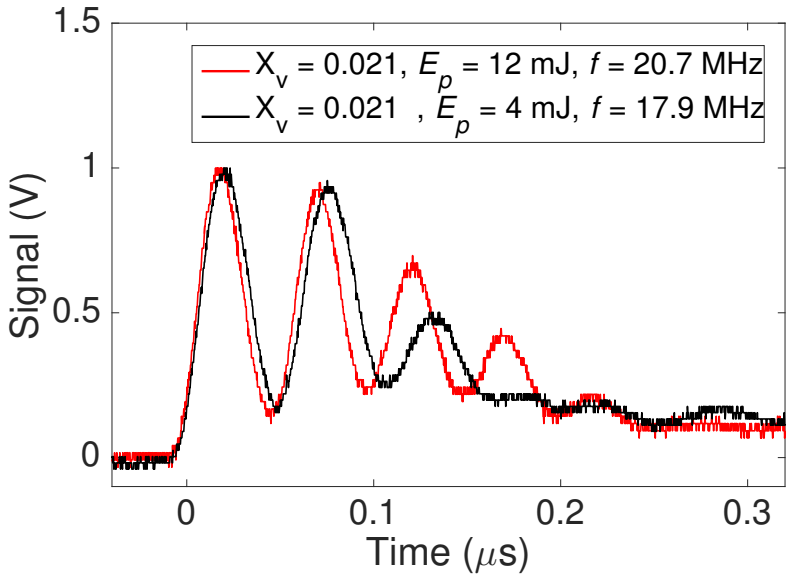

Fig. 4.2 Single-shot samples of raw signal for two cases for a fixed vapour concentration $n_v = 8.74 \times 10^{-4}$ mol/m^3 ($X_v = 0.021$) for pulse energies of 4 and 12 mJ. The frequencies measured are 17.8 and 21.8 MHz, respectively.

4.4.1 Effect of absorber concentration and pump energy on measured LITGS temperature

Figures 4.3 and 4.4 show the variation of the measured LITGS oscillation frequency and calculated temperature derived from the measured frequency as a function of tracer molar fraction for four different pump energies, for both acetone and toluene. Each data point represents the mean LITGS temperature obtained over 400 shots, with the error bars indicating the standard deviation. Both graphs show a monotonic increase in the measured temperature with absorbed energy and absorber molar fraction, as expected from Eq. (4.5).

The slope of the measured temperature with the molar fraction at a fixed energy is higher in the case of acetone relative to toluene, indicating a higher absorption cross section, or thermal conversion efficiency, as discussed further on. The main criterion for the LITGS measurement technique is that it should be non-intrusive, so that the lower energies and molar fractions should be used. Figs. 4.3 and 4.4, where data was acquired under relatively steady and uniform flow field conditions, shows that the precision suffers with an increase in pump energy. At stronger pump energies the fluctuation in the laser intensity becomes increasingly severe (measured up to 12 %), resulting in greater fluctuation of the intensity of the thermal grating, and hence the measured temperature.

The range of data points presented here was limited by the minimum amount of signal obtainable at the lowest absorber concentration/pump energy conditions for the optical configuration. As discussed in Chapter 2, to maximize the signal intensity, the probe volume should be as large as possible (i.e. long focal length crossing lens, short distance between pump beams). In this case, the optical geometry was selected to ensure that

the interaction region was shorter than the outlet diameter of the jet; the geometry was fixed for all cases. The optical geometry and range of mole fractions/pump energies used in this work were selected to be close to typical values used in previous studies where acetone/toluene-LITGS measurements are conducted [145, 147, 150].

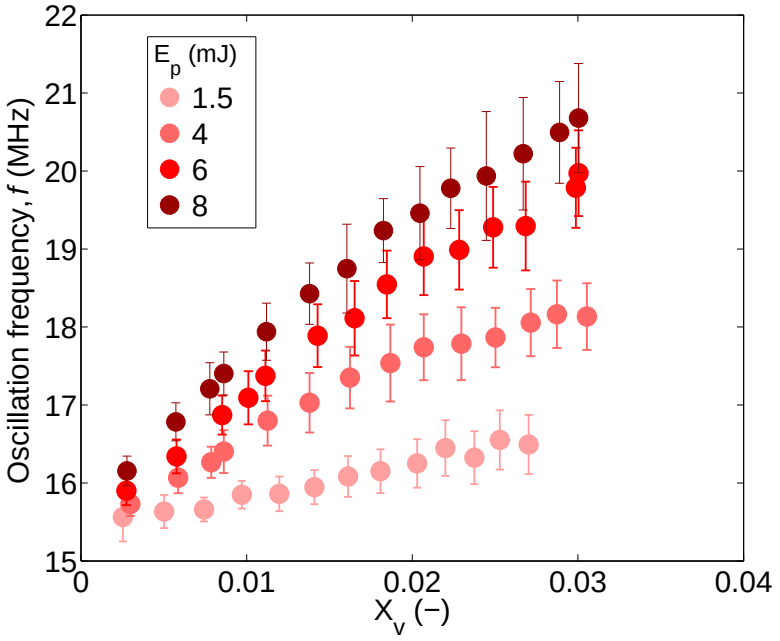

(a) Acetone

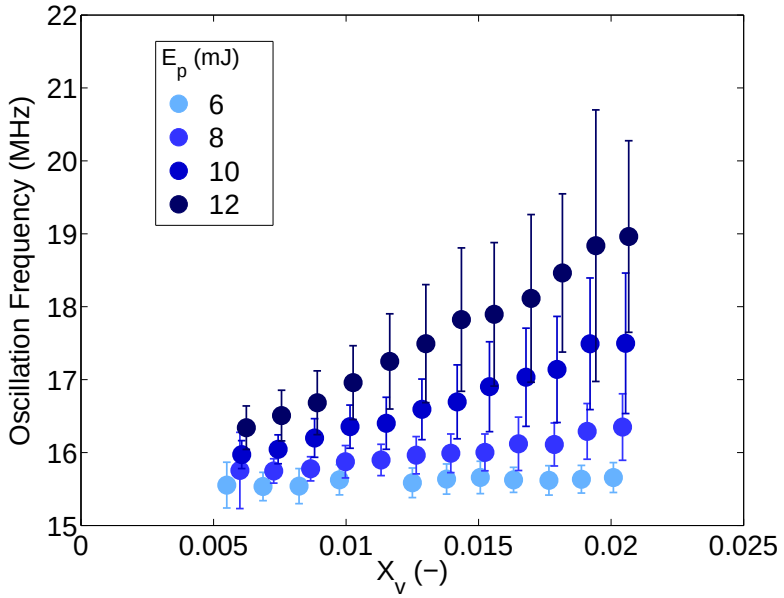

(b) Toluene

Fig. 4.3 LITGS signal oscillation frequency with increasing absorber molar fraction, for increasing pump energies. Error bars indicate root mean square fluctuations.

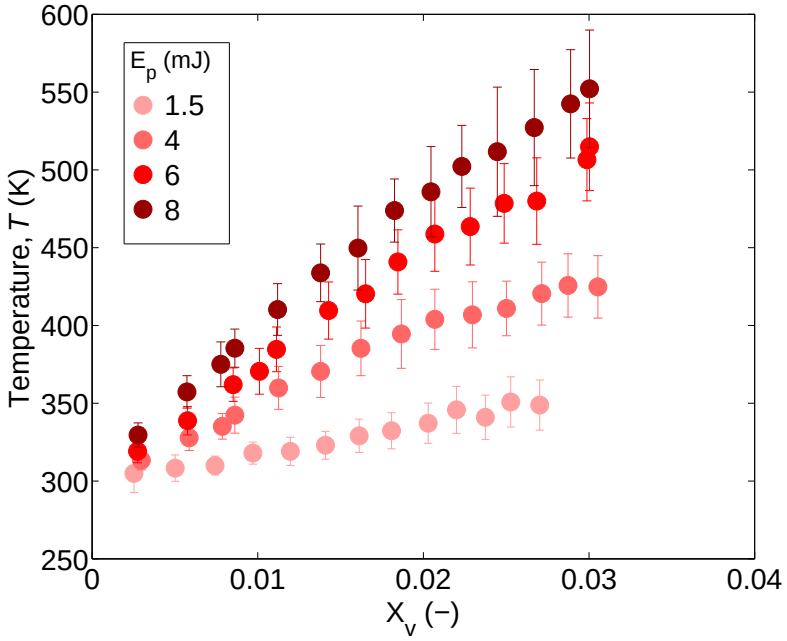

(a) Acetone, $T_0 = (293.1 \pm 0.6)$ K

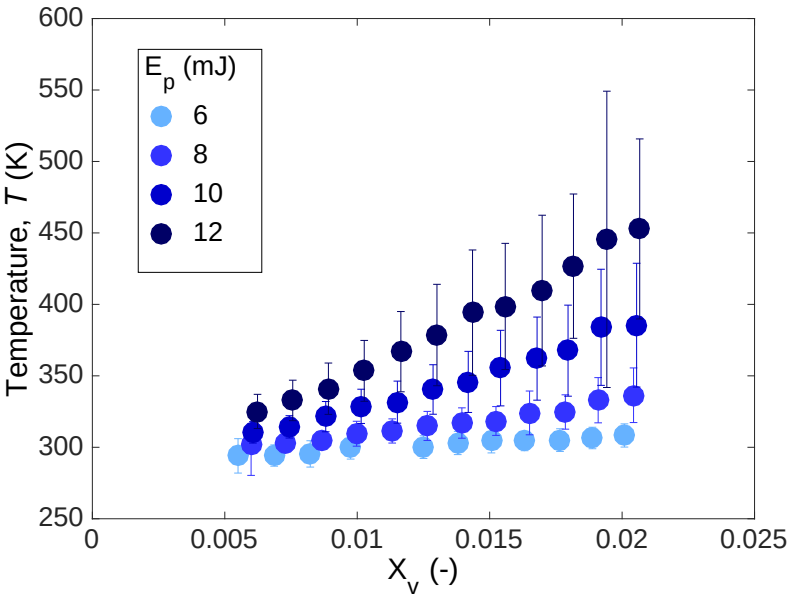

(b) Toluene, $T_0 = (292.3 \pm 0.5)$ K

Fig. 4.4 Derived LITGS temperature with increasing absorber molar fraction, for increasing pump energies. Error bars indicate root mean square fluctuations. T_0 represents mean and rms of thermocouple measurements recorded at each condition, just prior to acquiring LITGS signal.

4.4.2 LITGS temperature vs pump energy

Figures 4.5 and 4.6 show the effect of the pump energy on the measured LITGS signal oscillation frequency and derived LITGS temperature for three molar fractions.

Figure 4.6 shows that an increase in pump energy leads to an approximately linear increase in the measured temperature, with a significantly higher slope for acetone than in the case of toluene. However, the slope decreases with energy in the case of acetone at higher molar fractions, and remains approximately constant in the case of toluene.

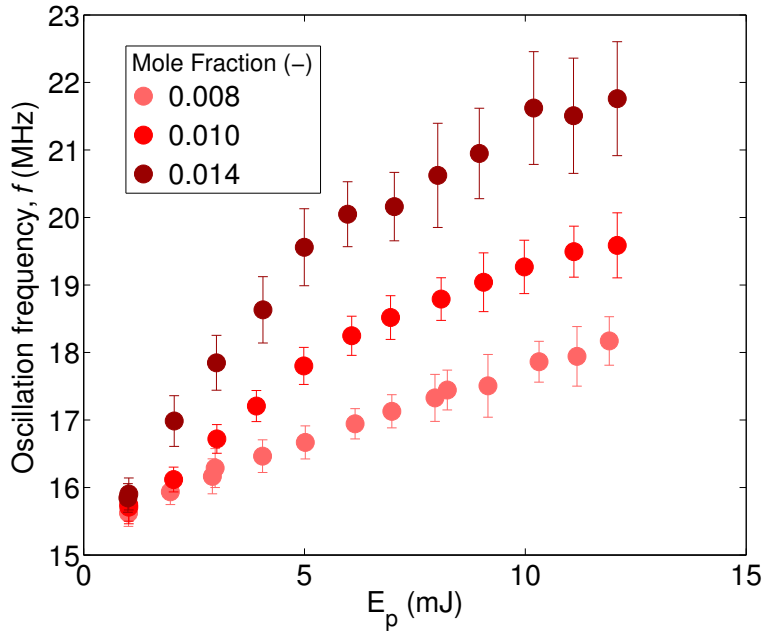

(a) Acetone

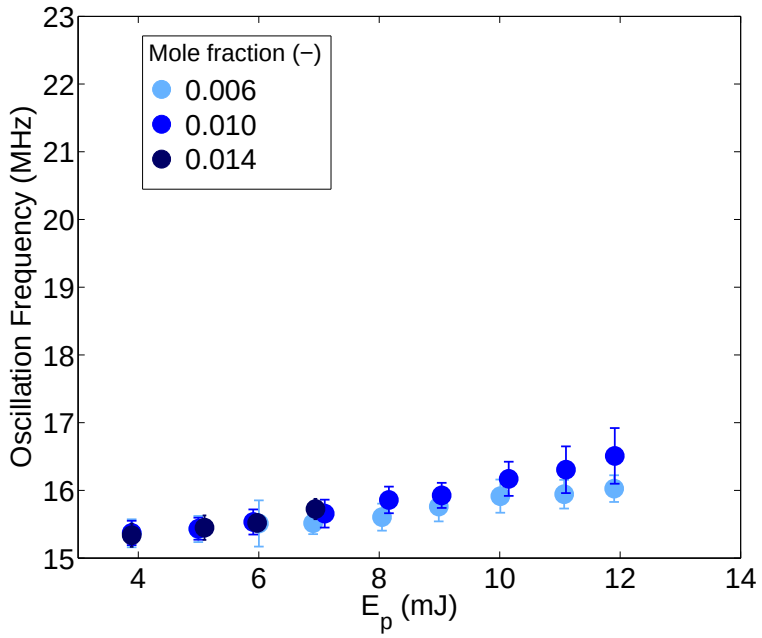

(b) Toluene

Fig. 4.5 LITGS signal oscillation frequency with increasing pump beam energy, E_p for three molar fractions

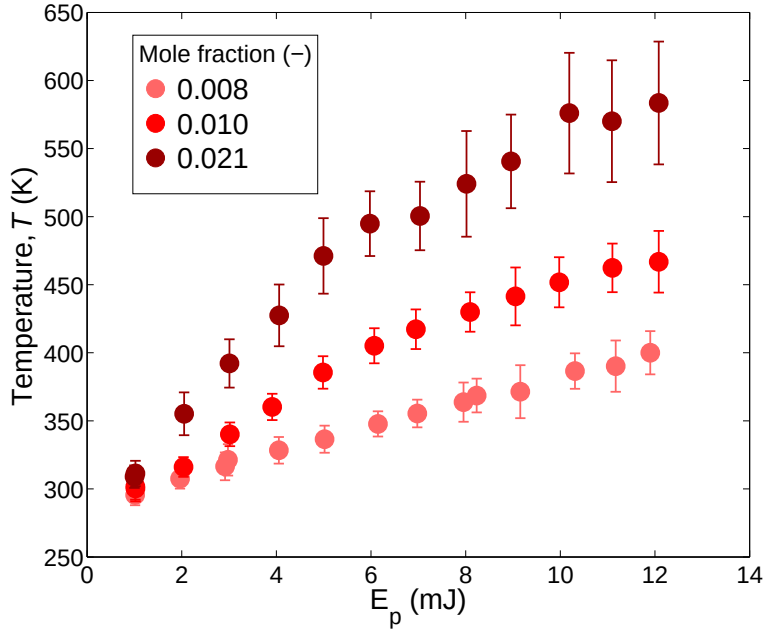

(a) Acetone, T_0 = 290.3 K +/- 0.52

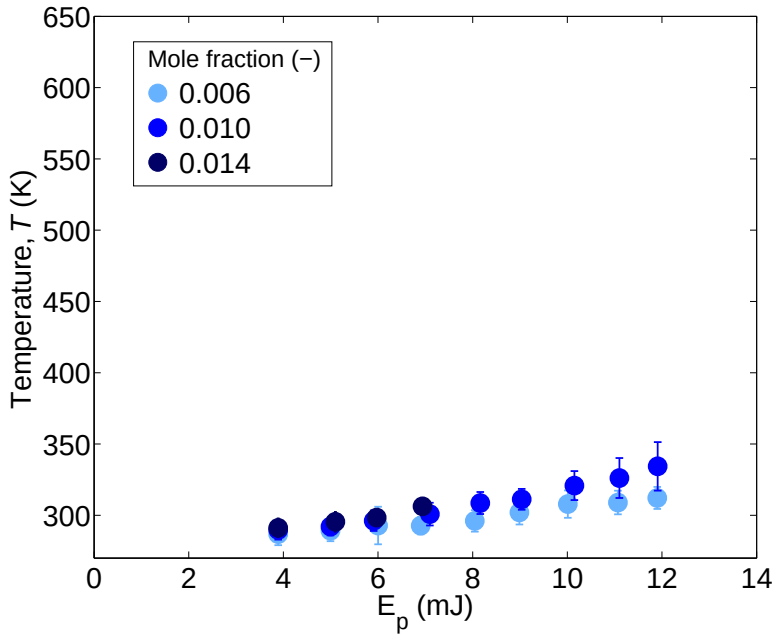

(b) Toluene, T_0 = 290.3 K +/- 0.83

Fig. 4.6 Derived LITGS temperature with increasing pump beam energy, E_p for three molar fractions

4.4.3 Supplementary data at 266 nm pump excitation

Figures 4.7 and 4.8 show the influence of the pump energy on the LITGS temperature for acetone and toluene, respectively, under two absorber mole fraction conditions where $\lambda_1 = 266nm$. In all cases under 266 nm excitation (where absorption coefficients, and hence expected signal intensities, are considerably higher for both absorbers than at 308 nm), absorber mole fractions were kept relatively low to avoid saturation of the PMT.

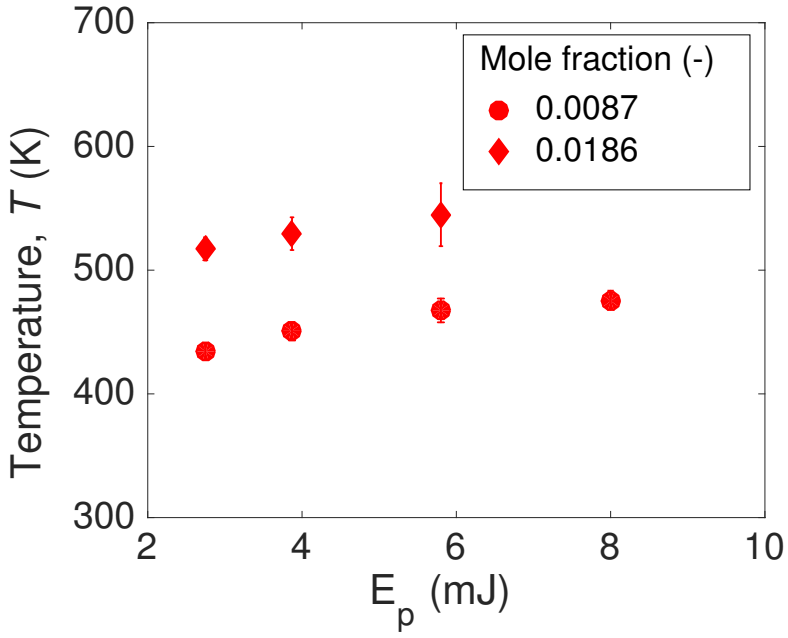

Fig. 4.7 LITGS temperature vs E_p for acetone where $\lambda_1 = 266$ nm. $T_0 = 291.1$ K

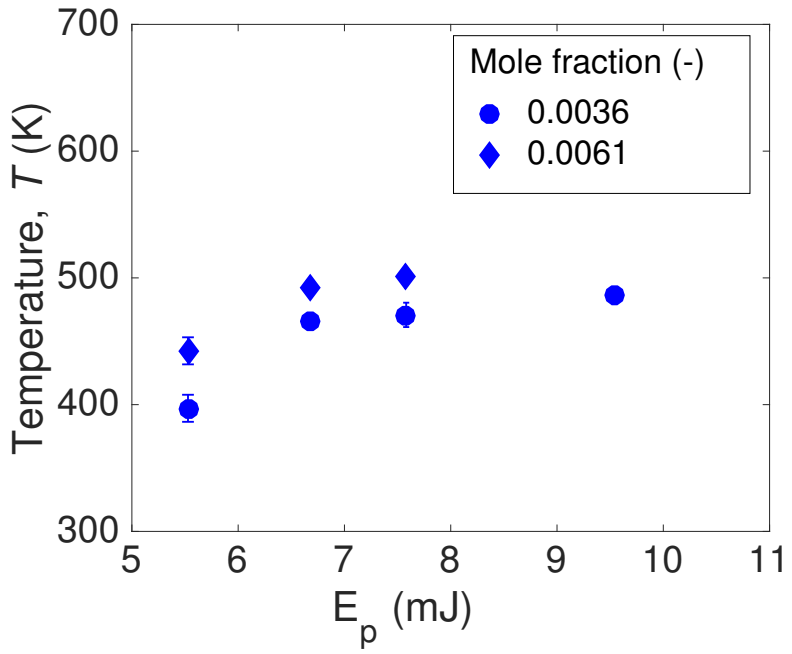

Fig. 4.8 LITGS temperature vs E_p for toluene where $\lambda_1 = 266$ nm. $T_0 = 290.7$ K

For toluene, the temperature increases with an increase in the excitation energy up to around 7 mJ before flattening. This suggests that the deposition of heat due to collision saturates beyond a certain value of the product of the laser intensity at focal point and absorber mole fraction as discussed further below (see Fig. 4.10).

4.4.4 Temperature rise

The normalized temperature rise, $\frac{\Delta T}{T_0}$ is plotted against $\frac{E_p \mathcal{A}}{\bar{c}_p T_0} \frac{\sigma}{A} X_v$ (see Eq. (4.5)) in Figs. 4.9 and 4.10 for acetone and toluene, respectively. For data acquired using 308 nm pump excitation, the value for σ is the value measured at 308 nm for acetone, $\sigma = 1.6 \times 10^{-20}$ cm^2 [72] and at 300 nm for toluene, $\sigma = 2.6 \times 10^{-20}$ cm^2[154]. Values at 308 nm are not available for toluene. For the supplementary data obtained with 266 nm excition (black points), the values of σ for acetone and toluene are $\sigma = 4.4 \times 10^{-20}$ cm^2 [72] and $\sigma = 2.5 \times 10^{-19}$cm^2 [154], respectively. The values of the mean mixture density and c_p are calculated according to the local temperature, T_0.

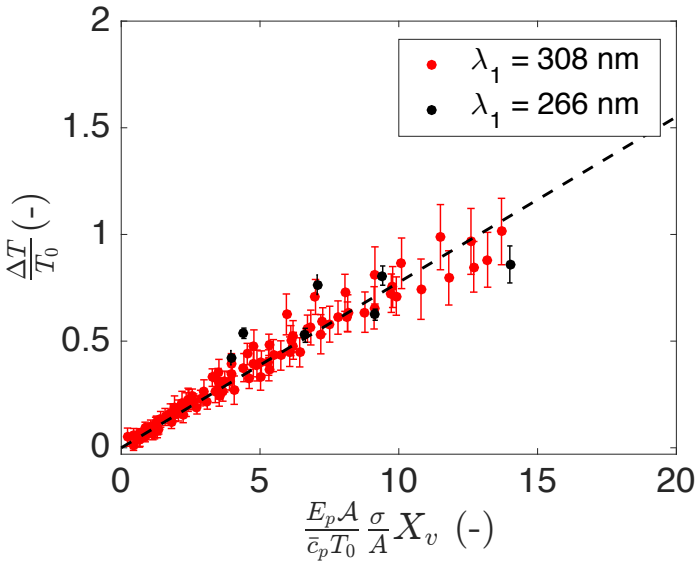

Fig. 4.9 Normalized local temperature rise vs product of intensity at focal point and absorber mole fraction for acetone/air mixtures. Dashed line represents line of best fit through all points. $R^2 = 0.97$

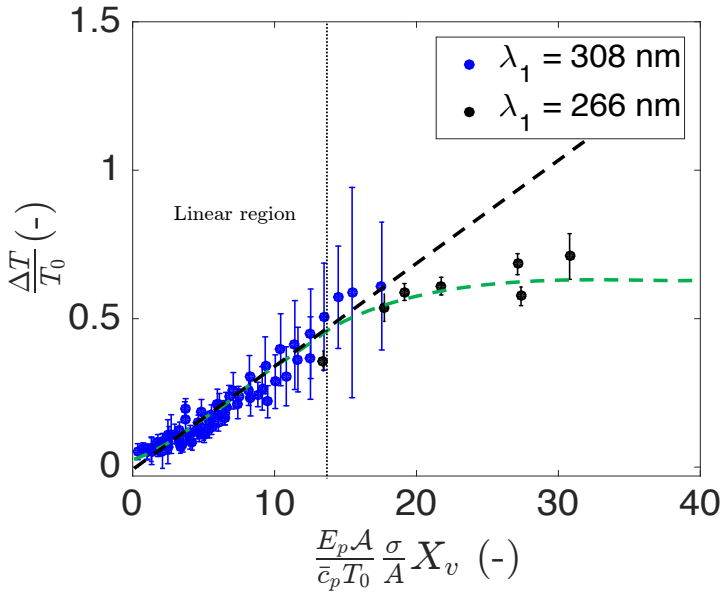

Fig. 4.10 Normalized local temperature rise vs product of intensity at focal point and absorber mole fraction for toluene/air mixtures. Dashed green line represents a non-linear logistic fit through all points. Dashed black line represents linear fit through points below saturation point

Figure 4.9 shows that the product of the incident pump energy, absorber mole fraction and the ratio of σ to A are proportional to the local temperature rise associated with the thermalization process where acetone is the target absorbing species. The gradient of the linear fit, which provides a measure of the overall efficiency of conversion of the incoming energy to thermal energy, is $\eta = 0.078$ for acetone. In the case of toluene, Fig. 4.10 shows that the temperature rise increases approximately linearly with the same parameters (with an overall efficiency, $\eta = 0.044$)) before reaching a saturation point at $\frac{E_p \mathcal{A}}{\bar{c}_p T_0} \frac{\sigma}{A} X_v \approx 13.64$, beyond which any further increase in the pump energy or absorber mole fraction leads to a constant value of probe volume heating. Whilst the absorption cross section for toluene is higher than that of acetone for both excitation wavelengths, the conversion efficiency of the absorbed energy to heat is higher for acetone.

In a molecular relaxation event, a proportion of the laser energy incident on the absorbing molecules is converted to thermal energy via collisions [28, 99]. According to Eq. 4.2, the number density of the absorbing molecules present in the interaction region, and the incident laser power determines the total amount of energy absorbed, and hence the heat deposition to the bulk gas. Whilst neither acetone nor toluene can provide truly non-intrusive measurements as target species, Figs. 4.9 and 4.10 suggest that LITGS signals can be acquired with reduced thermally intrusive effects over a wider range of concentrations when toluene is selected. As such, toluene can be considered a more suitable absorber, particularly in scenarios where the concentration of the absorbing species is fluctuating. The detailed photochemistry of acetone has been studied in some depth [46], however the photochemical decomposition mechanisms of toluene following molecular excitation is still relatively unknown. A qualitative description of the different photo-physics of acetone and toluene presented by Williams et al. [146] suggests that the longer time taken for the LITGS signal to reach its maximum value for toluene is indicative of a longer quench (thermal collision) time for toluene compared with acetone (see Fig. 4.11). Further detailed analysis of the photo-chemical processes that govern the extent to which toluene molecules thermalise, relative to the extent at which non-radiative relaxation processes dominate de-activation, may provide insight into the processes that govern the saturation observed above.

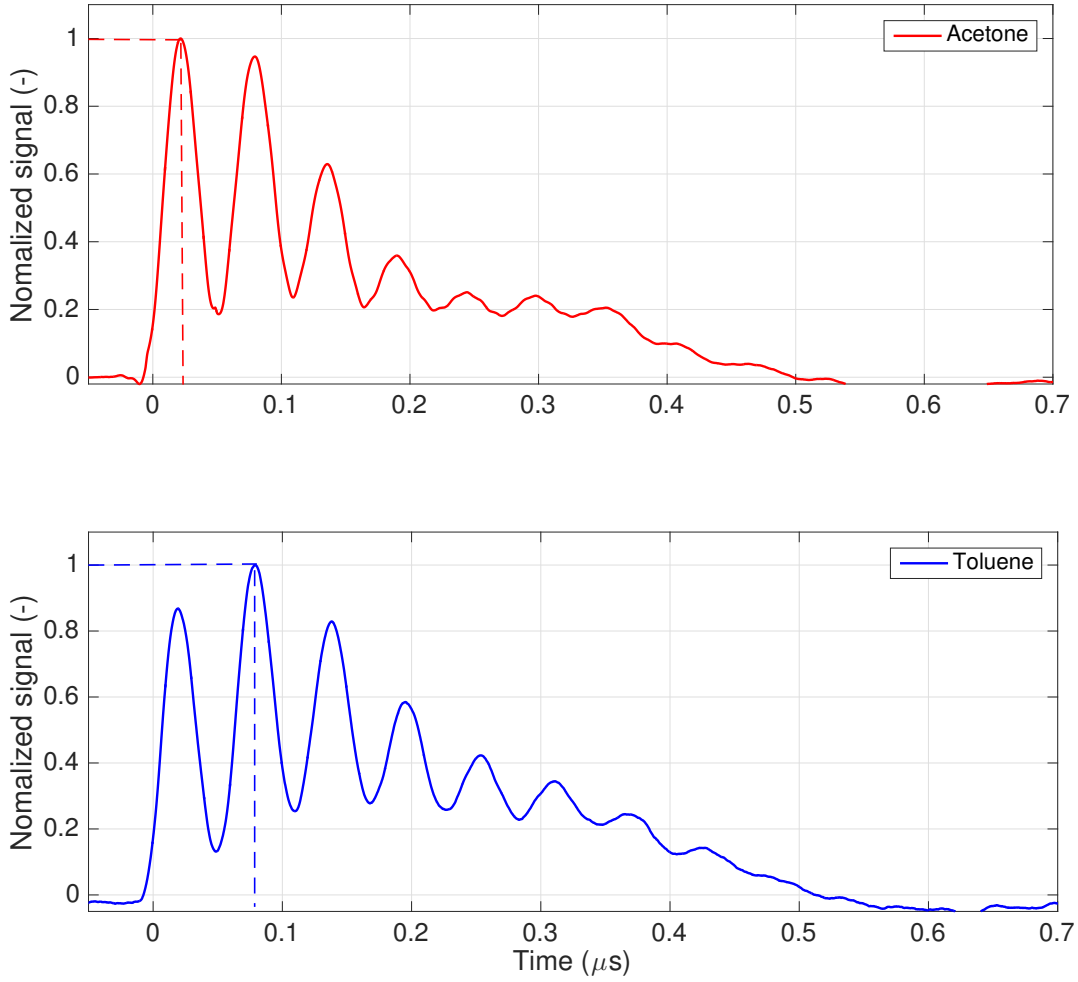

Fig. 4.11 Typical single shot examples in acetone (red) and toluene (blue) acquired using 308 nm excitation. Toluene takes around 100 ns longer to reach maximum intensity.

Effective LITGS measurements rely on the temperature rise within the probe volume to be sufficiently high to create a density perturbation that allows for signal detection, yet low enough to be remain within an acceptable degree of accuracy. For measurements in mixtures of acetone/air and toluene/air, Eq. 4.5 can be used to predict the local temperature rise in the linear ranges for a given optical geometry, pump energy and

absorber mole fraction. The range of pump energy/absorber mole fraction conditions at which LITGS signal was acquired in this study are similar to typical conditions used in previous experiments that report LITGS measurements using toluene or acetone as target species, with the most recent work by Willman *et al.* [150] where toluene-LITGS is employed for 1D multipoint measurements in gas flows of nitrogen seeded with around 2% toluene. In that study, differential heating in the measurement region as a result of absorption from the pump beams is discussed and further calibration to account for the influence of local heating was performed under conditions where higher concentrations of toluene were required to obtain signal. Future studies employing LITGS with acetone or toluene as a target species should minimize laser heating effects by using the lowest pump energy required to obtain signal and careful consideration should be taken in minimizing variations in the concentration of the target species over the measurement time.

4.5 Summary

Quantitative measurements of temperature in a continuously flowing jet have been demonstrated using laser induced thermal grating spectroscopy, where acetone or toluene are used as target absorbing species. The local temperature rise due to LITGS has been measured as a function of the incident pump energy and target species mole fraction for both absorbers. Results indicate that under the range of conditions tested in this work, which reflect typical energies and absorber mole fractions employed in previous LITGS experiments, heat deposition from the thermalization process increases linearly with the product of the incident pump energy, absorber mole fraction and

the ratio of σ to A for both absorbers. However, in the case of toluene/air mixtures, saturation of the temperature rise is observable for conditions where $\frac{E_p \mathcal{A}}{\bar{c}_p T_0} \frac{\sigma}{A} X_v > 13.64$.

For identical optical geometries, probe power and PMT gain, toluene requires higher pump energies for suitable signals by comparison to acetone, but exhibits a lower measured temperature rise with pump energy and mole fraction. At 308 nm excitation, the estimated absorption cross section for toluene is slightly higher than acetone, however, results show that the efficiency of conversion of absorbed energy to thermal energy is higher for acetone than toluene. Given that toluene is less susceptible to significant localized heating within the probe volume, it may be considered a more appropriate choice of absorbing species for LITGS temperature measurements in vapour/air flows at atmospheric conditions.

Results show that the LITGS technique can provide temperature measurements in acetone and toluene vapour flows with an accuracy and precision of less than 1% (based on temperature measurements shown in section 4.4) provided that the parameters that contribute to the local temperature rise due to the thermalization process are carefully considered to minimize intrusiveness, whilst obtaining sufficient signal. In summary, to obtain measurements that remain non-intrusive, one needs very small controllable pump powers and target species concentrations (of the order of ppm), but somehow increased SNR to detect the disturbance in the probe volume due to LITGS. This underlines the importance of ensuring that the alignment procedure produces a very good interaction zone (i.e. strong overlap) between the pump and probe beam, and a high power, low noise probe beam.

In the experiments presented in this chapter, the absorber quenching partner (i.e. molecules that the absorbing species collide with to induce collisional de-activation and subsequent thermalization) was restricted to air in all cases. Further work could extend

the current data set to include other absorbers or dilution gases to further understand the influence of the quenching partner on thermalization. In addition, parameters that affect η (the efficiency of conversion of incoming energy to thermal energy for a given) should be further investigated with the aim of constructing a more generalized model that can be applied to other absorbing species.

Chapter 5

OH-LITGS in high temperature, high pressure combustion

5.1 Chapter overview

This chapter demonstrates temperature measurements using LITGS in laminar premixed oxygen enriched $CH_4/O_2/N_2$ and CH_4/air flames at elevated pressure. Oxygen enriched flames provide an environment in which to test the robustness of LITGS at elevated temperatures (up to 2900 K). The wavelength of the pump beam was set for the OH(1,0) band excitation [108]. The magnitude of the LITGS signal is expected to increase with density, making it a promising technique for temperature measurements at high pressure. In this study, we show that LITGS signal can be successfully acquired at 0.5 MPa, for both high temperature oxygen enriched flames and CH_4/air flames. The primary parameters that influence the quality of LITGS signal were also investigated. The signal contrast, which acts as a marker for the strength of the frequency oscillations, is shown to increase with an increase in the burnt

gas density at the measurement point. Generating thermal gratings in higher density mixtures leads to increasingly rapid de-activation of the excited molecules due to a higher rate of collisions (i.e. collisional quenching), which leads to a stronger acoustic perturbation and ultimately, stronger oscillations in the signal.

5.2 Motivation and review of previous work

Internal combustion engines such as rocket motors, reciprocating engines and gas turbine combustors operate under high pressure conditions in order to increase efficiency and power density. Enhancing our understanding of combustion phenomena at high pressure is essential in improving practical combustion systems. This is particularly true in the case of rocket motors, where H_2/O_2 combustion is employed at extremely high pressures, often of the order of 10 MPa [158, 90]. However, the measurement of combustion parameters in rocket motors is particularly challenging due to the high pressure and high temperature conditions.

The high pressures prevalent in gas turbines and rocket systems create significant challenges for optical diagnostics. Whereas on one hand, the higher concentrations can help produce stronger signal due to the greater number of molecules per unit volume interacting with light, countervailing effects can reduce the signal to noise ratio of the techniques, including: (a) background radiant interference from intense chemiluminescence, which interferes with spectroscopic diagnostics such as fluorescence or Rayleigh scattering, (b) line broadening from techniques which rely on a well defined spectrum, such as OH-PLIF and CARS, (c) increased signal quenching from collisions, particularly in the case of fluorescence [128, 134]. Despite the challenges, temperature measurements in high pressure combustion have been attempted using established laser-

based approaches with some success. Examples include spontanous Raman scattering [15, 74], LIF [73, 128] and variants of the CARS technique [4, 55, 44, 138].

LITGS offers a number of distinct advantages over other laser-based methods, particularly for high pressure conditions: (a) the inherent precision of a frequency-based measurement is high, and independent of intensity-based inaccuracies [124]; (b) the signal intensity increases with pressure [22]; (c) the temperature can be determined quantitatively without the need for calibration against reference values; (d) the output signal in the form of a cw monochromatic coherent beam, and can be transferred over long distances away from the probe region, allowing for the separation of signal from interference; (e) it offers sufficient time resolution (less than 1 μs) for measurements in turbulent flames. The main disadvantages are (i) the need for sufficiently high concentrations of species which can absorb in the available wavelengths for pulsed lasers – whereas this is straightforward for reacting species, this is more challenging for product species, whose bands are primarily in the infra-red; (ii) the rate of energy transfer process between the excited species and the bath gases, which can limit the signal available, (iii) the need for alignment of three beams.

Despite the growing interest associated with LITGS measurements, only three studies have used LITGS for measuring product gas temperatures. This occurs because there are few species in accessible regions of the electromagnetic spectrum with sufficient concentration in the product gas: few product species absorb in the visible and near UV, where inexpensive pulsed solid state and dye lasers operate. Conversely, there are few pulsed sources that can access the deep infra red regions where, for example, water and carbon dioxide absorb. Absorption by the hydroxyl radical OH around 307 nm was used in measurements of product temperature over a porous flat-flame burner stabilized using H_2/O_2 at atmospheric pressures [148], and CH_4/air mixtures

under pressures of up to 40 MPa [82]. More recently, Sahlberg *et al.* obtained LITGS signals over an atmospheric pressure ethylene flame using infrared absorption around 3.2 μm for the fuel itself and H_2O to generate the thermal grating. In the experiment, the temperature could be evaluated from ethylene (fuel) absorption for the unburnt reactants mixture and H_2O (products) for the burnt gas, demonstrating the potential of using LITGS measurements to determine the structure of the flame front [111].

The purpose of this study is to demonstrate the capability of LITGS using OH excitation for product gas temperature measurements in high pressure, very high temperature flames for a range of conditions. In order to acquire LITGS signal in high temperature flames (compared to the study by Latzel et al. [82]), oxygen enriched flames were used, which generate large concentrations of OH. Unlike the previous studies on OH-LITGS, this study reports measurements of temperature under a range of flame conditions for a fixed pressure of 0.5 MPa and the various factors that influence the quality of the LITGS signal with increasing temperature are also investigated.

5.3 Experimental set-up

5.3.1 Absorber selection - OH

The hydroxyl radical (OH) is an intermediate radical species produced during the combustion of hydrocarbon fuels [66]. It has been a popular target species for a number of absorption-based laser diagnostic techniques in combustion [58] [80]. Several of its characteristics have made it favorable over other products of combustion that also exhibit strong absorption properties. Most notably, in hydrocarbon-air flames, OH forms in the flame front, and its distribution can act as a marker for heat release [47]. The absorption characteristics of OH are well known [24] and the spectrum in the accessible UV region is shown in Fig. 5.1.

OH was selected as a suitable target species for LITGS measurements of burned gas temperatures in this work for the following reasons:

1. Strong absorption cross section in UV.
2. It exists in relatively high concentrations in CH4/O2/N2 flames and increases in concentration with oxygen enrichment. This is important, given that this work targets high temperature flames and the LITGS signal suffers with an increase in temperature.
3. It is an important species of interest in combustion diagnostics.
4. It is a product of combustion and does not need to be seeded into the flame.
5. It is fairly long-lived, so it can be found throughout the post-flame region.

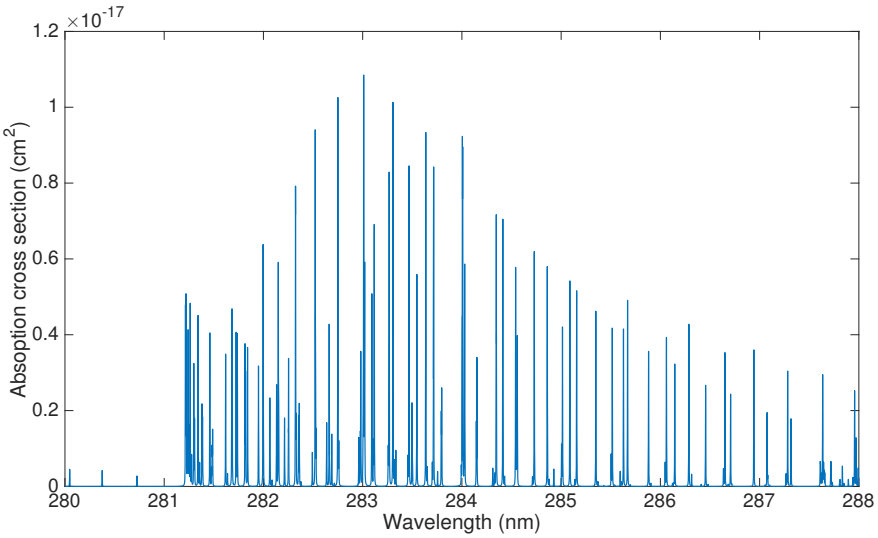

Fig. 5.1 UV absorption spectrum for OH(1,0) band [24]

5.3.2 Optical layout for 283 nm OH excitation

Figure 5.2 shows a schematic diagram of the experimental setup used in this study. High pressure combustion experiments were carried out using the test facility at the Institute of Fluid Science, Tohoku University. Details of the test facility have been described elsewhere [70]. Figure 5.2a shows the schematic layout of the optical geometry through the high pressure chamber. An Nd:YAG laser (Spectra-physics, GCR-250) pumping a frequency doubled dye laser (Lumonics, HD500+HT1000) was employed to obtain a pump beam set to a wavelength of 282.929 nm for OH(1,0) band excitation. The pump energy for OH excitation was set to 11 mJ. The pump beam was split using a 50:50 beam splitter to separate two pulses before the beams are introduced into a 1000 mm focal length crossing lens at an incident angle, $\theta_p/2$.

A CW semiconductor laser, operating at a wavelength of 445 nm (RGB laser system, NavoPro PB 445-1000 MM) was employed as the probe beam. The power for the probe

beam was set to 810 mW. The beams that pass through the high pressure chamber were stopped by a beam dump. The diffracted signal (LITGS signal) was detected using a photo multiplier tube (PMT, Hamamatsu Photonics, R928). The LITGS signal was acquired using an oscilloscope with a sampling rate of 5 GS/s and 150 MHz bandwidth (GwInstek, GDS-3154). At least 30 single shots of LITGS signal were acquired for all examined conditions.

The pump beam diameter at the crossing lens was measured in order to accurately evaluate volume of the crossing point and was found to be slightly elliptical in shape. The length of major and minor axes were 4.81 mm and 3.82 mm, respectively, assuming that the intensity of the laser beam has a Gaussian profile. In this study, the distance between the two pump laser beams was set to 10 mm and thus the incident angle, $\theta_p/2$ was 5.0 mrad.

The length of the intersecting region of the two pump beams (i.e. the measurements volume) can be calculated using Eq.'s 3.2 - 3.5. Assuming that the pump beams are Gaussian, the dimensions of measurement volume are $d_x = 94.8$ μm, $d_y = 94.8$ μm and $d_z = 17.0$ mm. Since a lens with 1000 mm focal length was employed in this study, the value of d_z is relatively large. However, the actual volume of the measurement point is the intersecting region of the two pump beams and the probe beam. Hence, the actual measurement volume is smaller than those implied by the values above. In this study, measurements were performed at the center of the burner, where the temperature gradients within the measurement volume are expected to be small according to the OH-PLIF flame observations that will be shown in Section 5.4.1.

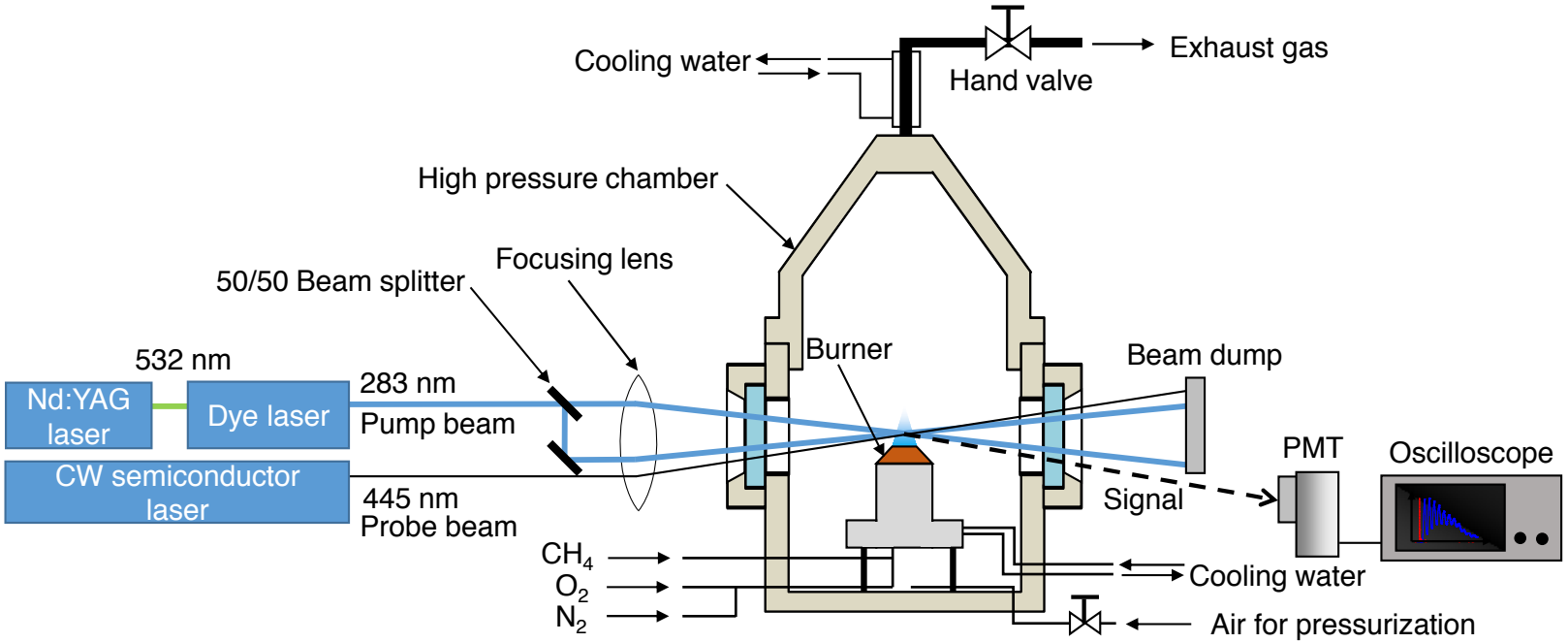

Fig. 5.2 Schematic diagram of the experimental setup for OH-LITGS measurements at high pressure.

To confirm the existence of OH in the measurement region, additional supplementary OH-PLIF experiments were performed, using the same pump and dye lasers. The output wavelength of the dye used in OH-PLIF measurements was also 283.929 nm, producing 11 mJ/pulse. The beam was reshaped using sheet-forming optics before being directed through the flame. The fluorescence was imaged using an intensified CCD camera (Andor, USB iStar) and produced images with a pixel resolution of 0.068 mm/pixel.

5.3.3 Pressure chamber

A schematic diagram of the structure of the high pressure chamber at the Institute of Fluid Sciences, Tohoku University, is shown in Fig. 5.3. The high pressure facility described briefly here, but for further details, the reader is referred to [71].

The chamber's internal cylindrical structure has an inner diameter of 498 mm and is an inner length of 600 mm. A conical lid attachment extends the the inner length of the chamber. It also acts to minimize flow disturbances and heating of the top of the chamber caused by the exhaust gas flow. When the conical lid is attached, the inner length of the chamber is 1150 mm. Nine cylindrical quartz observation windows (50 mm in diameter, 10 mm thickness) are available around the chamber. The chamber can be pressurized up to 10 MPa.

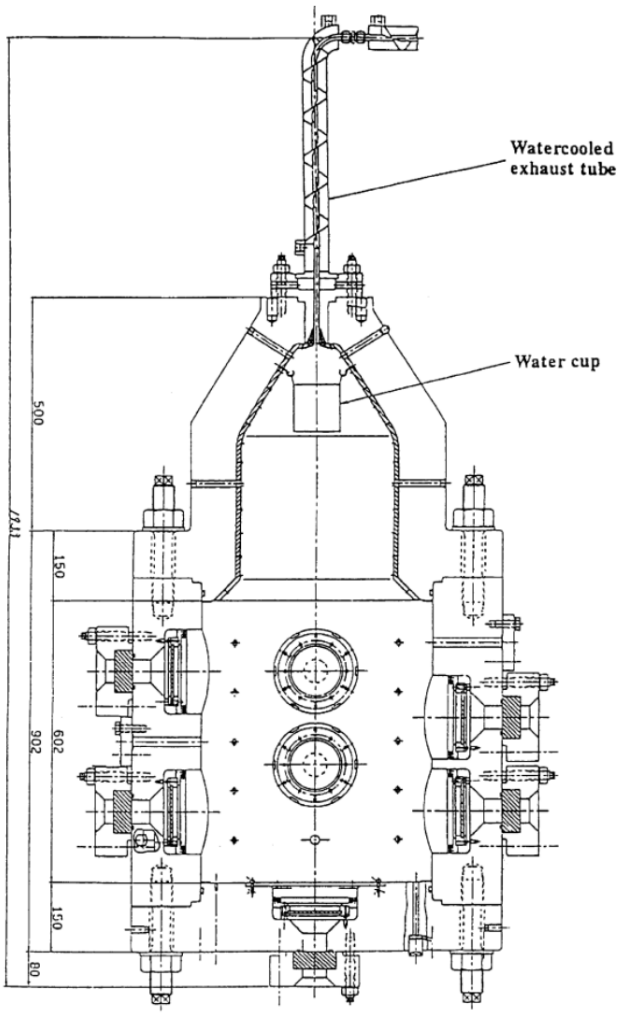

Fig. 5.3 Structure of high pressure chamber at IFS [71]

To pressurize the chamber, air is supplied from a tank (4.5 MPa and 7.5 m^3) and a high pressure compressor. Fuel is supplied from pressurized gas cylinders and flow rates are measured using calibrated-orifice flow meters. The pressure in the chamber is maintained at a constant value by adjusting the exhaust valve and the exhaust tube is water-cooled.

To ensure that the chamber does not fill up with exhaust gas and maintain a cool temperature, additional air is also supplied to the upstream (lower) part of the chamber.

The temperature of the mixture and the temperature profiles inside the chamber are measured by thermocouples and monitored, along with pressure, at a separate control panel. An automatic stage controlled outside the chamber is installed in the high pressure chamber to move a glow plug igniter. To observe the flame during experiments, CCD video cameras were placed either side of the chamber and directed through two available quartz windows.

5.3.4 Burner design

CH_4 (purity: 99.9 %) was selected as the fuel, O_2 (purity: 99.7 %) was used as the oxidizer and N_2(purity: 99.998 %) was used as a diluent. The flow rates were controlled using an orifice and mass flow meter. A high pressure calibration burner for high pressure and high temperature flames designed by Takeuchi *et al.* [129] was employed in this experiment. Figure 5.4 shows a photo of the nozzle of the calibration burner. The burner nozzle was made of oxygen free copper and was water cooled. The nozzle has 240 holes, each with a diameter of 0.7 mm. All holes are drilled within a 19 mm circular exit. Further details on the burner can be found in [129]. The length of the sampling volume region was similar to the nozzle diameter. The measurement points were 15 mm downstream of the burner surface for the oxygen enriched flame and 7 mm downstream for the methane/air flame.

All experiments were performed at pressures, P, of 0.5 MPa and reactant temperature of temperature 298 K. The equivalence ratio, ϕ, was varied from 0.45 to 0.95 and the dilution ratio, ξ_N is determined using:

$$\xi_N = \frac{Q_{\mathrm{N_2}}}{Q_{\mathrm{N_2}} + Q_{\mathrm{O_2}}}. \tag{5.1}$$

Here Q_{N_2} and Q_{O_2} are the volumetric flow rates of nitrogen and oxygen, respectively. According to this definition of the dilution ratio, $\xi_N = 0.79$ corresponds to air. For oxygen enrichment (and hence high temperature flames), the dilution ratios used in this study were set to between 0.55 to 0.79. The flow rate and Reynolds number for the largest flow rate condition (P = 0.5 MPa, $\xi = 0.55$, $\phi = 0.8$) was 24.9 L/min and 632, respectively. Flow rates for other conditions were smaller than this value, so the flow can be considered laminar for all cases.

Numerical simulations were performed using CHEMKIN-PRO [104]. GRI-Mech 3.0 reaction mechanisms [119] to determine species and temperatures.

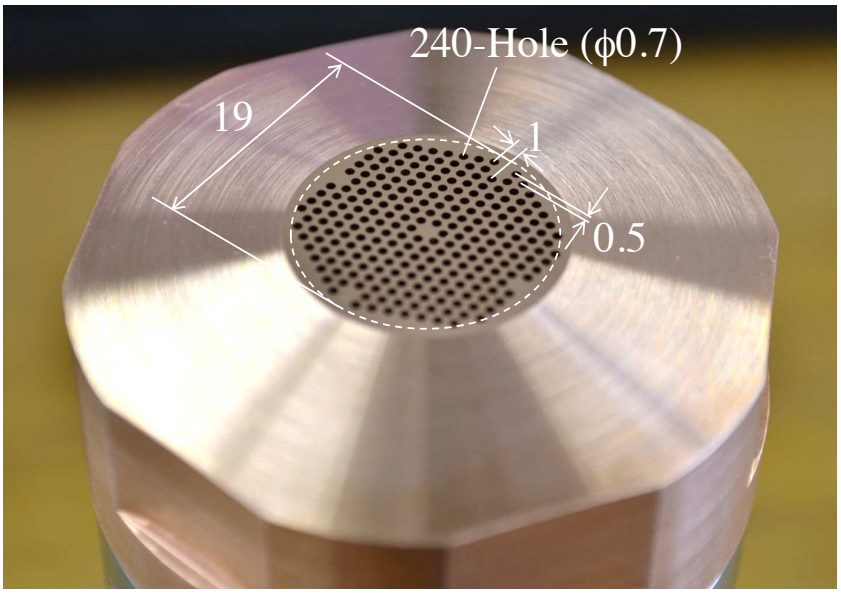

Fig. 5.4 Photograph of the burner nozzle.

5.4 Results

5.4.1 Flame structure

Figure 5.5 shows the simulated flame structure of a methane flame, for a pressure $P = 0.5$ MPa and equivalence ratio $\phi = 0.8$. In both graphs, the origin is set as the position of maximum heat release rate. The flame thickness is of the order of a hundred micrometres, owing to the high pressure conditions. Under oxygen-enriched conditions (Fig. 5.5(a)) the flame temperature peaks at around 2800 K before approaching an equilibrium state, and the OH mole fraction, X_{OH} in the product gas is around 0.028. For a similar equivalence ratio in simulated air (Fig. 5.5(b), dilution ratio, $\xi_N = 0.79$), the flame temperature is only around 2000 K and the product OH mole fraction hovers around 0.0013. Simulations conclude that the enriched oxygen flame thus significantly increases the OH levels. Both product levels and temperatures are close to equilibrium less than a millimetre away from the flame front, as shown by the dashed lines.

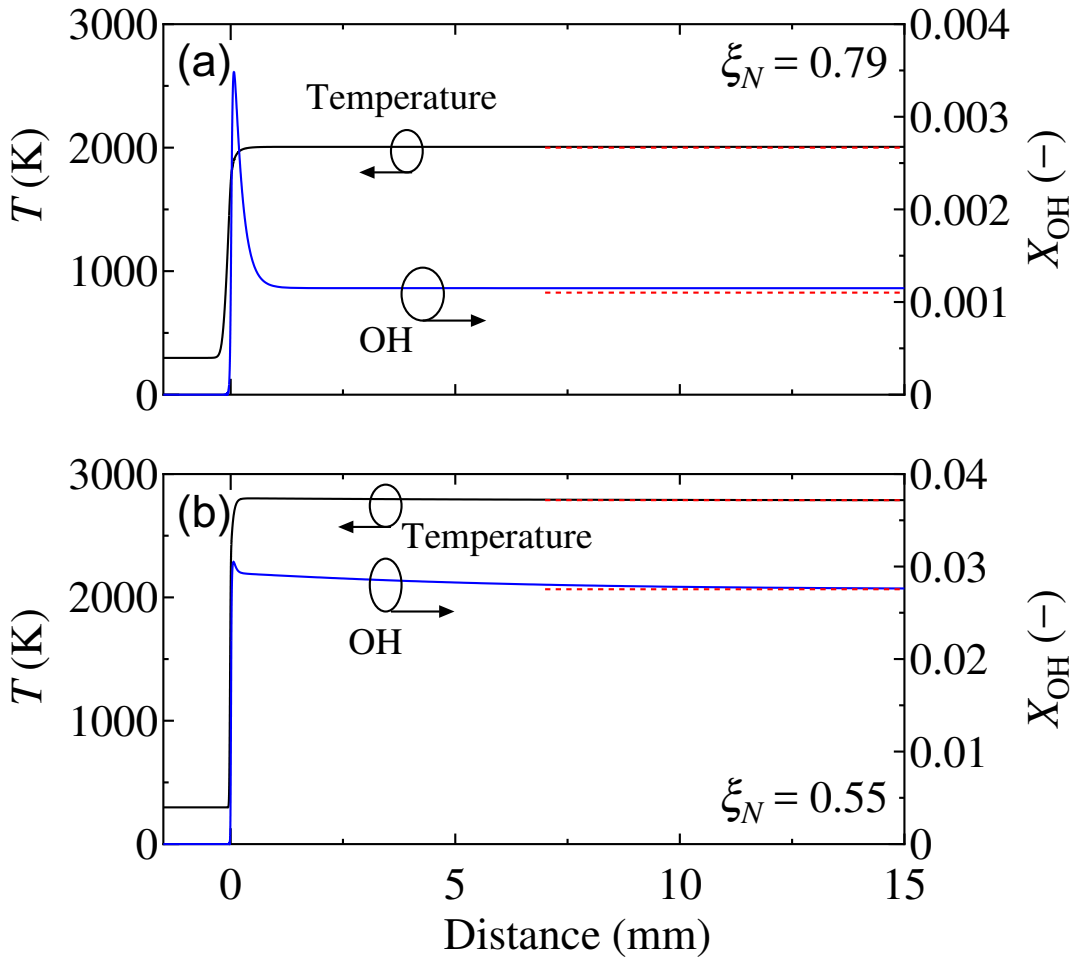

Fig. 5.5 Flame structure obtained from one-dimensional numerical simulation at pressure, P, of 0.5 MPa and equivalence ratio, $\phi = 0.8$. Here, dashed red line in the figure corresponds the equilibrium states of temperature and OH mole fraction: (a) Dilution ratio, $\xi_N = 0.79$. (b) Dilution ratio, $\xi_N = 0.55$.

Figure 5.6 shows how the mass concentration, ρ_{OH} and mole fraction, X_{OH}, of OH at the measurement point vary under the conditions of interest, based on the numerical simulations. Figure 5.6(c) shows the effect of the flame equivalence ratio under an oxygen enriched condition ($\xi_N = 0.55$). Whilst the mole fraction and density of OH at the most lean condition in this study are low, they are considerably larger than in the case of CH_4/air flames, as shown in Fig. 5.6(a).

Although the bulk mixture density decreases with the increase in temperature arising from the lower dilution rate or increase in equivalence ratio, the OH mass concentration increases due to the increase in OH mole fraction. This is necessary to obtain suitably large signal for LITGS from OH absorption.

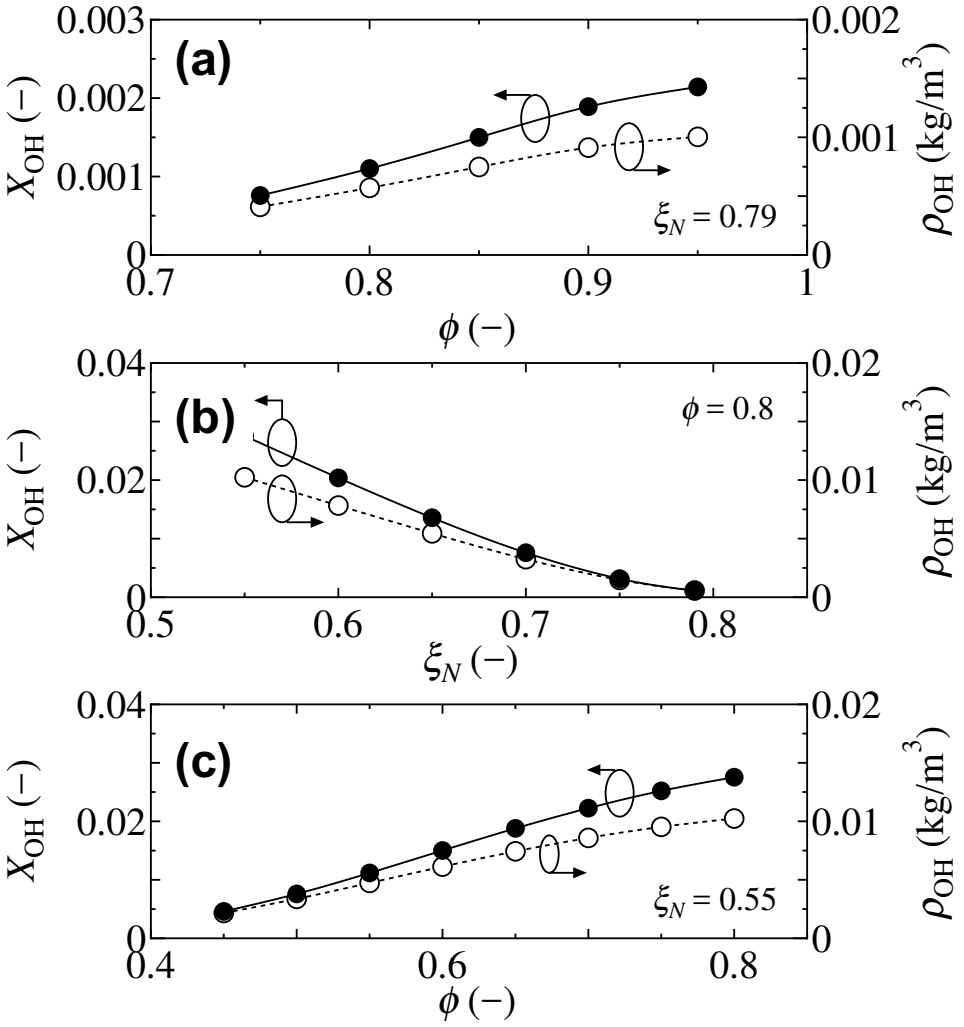

Fig. 5.6 Mole fraction of OH, X_{OH}, and density of OH, ρ_{OH}, at $P = 0.5$ MPa with (a) Equivalence ratio, ϕ, at $\xi_N = 0.79$, (b) Dilution ratio, ξ_N, at $\phi = 0.8$ and (c) Equivalence ratio, ϕ, at $\xi_N = 0.55$

Figure 5.7 shows direct photographs of the flame and images acquired via OH-PLIF. Figures 5.7(a) and 5.7(b) show natural luminosity and OH-PLIF single shot images that were acquired for a CH_4-air flame and Figs. 5.7(c) – (d) were acquired in an oxygen enriched condition. The distorted section on the upper right region of Fig. 5.7(c) appears due to the presence of an igniter. The increased laser attenuation observable on the left hand side of Fig.5.7(d) is caused by the enhanced absorption

of the laser energy as a result of the larger amount of OH present in the flame. The excitation wavelength employed in the OH-PLIF measurements is identical to that used for the LITGS measurements in this study (282.989 nm). The natural light figures (Fig. 5.7(a) and (c) show the blue C_2 chemiluminescence around the flame zone, followed by broadband white emission in the downstream region of the oxygen-enriched flames. The signal level in Fig. 5.7(c) is significantly higher than that in the air flames Fig. 5.7(a), owing to the much higher temperature in the former. The bottom of Fig. 5.7(b) shows the small conical flames associated with the individual holes of the burner, under the air-fired conditions. Similar conical flames were also formed in the oxygen enriched flame (5.7(d)). Based on the uniform signal in the measurement points marked in Figs. 5.7(a) and (b), we assume that the OH and temperatures in the burnt gas region are uniform across the horizontal region.

Fig. 5.7 Flame images: (a)Direct photograph at $P = 0.5$ MPa, $\xi_N = 0.79$ and $\phi = 0.8$; (b) OH-PLIF image at $P = 0.5$ MPa, $\xi_N = 0.79$ and $\phi = 0.8$; (c) Direct photograph at $P = 0.5$ MPa, $\xi_N = 0.55$ and $\phi = 0.8$; (d) OH-PLIF image at $P = 0.5$ MPa, $\xi_N = 0.55$ and $\phi = 0.8$.

5.4.2 Quantitative measurements of temperature from LITGS signal

Figure 5.8 shows representative single shots of LITGS signal for conditions where (a) $\xi_N = 0.79$ and $\phi = 0.75$, (b) $\xi_N = 0.55$ and $\phi = 0.8$ and (c) $\xi_N = 0.55$ and $\phi = 0.45$. Since the the total duration of a single shot of LITGS signal is shorter than 0.5 μs the technique has the potential for temporally resolved measurements in turbulent flames. The zero origin for each shot is shifted to the the point of maximum signal intensity.

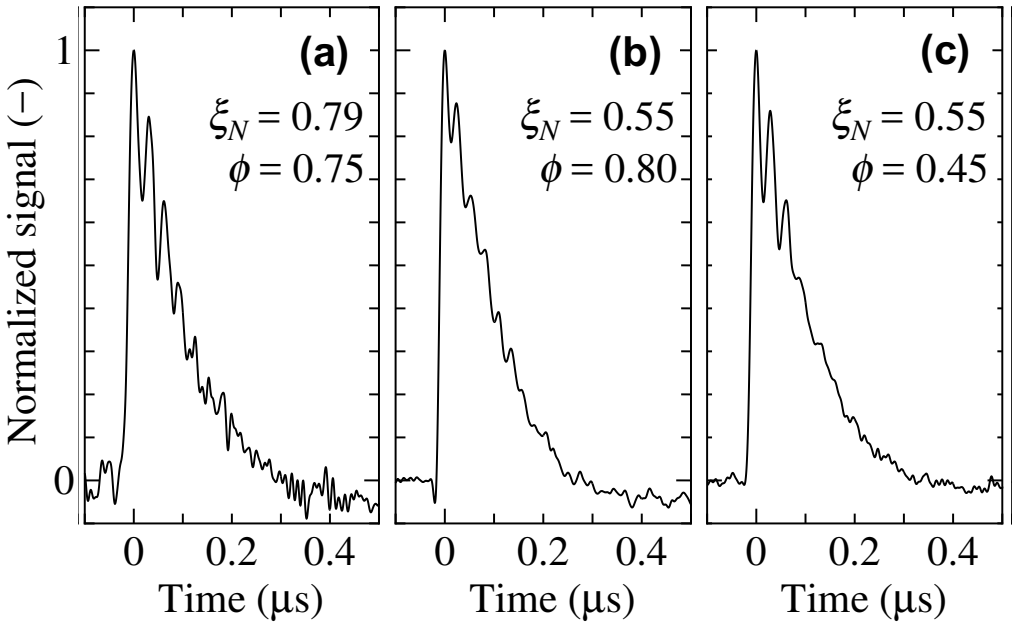

Fig. 5.8 Representative single shot OH-LITGS signals at three different conditions

Figures 5.9 and 5.10 show measured and calculated flame temperatures as a function of equivalence ratio, for $P = 0.5$ MPa at two dilution ratio conditions ($\xi = 0.79$ and 0.55, respectively). Figure 5.11 shows the measured and calculated flame temperatures as a function of the dilution ratio, ξ_N where the equivalence ratio, ϕ, is fixed at 0.8. The symbols represent the mean temperature extracted from the measured LITGS signal

frequency, and the error bars are the root mean square of the measured values, which were averaged over 40 shots. The solid lines represent the adiabatic flame temperatures calculated using one-dimensional free flame simulations at the corresponding operating conditions.

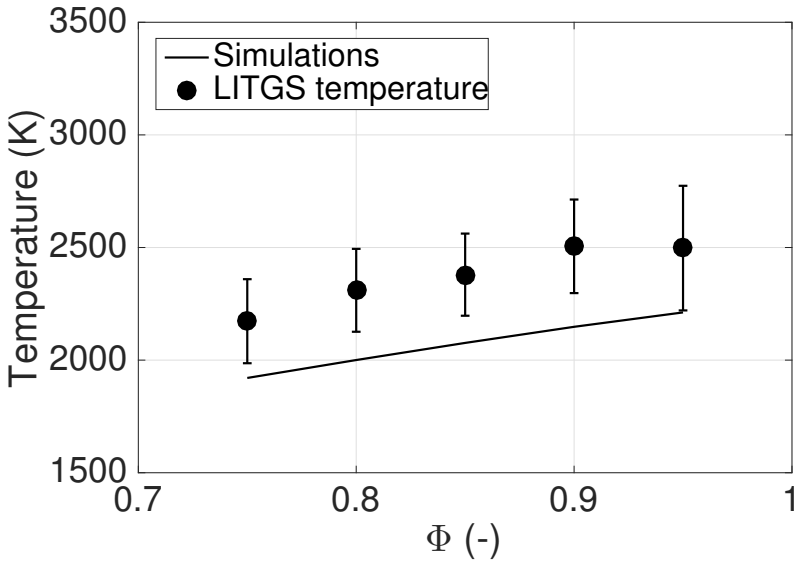

Fig. 5.9 Experimentally derived temperature from LITGS signal, T, at $P = 0.5$ MPa in CH_4-Air flame with equivalence ratio, ϕ, at $\xi_N = 0.79$. The closed symbols in the figure correspond the derived temperature from LITGS signal and the line corresponds the results of 1D flame simulation using CHEMKIN-PRO.

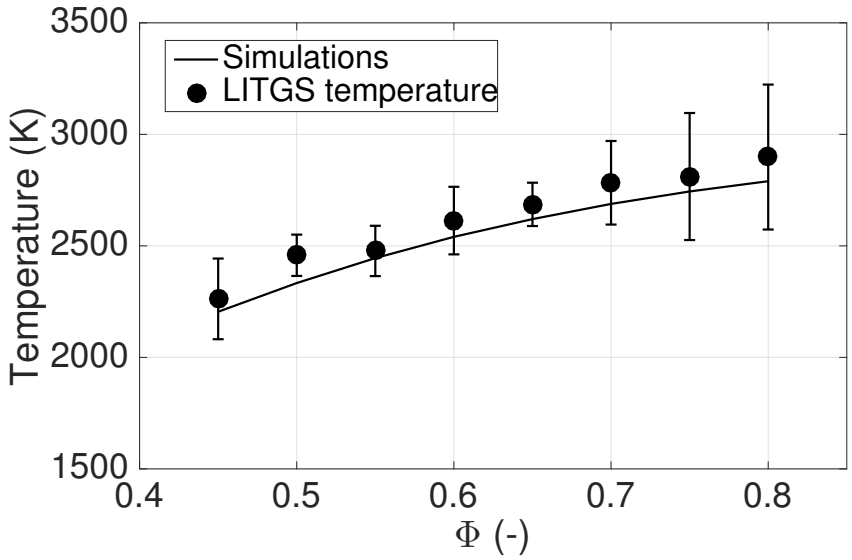

Fig. 5.10 Experimentally derived temperature from LITGS signal, T, at $P = 0.5$ MPa in oxygen enriched flame with equivalence ratio, ϕ, at $\xi_N = 0.55$.

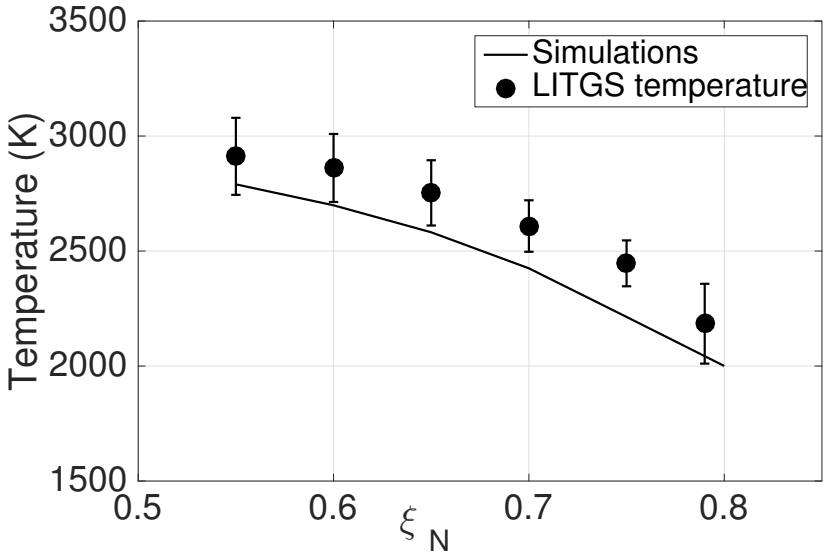

Fig. 5.11 Experimentally derived temperature from LITGS signal, T, at $P = 0.5$ MPa with dilution ratio, ξ_N, at $\phi = 0.8$

The values of the specific heat ratio, γ, and the mean molecular weight, W, used in Eq. 2.13 were obtained from the expected molar fractions of species and temperature obtained from one-dimensional flame simulations at 15 mm downstream of the burner exit for the oxygen enriched condition or 7 mm downstream for the CH_4/air condition. In all cases shown in Figs. 5.9, 5.10 and 5.11, the LITGS signal leads to overestimations of the temperature relative to the values obtained via simulations by about 200-250 K. This may seem a little surprising, since the actual temperatures are expected to be lower than adiabatic, on account of potential heat losses to the burner. As discussed in section 3.3 some of systematic error in the derived temperature may be attributed to error in the knowledge of the grating spacing, Λ. Note that because $T \propto c^2 W/\gamma \propto (\Lambda f)^2 W/\gamma$, small errors in the absolute value of Λ (say, 3%) can lead to 8% error in the evaluated temperature. In general, calibration of the grating spacing should be performed using the same absorbing species as is targeted in the final measurements, and without any further adjustment of the beams thereafter. In this case, once OH-LITGS signal was obtained, slight adjustments of the beams were performed to maximize the signal intensity as initial signals were extremely weak. The initially weak signal is likely due to beam steering effects within the flame that causes imperfect overlap of the beams.

The systematic overestimation of temperature observed in Fig.'s 5.9, 5.10 and 5.11 may also be attributed to the generation of a local disturbance to the local temperature and density required for LITGS measurements. As investigated in Chapter 4, the trade-off between producing robust LITGS signals using high pump energies and the magnitude of the induced temperature rise due to the thermalisation process must be considered when obtaining LITGS measurements. Future experiments may remove the influence of laser heating by first measuring the LITGS temperature over a range of energies (where sufficient signal can be obtained) as calibration for an estimate of the true gas temperature without the influence of thermalisation under a particular flame condition.

This technique has been applied in further research since this data was acquired to obtain measurements with improved accuracy [49].

Based on previous LITGS experiments performed in Chapter 4 [48] in non-reacting flows at ambient conditions, local heating effects due to the absorption of laser light can lead to an overestimation of the derived temperature from the LITGS. To enhance the accuracy of LITGS measurements, the pump energy should be sufficiently strong to produce signal, but remain weak enough to avoid significant heating of the bulk gas. The influence of the pump energy on OH-LITGS signal has not been studied in this work.

Further uncertainties in the thermodynamic properties can be evaluated by estimating the changes with temperature. An uncertainty of 300 K leads to an uncertainty in γ of the order of 1% and little change in molecular weight. Therefore, this cannot account for the systematic difference observed

Figure 5.12 shows the systematic deviation between the derived temperature from the LITGS signal and the temperature calculated from the one-dimensional flame simulations.

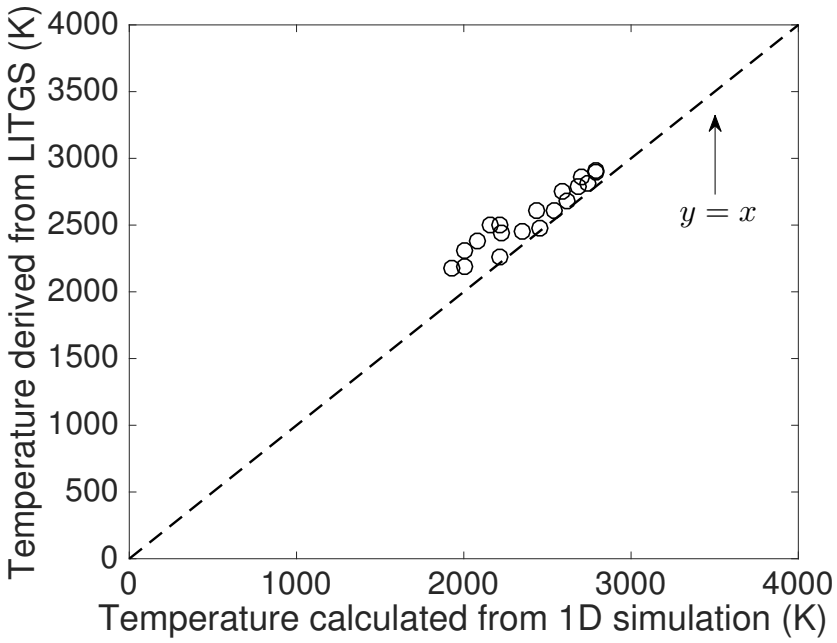

Fig. 5.12 Relationship between derived temperature and the temperature calculated from 1D flame simulation.

5.4.3 Analysis of LITGS signal contrast

The quality of LITGS signals with respect to the determination of the frequency increases as the peak signal and the contrast (or amplitude) between peaks and troughs both increase. Figure 5.8 shows the amplitude of oscillation of LITGS signal decreases with increasing temperatures.

The contrast is defined in Eq. (5.2) according to [146], as a measure of the relative strength of the stationary thermal and acoustic components that generate the oscillations.

$$\Delta I = \frac{1}{N} \sum_{i}^{N} \frac{I_{max,i} - I_{min,i}}{I_{max,i} + I_{min,i}}. \tag{5.2}$$

where $I_{max,i}$ and $I_{min,i}$ represent the intensities of the i-th local peak and trough, respectively. N is the total number of local peaks used for the calculation of signal contrast. The value of N is dependent on the number of local peaks detectable in each smoothed shot of LITGS signal.

Figure 5.13 shows the variation in signal contrast for conditions (a) $\xi_N = 0.79$, (b) $\phi = 1.0$ and (c) $\xi_N = 0.55$. At fixed dilution ratio conditions, shown in Figs. 5.13a and 5.13c, the signal contrast decreases with an increase in the equivalence ratio. In addition, Fig. 5.13b shows that the signal contrast increases as the dilution ratio increases. A higher equivalence ratio or dilution ratio leads to an increase in the flame temperature. Figures 5.14 and 5.15 show the variations of signal contrast with temperature derived from LITGS signal and burnt gas density at the measurement point, respectively.

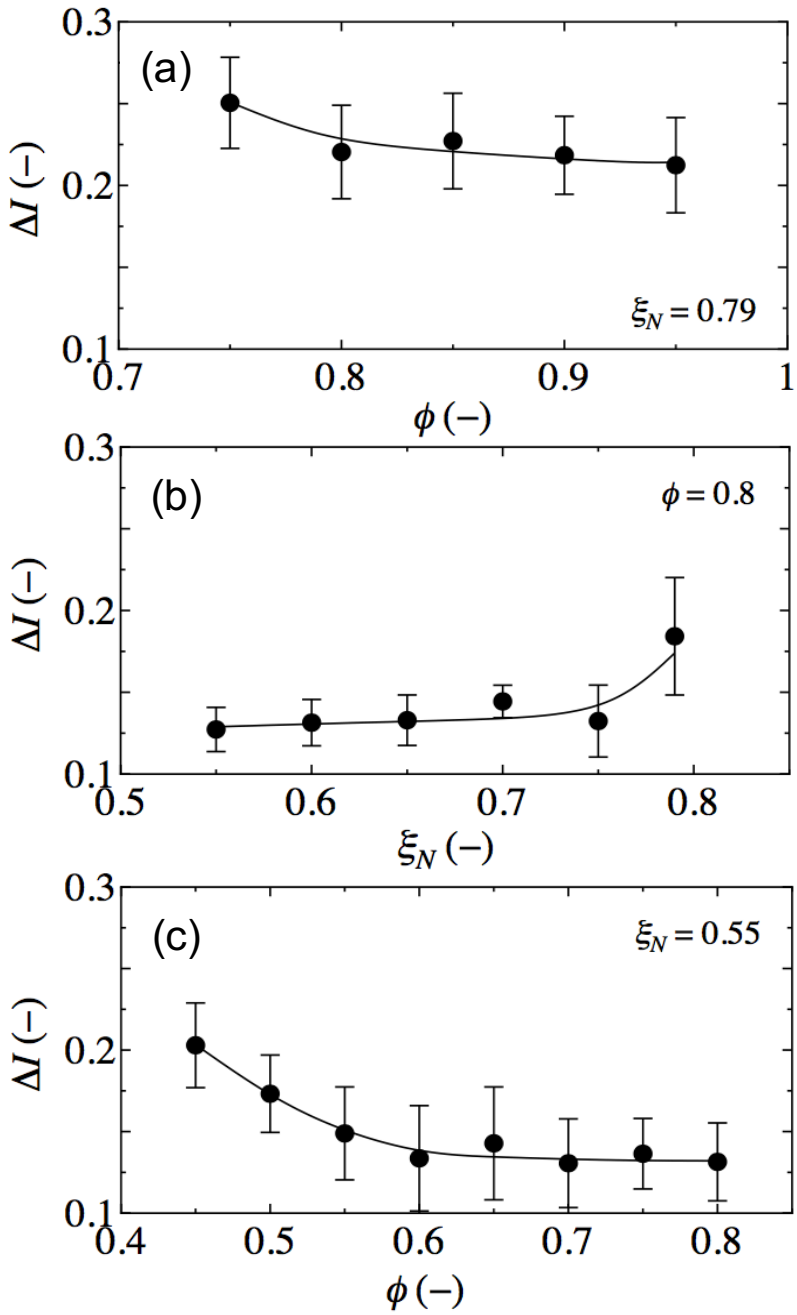

Fig. 5.13 Signal contrast, ΔI, at $P = 0.5$ MPa as a function of (a) Equivalence ratio, ϕ, at $\xi_N = 0.79$, (b) Dilution ratio, ξ_N, at $\phi = 0.8$ and (c) Equivalence ratio, ϕ, at $\xi_N = 0.55$.

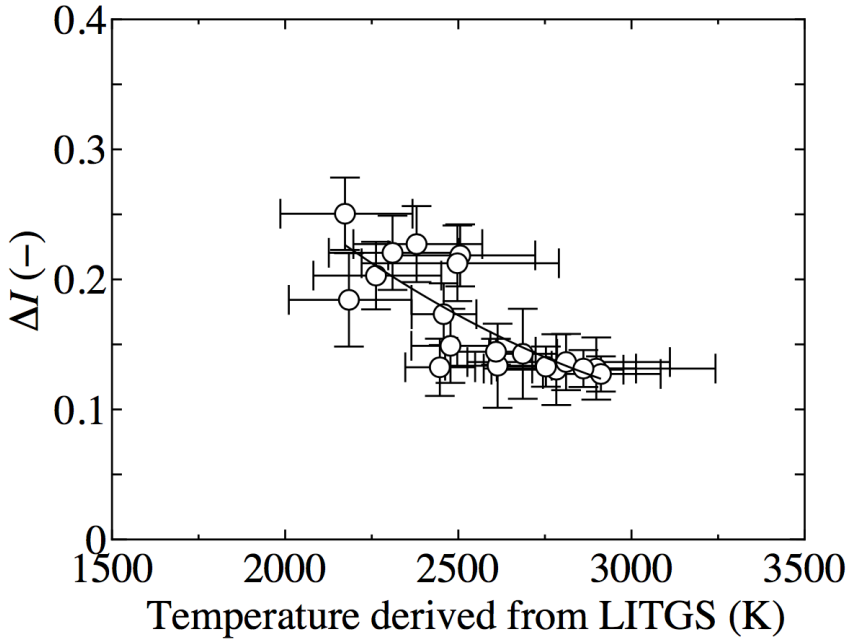

Fig. 5.14 . Relationship between signal contrast, ΔI, and the temperature evaluated from LITGS signal.

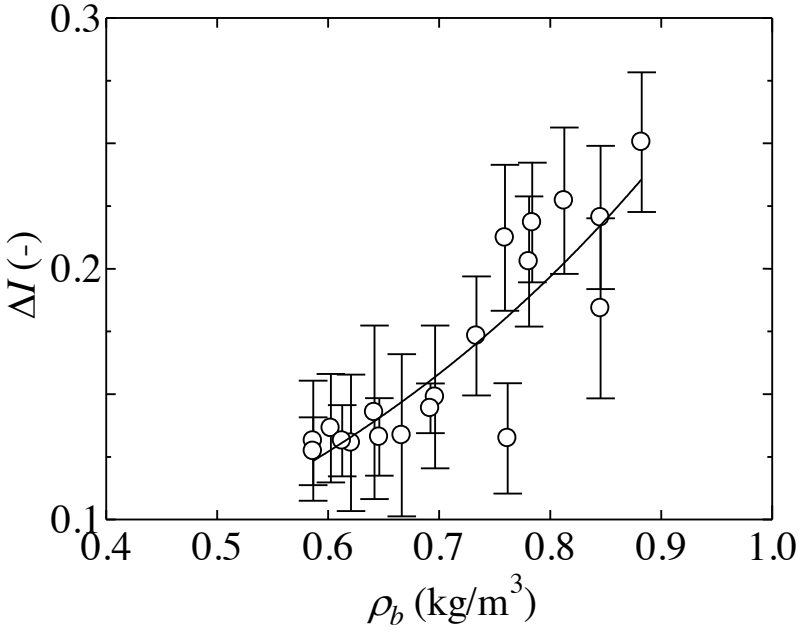

Fig. 5.15 . Relationship between signal contrast, ΔI, and mixture density at the measurement point, ρ_b.

In general, as the temperature increases, the overall mass density of OH decreases, and both the signal and the signal contrast decrease. Hence, under high temperature conditions, where the relative strength of the propagating acoustic wave is weak, obtaining LITGS signal becomes increasingly difficult. In addition, as the burnt gas density increases, the signal contrast increases.

5.5 Summary

To explore the potential for quantitative measurements of temperature in high temperature, high pressure, rocket motor combustion, Laser Induced Thermal Grating Spectroscopy (LITGS) using OH as the target absorbing species was applied to flame temperature measurements in CH_4/air flames and oxygen enriched $CH_4/O_2/N_2$ mixtures at 0.5 MPa. The main conclusions are as follows:

1. LITGS signal can be acquired successfully in CH_4/air and oxygen-enriched $CH_4/O_2/N_2$ flames operating at pressures of 0.5 MPa. The burned gas temperature can be derived from the LITGS signal for the mixtures where the flame temperature is as high as 2900 K. Therefore, the potential for LITGS measurement in high temperature flames is demonstrated.

2. The derived burned gas temperature obtained from the LITGS signal is close to estimations made using one-dimensional flame simulation. Temperatures are overestimated by around 200 - 250 K at the conditions measured.

3. As the flame temperature increases, the signal contrast, which represents the quality of LITGS signal with respect to the ease at which the oscillation frequency

can be extracted, decreases. The decrease in signal contrast is the result of a decrease in the burnt gas density at the measurement point.

Chapter 6

LITGS thermometry using NO absorption

6.1 Introduction

In Chapter 5, LITGS measurements were demonstrated in high pressure flames where OH was selected as the target species for molecular excitation. This chapter demonstrates quantitative measurements of temperature in high pressure flames using LITGS where NO is the target absorbing species. Targeting NO can lead to a number of distinct advantages over OH. First, NO-LITGS has the potential to provide measurements in high pressure combustion environments where NO exists in larger quantities than OH, such as ammonia combustion (discussed further in section 6.4). Second, unlike OH, small amounts of NO can be doped into the unburnt mixture, creating the potential for spatially resolved measurements of temperature through the flame which would act as a marker for the flame structure. NO doping has been employed for similar purposes in NO-LIF measurements [130]. Finally, with suitable calibration and a stable signal,

NO-LITGS could offer the potential for simultaneous measurements of temperature and NO concentration by extracting the temperature from the frequency of oscillations and the concentration from the signal intensity.

In this Chapter, we explore the potential for quantitative measurements of temperature using NO-LITGS under high pressure conditions in both reacting and non-reacting environments. The NO-LITGS signal is demonstrated in the burned gas of premixed CH_4/NH_3/air flames under high pressure conditions.

6.2 Absorber selection - Nitric Oxide (NO)

Oxides of nitrogen (NO_x) are some of the most important pollutants associated with combustion due to their role in the production of acid rain and smog, as well as their influence on the depletion of atmospheric ozone [16]. With strict regulations placing stringent limits on acceptable levels of nitric oxide (NO) emitted from power-plants and engines [19, 31], there has been a concerted effort from the combustion community to advance our understanding of the formation of NO and develop tools for its detection and reduction, with particular attention paid to its strong dependence on temperature [67] [57]. Typical fluctuations in temperature found in gas turbine engine combustion chambers can lead to increases in NO production by an order of magnitude [59].

Unlike diatomic nitrogen (N_2), nitrogen as a single atom (N) has the potential to be reactive and form several oxides (e.g. NO, N_2O, N_2O_2), grouped as NO_x emissions. Nitric oxide (NO) formation is categorized by three mechanisms - *prompt NO*, *thermal NO* and *fuel NO*, with the most dominant source being *thermal NO* in most high pressure, high temperature combustion scenarios [41]. Thermal NO refers to the formation of NO by high temperature oxidation of atmospheric nitrogen. The sensitivity

of thermal NO formation to temperature has been the driving force behind low-NO_x, lean premixed gas turbine combustion research [112].

Fuel NO is formed via direct oxidation of nitrogen compounds found within the fuel, and is therefore primarily a concern in the combustion of fuels such as coal or ammonia [94]. Prompt NO is produced at the flame front, where molecular nitrogen in the air combines with fuel under fuel rich conditions. The flames explored in this chapter are laminar, premixed CH_4-NH_3-air mixtures operating at elevated pressure, which produce very thin reaction zones. Hence, the primary sources of NO can be attributed to fuel-NO and thermal-NO mechanisms.

Like OH, NO is also a product of combustion that exhibits absorption bands accessible in the UV and infra-red range [121, 127]. This has prompted the development of diagnostics techniques that utilize NO detection for temperature measurements in combustion environments, including NO-LIF [9] and two-color absorption spectroscopy [2]. In this chapter, NO-LITGS is employed using resonant molecular excitation in the NO A←X (0-0) band (approx. 226 nm). Figure 6.1 shows the UV absorption spectrum for NO at atmospheric conditions.

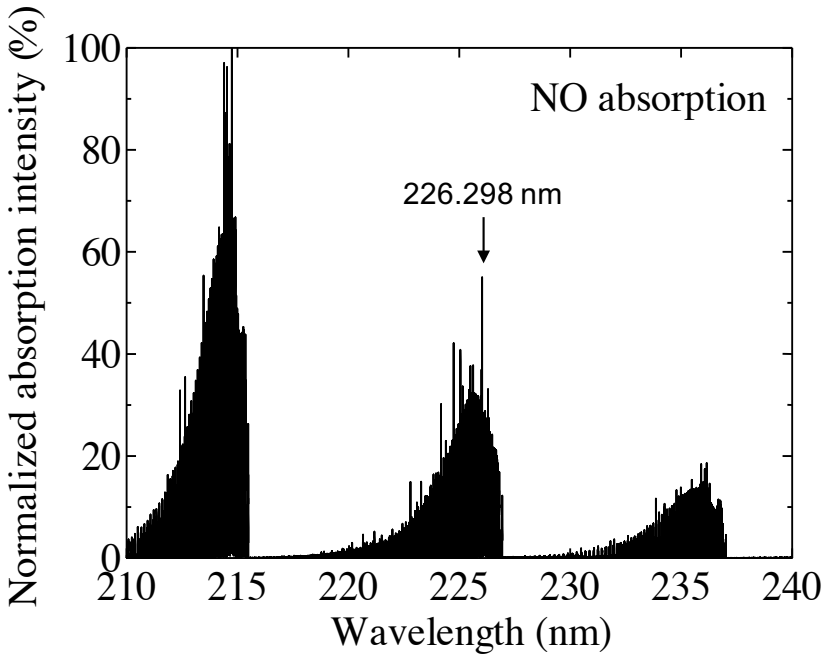

Fig. 6.1 UV absorption spectrum NO [108]

6.3 NO as a target species in high pressure combustion

Nitric oxide has been employed as a target species for a number of laser-based thermometry techniques including LIF and DFWM [35]. Most applications have been limited to non-reacting scenarios and flames operating at atmospheric pressure due to the challenges associated with measurements in high pressure, high temperature flows identified in Chapter 5. Electronic-resonance-enhanced (ERE) CARS using NO has also been suggested as a potential tool for thermometry since being employed for NO concentration measurements in NO-doped H_2/air flames [77]. Experiments performed in a jet at room temperature containing 1000 ppm of NO in various buffer gases (including N_2, O_2 and CO_2) showed little sensitivity between the NO-ERE-CARS

signal and the quench rates associated with each buffer gas [98]. However, Kulatilaka et al. [78] investigated the effect of pressure on NO-ERE-CARS signal in a gas cell containing mixtures of NO and N_2 and found that the CARS signal saturated at pressures above 2 bar. Laser-Induced Fluorescence (LIF) excitation in the NO A<–X (0-0) band (approx. 226 nm) has become a more established method for the detection of NO in high pressure combustion environments [6] [106]. The first example of the use of NO-LIF for thermometry in high pressure combustion was performed by Vyrodov et al. [140], where fuel-rich methane-air flames were doped with 400 ppm of NO up to 20 bar and they report temperature measurements with around 3% accuracy. Lean flames were avoided due to interference of O_2 fluorescence in the NO-LIF signal and the signal is reported to have suffered with an increase in pressure. Recently, Besseler et al. [9] demonstrated multi-line NO-LIF measurements of temperature in fuel-rich atmospheric flames before Lee et al. [84] extended this technique to slightly lean flames at high pressure (up to 60 bar). The multi-line NO-LIF method relies on accurate modeling of the excitation spectra, which requires adjustment for high pressure experiments. As with previous studies using NO-LIF, the SN ratio suffers with increased pressure and where the composition of the measurement region contains oxygen (i.e. lean flames) due to its influence on the quenching properties of the gas mixture.

LITGS measurements that employ molecular excitation of NO in flames may offer a number of potential advantages over LIF, DFWM and CARS. As was the case with OH-LITGS, signal is expected to improve with pressure, it does not require the target species to fluoresce and the coherent signal beam can be spectrally isolated with relative ease to avoid any signal contamination. Also, the NO-LITGS signal is expected to improve with O_2 in the gas mixture as it is shown to be good quenching partner of NO [95]. As such, LITGS may be a more appropriate tool for measuring temperature in lean flames.

Whilst NO has been recognized as a potential target species for LITGS measurements, it has not yet been employed for temperature measurements in flames. Danehy et al. [22] first observed thermal grating contributions as an artifact in DFWM experiments with NO excitation in gas cell conditions where collisions were increasingly prevalent (*i.e.* high pressure, or a strongly collisional quenching partner buffer gas such as CO_2). They also performed measurements in an NO doped (400 ppm doping) atmospheric, oxygen-enriched $CH_4/N_2/O_2$ flame but reported the dominance of population gratings (i.e. DFWM signals) and did not detect any LITGS signal. McCormack *et al.* [92, 93] have used NO-LITGS to successfully obtain the absorption spectrum and make inferences regarding the molecular physics of NO.

6.4 Ammonia-methane combustion

Additional regulatory requirements to decarbonise the power and transport sector have led to research efforts into alternative fuels that, when burned, generate ultra-low CO_2 emissions. Hydrogen has been identified as an alternative carbon-free fuel source [135]. However, economic, technical and safety concerns associated with its storage and distribution have acted as barriers to its complete adoption in the transportation and power generation sectors [107].

Ammonia has been suggested as a potential carbon-free alternative to hydrogen for several reasons. It is relatively cheap and is easier to handle, store and distribute safely due to its narrow flammability limits [11]. Ammonia can be produced from renewable energy sources, including wind and solar energy [43, 142] and CO_2 sequestration can be performed in facilities that produce ammonia [155]. The use of ammonia as a fuel in gas turbine engines was first proposed in the 1960's [89, 100, 136]. However, directly

replacing conventional fossil fuels with pure ammonia-air combustion is challenging, particularly due to the relatively slow chemical reaction rates associated with burning ammonia [85]. Low laminar flame speeds require reduced air flows to maintain flame stability, which in turn leads to reduced turbulent mixing and hence poor combustion efficiency. Also, whilst a carbon-free fuel source like ammonia is an attractive option for reducing CO_2 emissions, it does produce large quantities of NO_x due to nitrogen molecules in the fuel reacting with oxygen (*i.e.* fuel-NO_x) [91, 101].

Given these challenges, fuel-blends of hydrogen or methane with ammonia have been proposed as a form of fuel enhancement to optimize flame stability and emissions performance [60]. Methane/ammonia combustion has recently been demonstrated using stratified injection with low tangential swirl to produce stable flames over a range of conditions [135].

This chapter demonstrates the potential for NO-LITGS measurements applied to premixed methane-ammonia combustion for quantitative measurements of temperature, where NO concentrations are predicted high enough to produce good signal.

6.5 Measurements in non-reacting environments

Before attempting measurements in a flame, preliminary tests were performed in a pressurized cell (which contained mixtures of NO/N_2) and heated laminar ambient air jet (with small amounts of NO added to the stream) to determine rough estimates of the minimum absorber concentration/pressure required to obtain NO-LITGS signal for a given temperature. The pressure in the cell was varied from 0.1 – 0.8 MPa and the temperature of the air-jet ranged from ambient to around 600 K.

6.5.1 Optical geometry

The optical layout of the experiment is shown in Fig 6.2. Pump pulses of 8 ns duration at a frequency of 10 Hz from a frequency doubled Nd:YAG laser (Continuum Surelite I-10) pumping a Sirah dye laser (using Coumarin 6 dye) at 226 nm delivered energies of up to 1.5 mJ over a diameter of 3.89 mm to a 50/50 beam splitter. The pump beams, separated by a distance of 10 mm were focused towards the probe volume using a single 750 mm focal length crossing lens for a crossing angle of 0.802°.

The continuous wave probe beam ($\lambda_2 = 671$ nm, diameter around 1 mm) producing powers of up to 1 W was provided by a diode-pumped solid state laser (CNI, MLL-III-300) at an angle of 0.877° to the midplane of the crossed beams. The diffracted signal was collected at the corresponding Bragg angle via mirrors into a photomultiplier tube (Hamamatsu PMT), with a gain of 0.75 V for a sensitivity of 80 mA/W after spectral filtering with a narrow bandwidth filter around the probe wavelength. The signal, triggered from the rise in the collected LITGS signal itself with a threshold of 150 mV was collected using a PC oscilloscope (PicoScope 6000) at a maximum sampling rate of 5 GS/s and 8-bit precision.

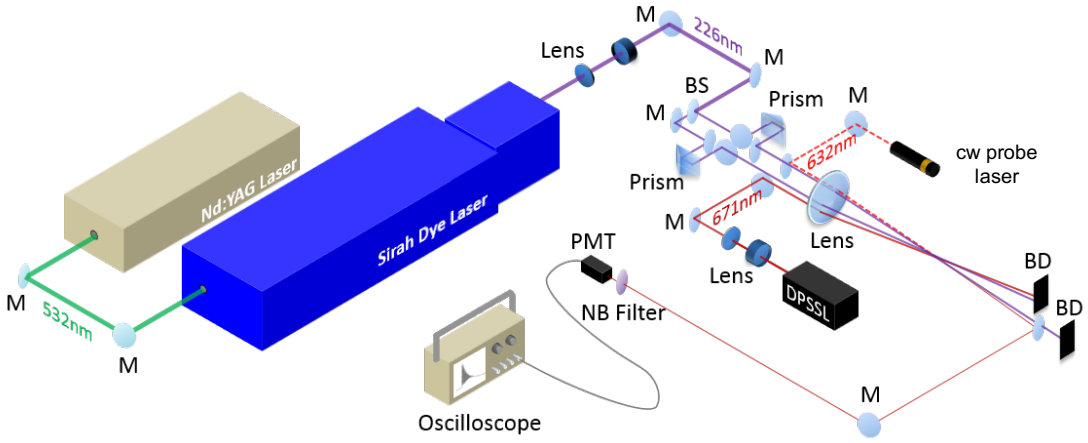

Fig. 6.2 Schematic diagram of the experimental setup for NO-LITGS measurements in a high pressure cell and heated jet. M: mirror, BS: beam-splitter, PMT: Photo-multiplier tube, BD: Beam-dump

6.5.2 Pressure cell design

A sketch of the in-house designed high-pressure cell is shown in Fig.6.3. Two observation windows ($\phi = 100$ mm) were embedded in stainless steel flanges. A graphite gasket with a nickel impregnated foil was used for sealing, which is appropriate for NO. The optical access window was made of quartz glass (Spectrosil 2000, damage threshold of 3854 ± 85 J/cm^2) with thickness of 10 mm. A vacuum pump was connected to the cell to evacuate any gas in the chamber prior to filling it with mixtures of NO/N_2. Experiments were conducted at room temperature by first filling an evacuated static pressure cell with a known amount of NO in a range of 518 ppm to 4149 ppm, which resonantly absorbs 226 nm UV light output from the dye laser. Fixed amounts of dry N_2 were then successively added to the cell. The composition in the cell was controlled by individual stainless steel low flow metering valves (Swagelok, SS–SS4–VH) and determined by pressure measurements read from a pressure sensor (Keyence, GP–M010) with 0.3% accuracy. In this way, once the gas pressure was set to the

maximum condition of interest (*i.e.* 0.8 MPa), data were collected as a function of the total pressure with fractional amounts of the mixture bled off between conditions. The temperature inside the cell was acquired using a calibrated K-type thermocouple inserted in the cell wall.

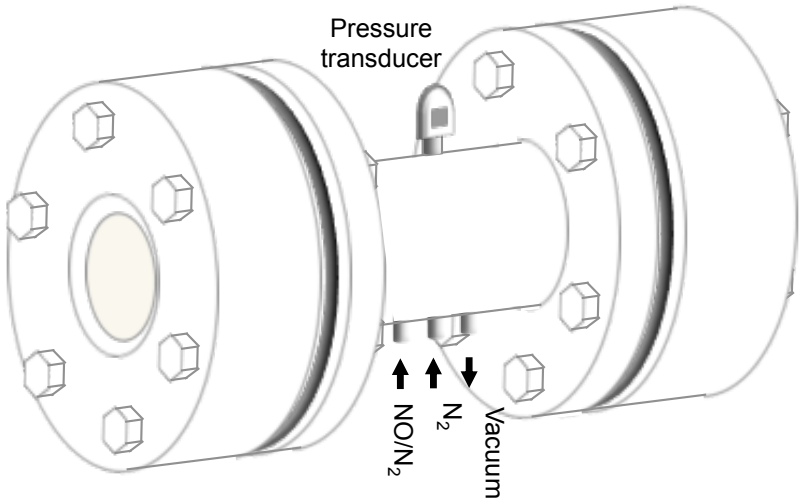

Fig. 6.3 Structure of optically accessible high pressure cell

6.5.3 Heated jet layout

In order to investigate the NO-LITGS signal dependence on both temperature and absorber concentration, a preheated free jet of 6.35 mm inner diameter was used. The flow rate of NO/N_2 was controlled by a calibrated rotameter and the amount of diluent (N_2) was controlled using a mass flow controller (Alicat MCR–250SLPM). The mole fractions of NO in the jet were set to 3630, 5910, 8500, 11500, and 15000 ppm. The jet was heated using an in-line heating cartridge (Omega Engineering, AHP–7562), providing a maximum outlet temperature of around 600 K for the flow rate of air at 42.4 SLPM. The temperature at the jet nozzle was measured using a calibrated K-type

thermocouple and digital thermometer (RS 206-3744) with a probe diameter of 1.5 mm and measurement accuracy of ± 1.5 °C. Measurements were taken at five temperature conditions (292, 306, 388, 483, and 577 K).

6.5.4 Results

Pressure cell

Single shot NO-LITGS signals were acquired at pressures ranging from 0.1 MPa to 0.8 MPa in mixtures of NO/N_2, where the mole fractions of NO ranged from 500 – 4300 ppm. LITGS signal was detectable using mole fractions of NO as low as 1800 ppm at 0.1 MPa and ambient temperatures, corresponding to a concentration of 0.07 moles/m^3. When the total pressure in the cell was increased to 0.5 MPa (the operating pressure for flame experiments as described in section 6.6), LITGS signal could be observed with mole fractions of NO down to 500 ppm.

Figure 6.4 shows averaged shots of LITGS signal for three pressure conditions. In all three cases, the mole fraction of NO is 1800 ppm.

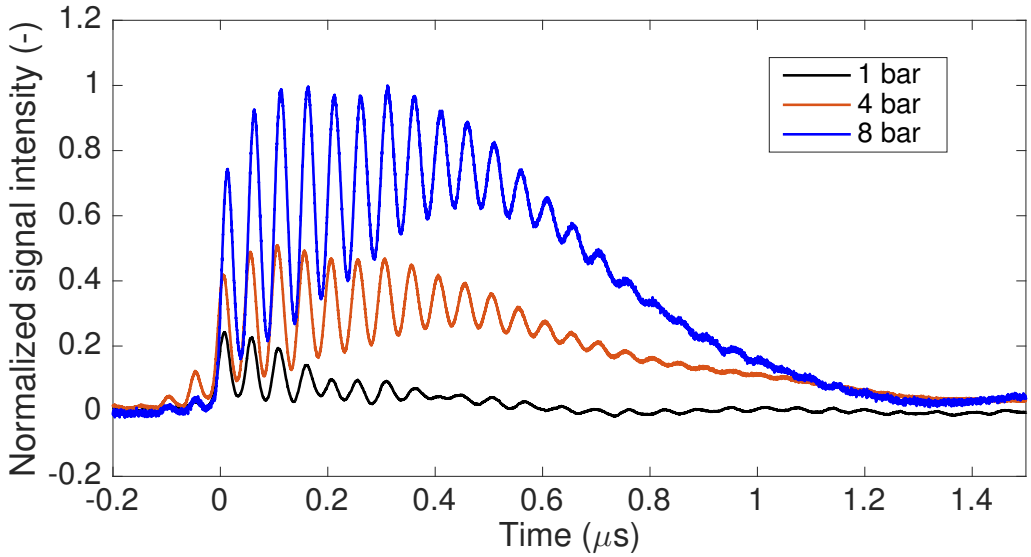

Fig. 6.4 Averaged NO-LITGS signal (over 400 shots) at three pressure conditions. All measurements were acquired gaseous mixtures of NO/N_2 with mole fractions of 1800 ppm.

The traces show that an increase in pressure has notable effects on the LITGS signal. First, the signal intensity increases with pressure due to the higher rate of collisions and subsequently stronger density perturbations that define the thermal grating. Second, the time taken for the LITGS signal to decay increases slightly with pressure. The rate of decay is dependent on the thermal diffusivity of the gas, which is inversely proportional to the mixture density. Hence, the rate at which the thermal perturbation due to the induced grating equilibrates with the surrounding gas decreases with pressure, leading to longer-lived signals.

Finally, we observe a change in the shape of the LITGS signal with an increase in pressure. As the pressure (and signal intensity) increases, a 'hump' begins to form in the signal. At 1 bar, the troughs in the oscillations fall close to the zero value of intensity at almost all points in the trace. At 8 bar, the signal intensity at the troughs

in the oscillations increases while the peaks remain at relatively constant intensities until around 0.5 μs before both peaks and trough values of intensity decrease until the signal dies out. As discussed in chapter 5, the relative intensities of the peaks and troughs define the signal contrast.

Given that the contrast is a measure of the strength of the thermal to the acoustic perturbation, this suggests that the rate at which the acoustic wave is damped is faster than the rate at which the thermal grating diffuses for signals acquired at higher pressure. At 1 bar, the contrast between each peak and trough is close to 1 for the whole trace, indicating that acoustic damping and thermal diffusion occur at similar rates. The shape of the LITGS signal also depends on the absorber selection and quenching partners (or the surrounding molecules, which is N_2 in this case) as it depends on the quenching and relaxation processes, which differ for different molecules.

Figure 6.5 shows the measured LITGS temperature with the mole fraction of NO in the mixture for various pressures. For the range of absorber mole fractions and pressures, the temperature remains almost constant, suggesting that localized laser heating effects are not dominant for the range of concentrations used in this study.

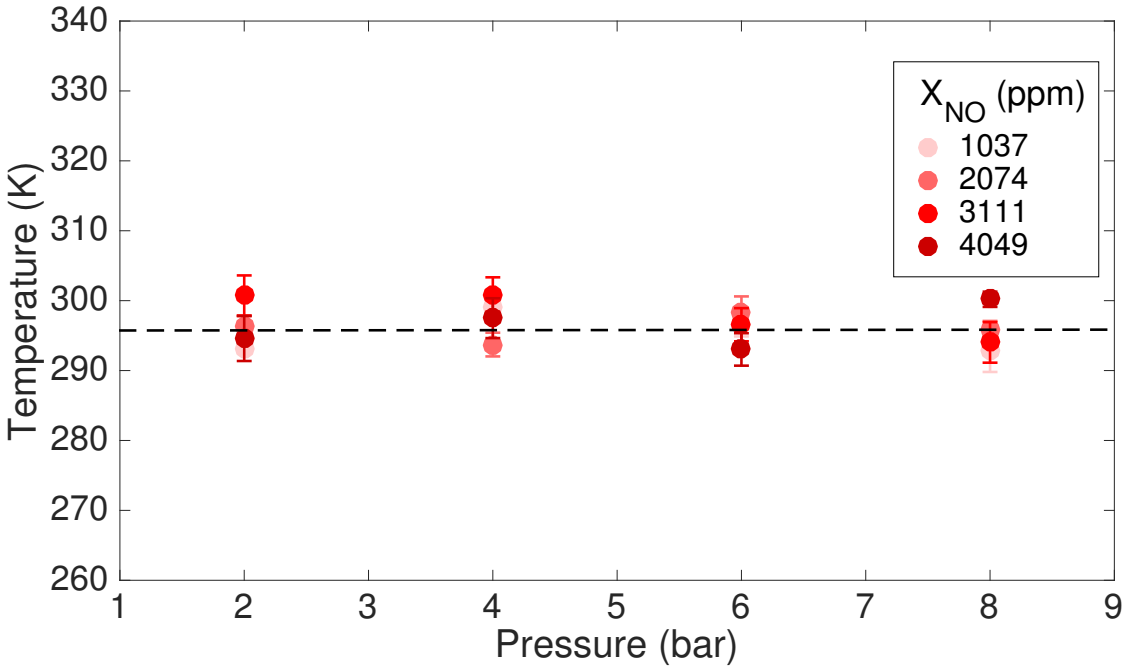

Fig. 6.5 LITGS temperature vs pressure for various quantities of NO in NO/N_2 mixture. Dashed line represents the stable thermocouple measurement in the pressure cell.

Heated jet

In the heated air jet, single shot NO-LITGS signals were recorded at five temperatures, ranging from 292 – 577.8 K for absorber mole fractions up to 15,000 ppm. Figure 6.6 shows averaged shots of LITGS signal for three different jet temperatures. In all three cases, the absorber mole fraction is set to 5900 ppm.

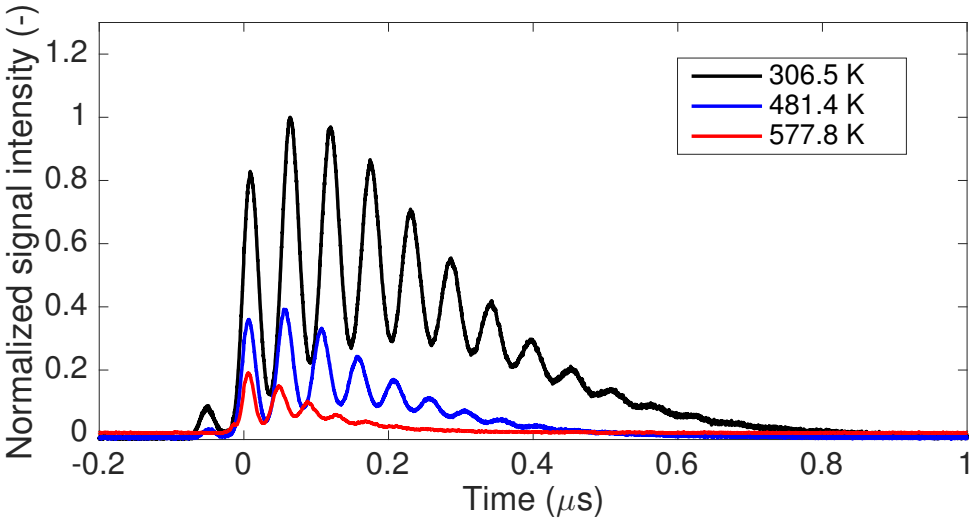

Fig. 6.6 Averaged NO-LITGS signal (over 400 shots) at three jet temperature conditions. All measurements were acquired gaseous mixtures of NO/N_2 with mole fractions of 5900 ppm.

As the temperature of the jet is increased, the amplitude of the LITGS signal decreases, due to the lower density mixture and subsequent reduction in collisions. Also, the signal decay rate increases with an increase in temperature because diffusion rate is proportional to $T^{1.5}$, resulting in rapid equilibration of the thermal grating at elevated temperatures. In flames where temperatures are significantly higher, larger probe volumes should be employed to compensate for the reduction in signal length in order to ensure that a sufficient number of oscillations are acquired to recover the temperature with sufficient precision [68].

Figure 6.7 shows the temperature derived from LITGS for various jet temperatures and absorber mole fractions. A slight increase in temperature can be observed at high absorber mole fractions, however for the range of mole fractions expected in flame

measurements presented later in this chapter (≈ 6000 ppm, discussed in section 6.6.3), points remain in close agreement with thermocouple temperatures.

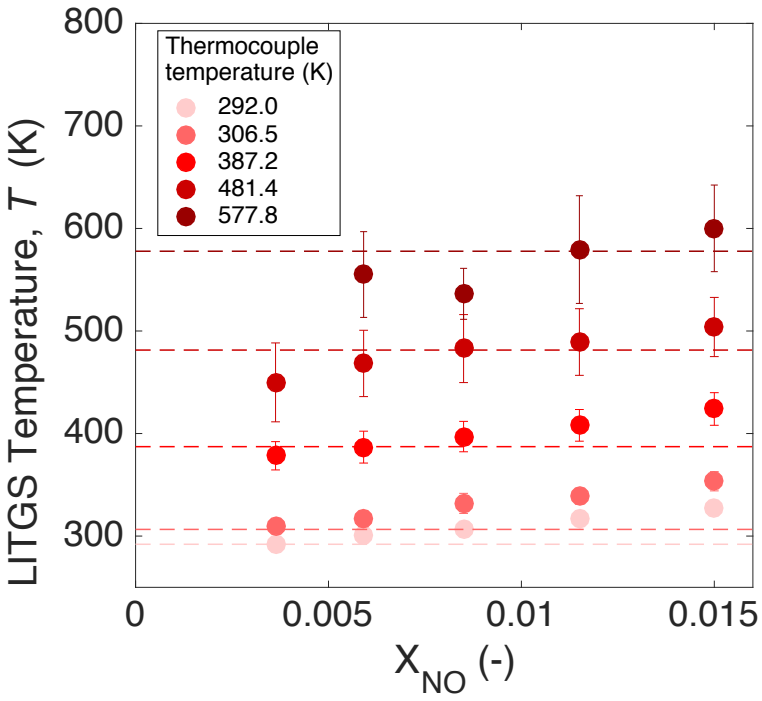

Fig. 6.7 Temperature vs mole fraction of NO for various jet temperatures.

6.6 CH_4/NH_3/air flames at high pressure

Preliminary measurements in the pressure cell indicate that at ambient temperatures, around 500 PPM of NO was required to obtain sufficient signal the for optical geometry described in section 6.5.2 at 0.5 MPa. Given that the molar densities in burned gas mixtures can be expected to be around 5 – 6 times lower than the mixtures used under non-reacting conditions at a given pressure, we estimate that with a similar configuration, molar fractions of least 2500 ppm of NO would be required in the burned gas mixture to obtain signal.

This section gives an account of NO-LITGS measurements applied to high pressure, premixed, laminar methane-ammonia-air flames, where 1D simulations (as described in section 6.6.3) indicate mole fractions of NO of around 6800 ppm in he burned gas region. As was the case in Chapter 5, high pressure combustion experiments were carried out using the high pressure combustion test facility at the Institute of Fluid Science, Tohoku University.

6.6.1 Optical geometry

Figure 6.8 shows the schematic layout of the optical geometry through the high pressure chamber for 226 nm excitation. An Nd:YAG laser (Spectra-physics, GCR-250, 355 nm, 300 mJ) pumping a frequency doubled dye laser (Sirah, PrecisionScan) was employed to obtain a pump beam set to a wavelength of 226.2999 nm for NO excitation. The maximum available pump energy was around 10 mJ. The pump beam was split using a 50:50 beam splitter to separate two pulses before the beams are introduced into a 1000 mm focal length crossing lens at an incident angle, $\theta_p/2$.

A CW semiconductor laser, operating at a wavelength of 445 nm (Omicron, BrixX 445-250) was employed as the probe beam. The power for the probe beam was set to 2000 mW. The beams that pass through the high pressure chamber were stopped by a beam dump. The diffracted LITGS signal was detected using a photo multiplier tube (PMT, Hamamatsu Photonics, R928). The LITGS signal was acquired using an oscilloscope with a sampling rate of 20 GS/s and 500 MHz bandwidth (GwInstek, GDS-3154). 160 single shots of LITGS signal were acquired for all examined conditions.

The pump beam diameter at the crossing lens was measured in order to accurately evaluate volume of the crossing point and was found to be slightly elliptical in shape. The length of major and minor axes were 4.81 mm and 3.82 mm, respectively, assuming that the intensity of laser beam has a Gaussian profile. In this study, the distance between the two pump laser beams was set to 15 mm and thus the incident angle, $\theta_p/2$ was 5.0 mrad.

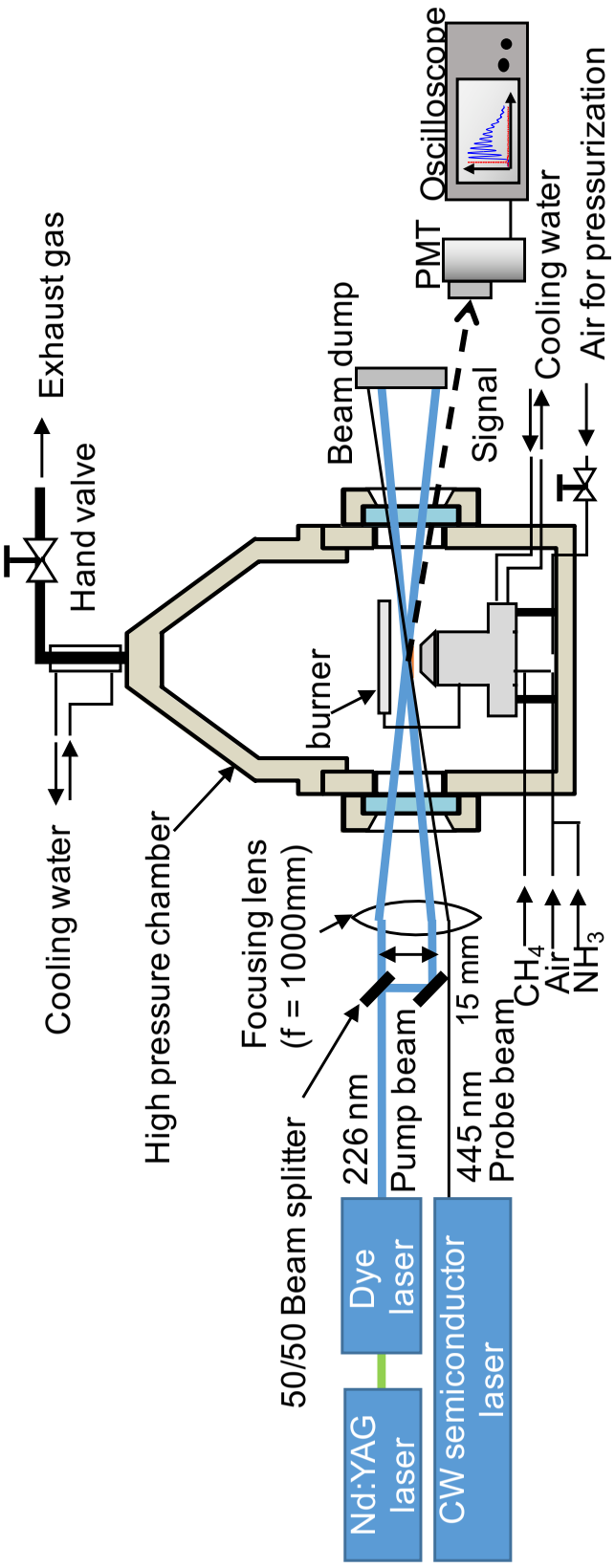

Fig. 6.8 Schematic diagram of the experimental setup for NO-LITGS measurements at high pressure.

6.6.2 Burner

Figure 6.9 shows a schematic diagram of the high pressure burner used to generate a flat flame. The burner is composed of a stainless steel nozzle and a water-cooled stainless steel plate which is used for flow stagnation. The burner stabilized stagnation flame is generated between the burner and the stagnation plate and a direct photograph of the flame is shown in figure 6.9. The premixed reactants (CH_4, NH_3 and air) are introduced into the base of the burner before exiting through the 20 mm diameter nozzle. The burner is placed on a z-axis stage at the center of the pressure chamber (described in section 5.3.3). The maximum total flow rate of the mixture was 77.8 standard litres per minute (SLM).

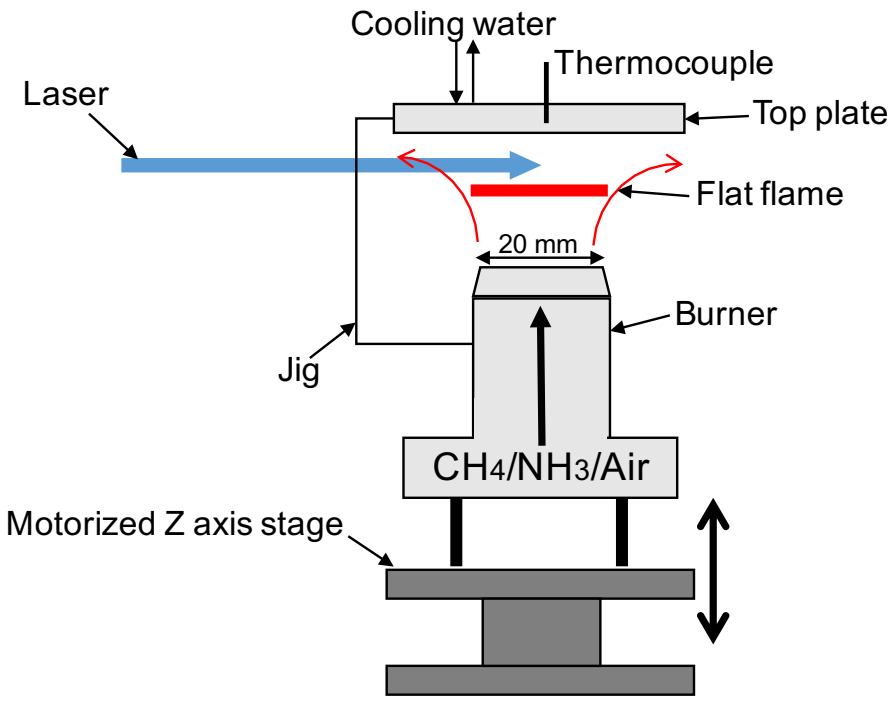

Fig. 6.9 Schematic diagram of stagnation-plate stabilized burner set-up.

Figure 6.10 shows a direct photograph of a CH_4-NH_3-air flame at $\Phi = 0.9$ with 10% NO in the reactant mixture. The top plate is placed 20 mm above the burner outlet.

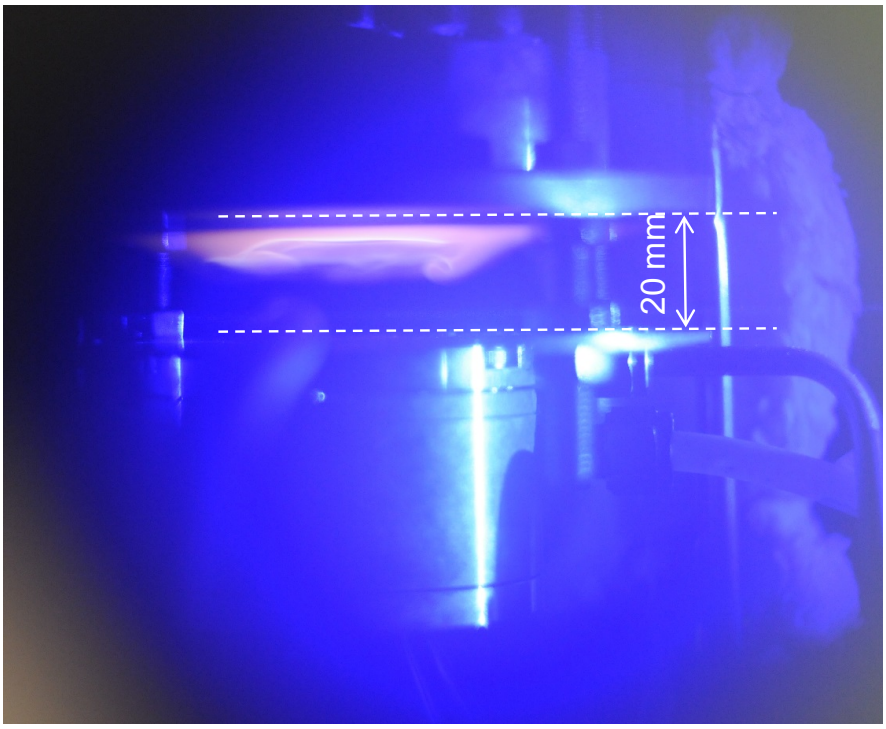

Fig. 6.10 Direct photograph of CH_4/NH_3/air flame. Equivalence ratio, $\Phi = 0.9$, 10% NH_3 in the fuel mixture.

6.6.3 Results

NO-LITGS signals were systematically acquired at various heights above the burner in the burned gas region of a premixed, CH_4-NH_3-air flame at $\Phi = 0.9$. The NH_3 mixing ratio was set to 0.1 (*i.e.* 10% NH_3 in the fuel mixture) and is defined as the weighted energy fraction:

$$E = \frac{[NH_3][LHV_{NH_3}]}{[NH_3][LHV_{NH_3}] + [CH_4][LHV_{CH_4}]} \tag{6.1}$$

where $[i]$ is the volumetric flow rate of species, i and $[LHV_i]$ is the lower heating value of species i per unit volume [87].

Additional measurements where the NH_3 mixing ratio was set to 0.2 were acquired at one fixed position of 19 mm above the burner exit.

Flame structure

Figure 6.11 shows the simulated flame structure of a methane-ammonia-air flame, for a pressure $P = 0.5$ MPa and equivalence ratio $\phi = 0.9$. 1D strain stabilized numerical simulations were performed using CHEMKIN-PRO [104] with GRI-Mech 3.0 reaction mechanism [119] to determine species and temperatures. The GRI-Mech 3.0 mechanism was selected based on a comparative study by Okafor et al. [97] on how various reaction mechanisms performed in predicting laminar burning velocities in CH_4-NH_3-air combustion under conditions presented in this work. The fuel mixture contains 10% ammonia. The origin is set to the outlet of the burner nozzle and the top plate temperature is used as the downstream boundary condition. The top-plate wall temperature was estimated by simultaneously acquiring the temperature at three

locations within the top plate and subsequently applying a linear approximation to estimate the temperature through the plate. The initial temperature of the mixture was 298 K. The flame thickness is of the order of a hundred micrometres, owing to the high pressure conditions. The result indicates that 10% NH_3 addition to the reactant fuel mixture should produce flames with close to 7000 ppm of NO in the product gas.

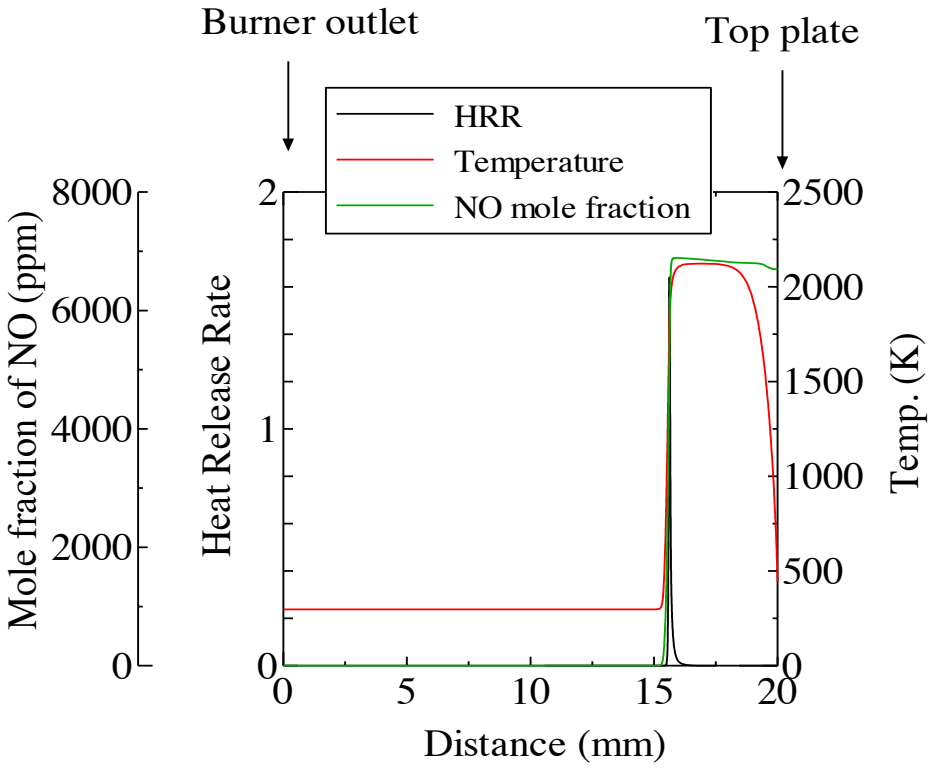

Fig. 6.11 1D strain stabilized CH_4-NH_3-air flame structure simulated using ChemKIN. Fuel mixture composed of 10% NH_3 and equivalence ratio, $\Phi = 0.9$

Grating spacing calibration

As discussed in section 3.3 a purely theoretical determination of the grating spacing can lead to systematic errors in the measured LITGS temperature. In practice, adjustments are made to the initial geometry to optimize the alignment for maximum signal, which can alter the grating spacing. In order to evaluate a more accurate value of the

grating spacing, a simple calibration procedure is used at a known temperature and gas composition.

Figure 6.12 shows the average of 20 shots of LITGS signal acquired in a flow of air with 5000 ppm of NO added to the mixture at 0.5 MPa. With the temperature in the stream measured using a thermocouple and the gas composition known, the corrected grating spacing is given by:

$$\Lambda = \frac{c_s}{f} = \frac{1}{f}\sqrt{\frac{\gamma k_b T}{W}} = 24.2\,\mu\text{m} \tag{6.2}$$

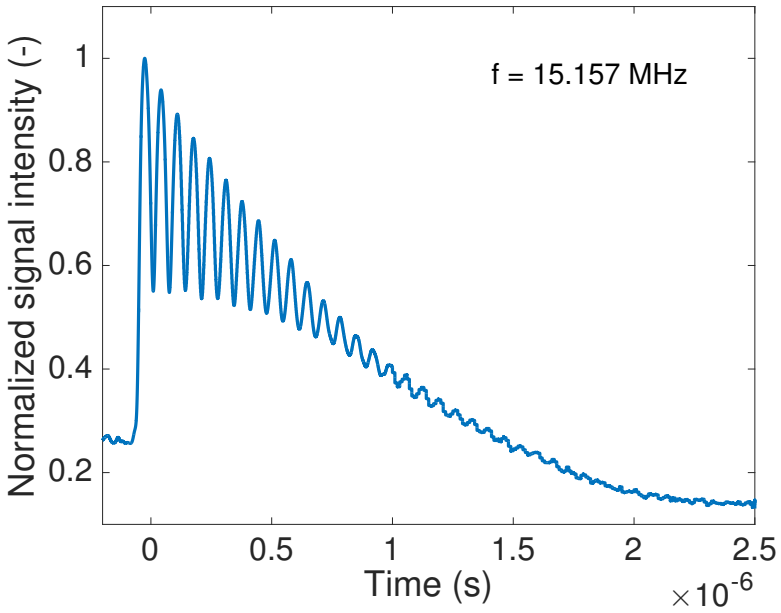

Fig. 6.12 NO-LITGS signal obtained for calibration of grating spacing. 0.5% NO in air at 5 bar

Flame measurements

Figures 6.13 (a) and (b) show representative single shots of LITGS signal for conditions where the ammonia content in the reactants is 10% and 20%, respectively. The zero origin for each shot is shifted to the point of maximum intensity. The signals acquired in the flame oscillate at higher frequencies and decay around ten times faster in the flames compared to the cold flow signals acquired for calibration of the grating spacing, where the optical geometries are identical. This is due to the greater speed of sound and faster thermal diffusion at flame temperatures.

Signal intensities acquired with 20% ammonia in the reactant mixture are slightly higher due to the higher mole fraction of NO in the burned gas. The signal contrast is also observably larger due to the lower flame temperature.

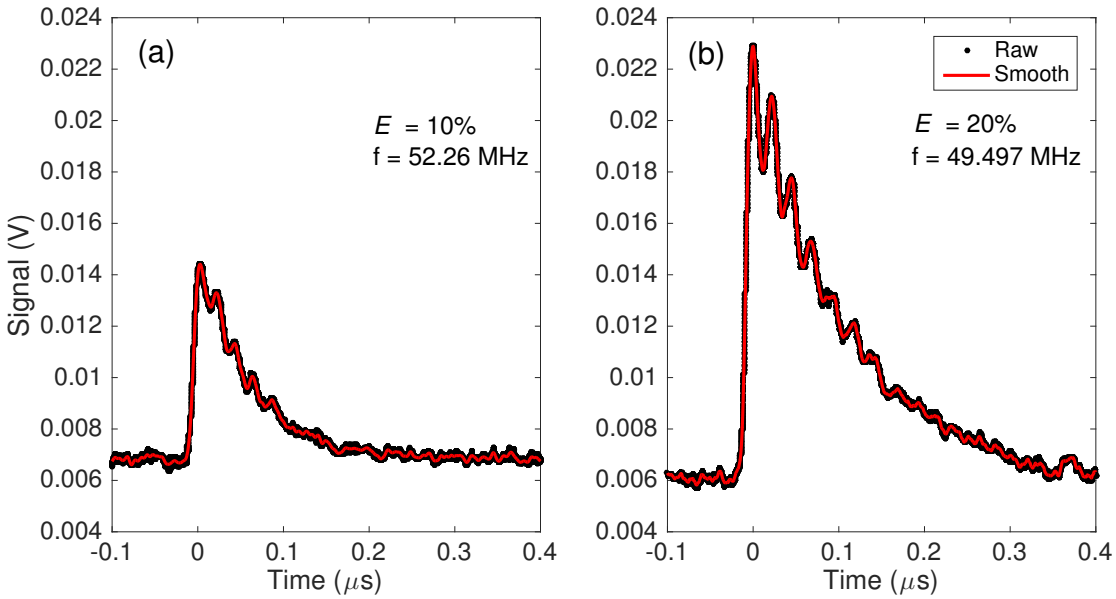

Fig. 6.13 Single shots of LITGS signal in CH_4-NH_3-air flames where fuel mixtures contained (a) 10% and (b) 20% NH_3. The measurement point is located at the centre of the burner, 19 mm above the burner outlet.

Figure 6.14 shows the average LITGS temperature for two conditions 19 mm above the burner outlet. The points represent the average temperatures and contrasts of 160 single shots of LITGS signal, respectively. The error bars indicate the standard deviation. The values of the specific heat ratio, γ, and the mean molecular weight, W, used in Eq. 2.13 were obtained from the expected molar fractions of species and temperature obtained from one-dimensional flame simulations at the corresponding height above the burner exit. As expected, an increase in the amount of NH_3 introduced into the fuel mixture leads to lower flame temperatures and higher signal contrasts.

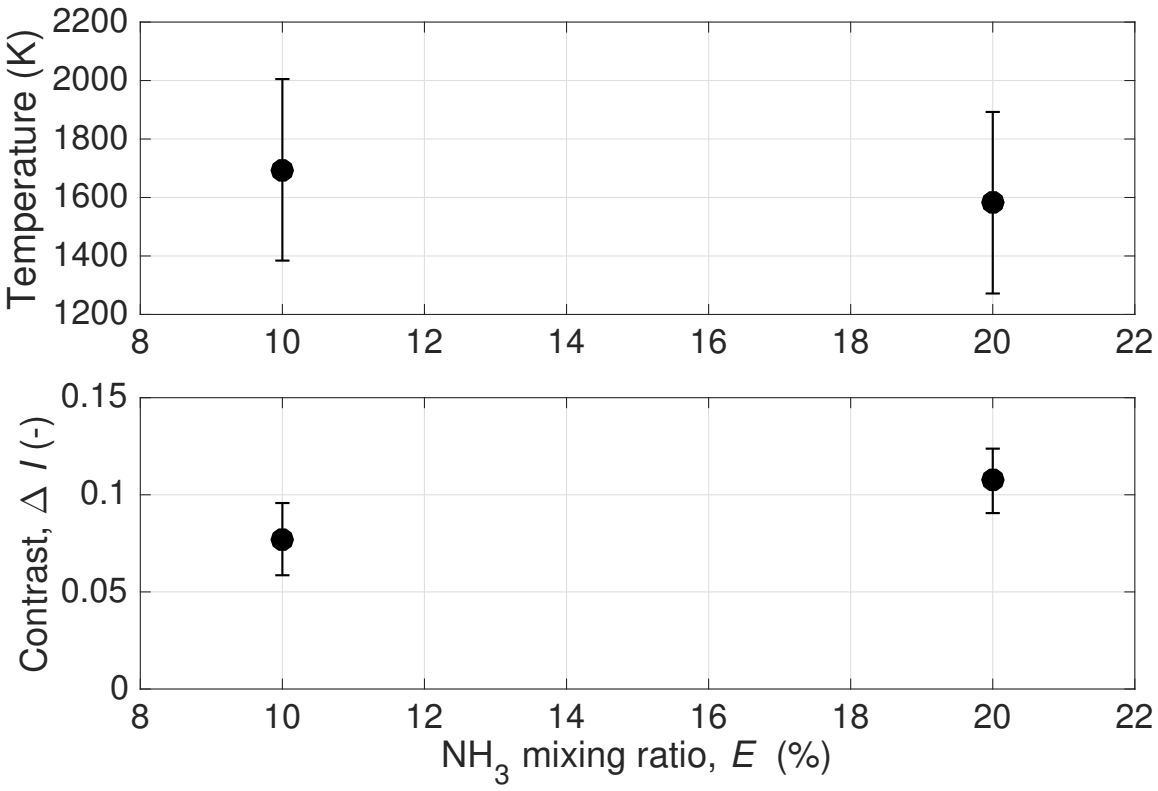

Fig. 6.14 Average LITGS temperature vs % of NH_3 in fresh-gas fuel mixture. Measurements acquired 19 mm above burner outlet. Each point is average of 160 single shots and error bars indicate standard deviation.

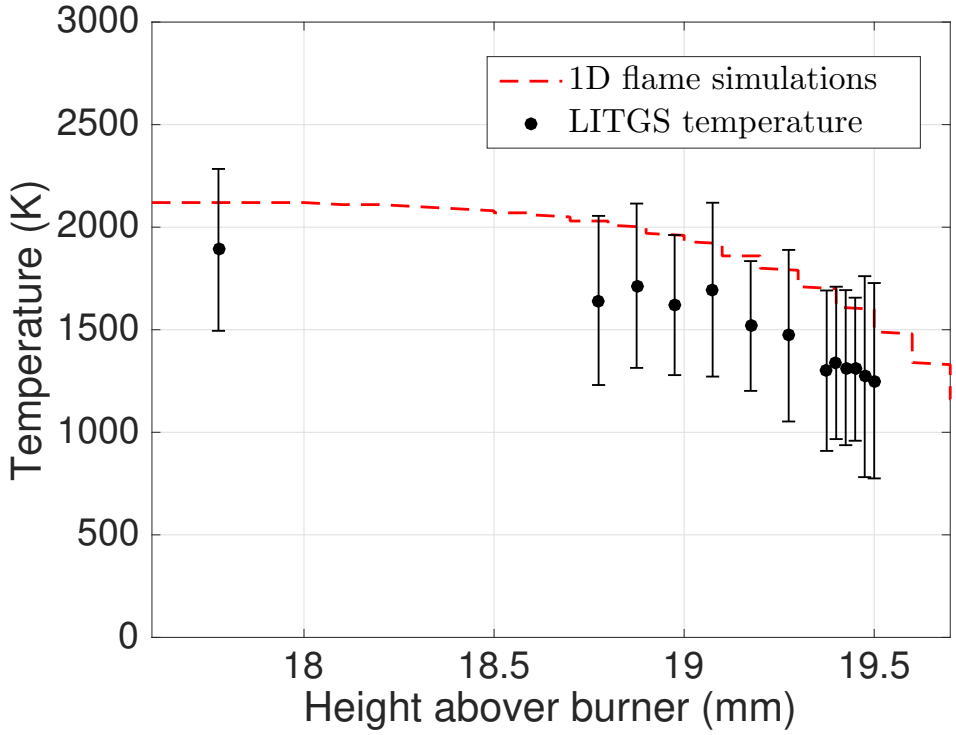

Fig. 6.15 LITGS temperature vs height above burner in CH_4-NH_3-air flame where Φ = 0.9. Dashed red line represents temperatures calculated from 1D strain-stabilized flame simulations.

Figure 6.15 shows the average LITGS temperature at several heights above the burner exit. All measurements were acquired at the center of the burner. Each point represents the mean temperature of 160 shots and the error bars indicate the standard deviation. The error reflects uncertainty in the oscillation frequency, gas composition (determined from 1D flame simulations) and non-uniformities in the flame. The red dashed line is data obtained from 1D flame simulations (see also Fig. 6.11) and shows a steady reduction in temperature towards the water-cooled stagnation plate, which is fixed 20 mm above the burner outlet. Measurements were acquired at various intervals to investigate the capability of NO-LITGS for spatially resolved measurements of temperature. The LITGS measurements appear to follow a similar trend to the simulated data, with the evaluated temperature steadily decreasing as the top-plate is

traversed closer to the probe volume. Unlike the data obtained in Chapter 5, at every position, the LITGS signal leads to estimations of the temperature below the simulated flame temperatures by around 200 – 250 K. The strain-stabilized ChemKin simulations were performed using the GRI-mech 3.0 chemical mechanism, which has not yet been fully validated for ammonia-methane combustion, so error in the simulation may account for the difference between the LITGS temperature and simulated temperature.

6.7 Summary

LITGS employing resonant excitation of NO to produce thermal gratings in the gas phase has been demonstrated for quantitative measurements of temperature in three environments – a static pressure cell at ambient temperature, a non-reacting heated jet at ambient pressure and a premixed CH_4-NH_3-air flame operating at 0.5 MPa.

NO-LITGS signals acquired at ambient temperatures where N_2 is used as a buffer gas were found to increase in strength with pressure, owing to greater collisional frequencies in mixtures with elevated densities. In the non-reacting air jet, where the pressure remained ambient, the LITGS signal intensity suffers with an increase in temperature due to the lower density mixtures. The signal decay time, which is an important parameter in maximizing the number of observable oscillations in (and hence the quality of) the LITGS signal, is longer in low temperature and high pressure mixtures.

Measurements of temperature were also performed in the burned gas region of a CH_4-NH_3-air flame at 0.5 MPa where, according to 1D flame simulations, we expect mole fractions of NO of around 6800 ppm. Measurements were acquired at various locations relative to a water-cooled stagnation plate, demonstrating the capability of LITGS measurements for measuring temperature gradients in combustion environments. Future

measurements could employ NO-doping in the fresh gas to allow for measurements through the reaction zone.

Chapter 7

Conclusions and future work

This final chapter is split into two parts. The first summarises the findings presented in Chapters 4, 5 and 6 and the second provides an outlook for potential future research on the development of LITGS into a more robust laser-based tool for thermometry in combustion.

7.1 Conclusions

The primary goal of this project was to investigate the potential for accurate and precise measurements of temperature using LITGS in both non-reacting and reacting flows. More specifically, the aims were to:

- Understand the factors that influence the local temperature rise within the probe volume due to LITGS and subsequently the accuracy of the measurements in cold-flow conditions.

- Demonstrate LITGS as a tool for thermometry using a range of absorbing species that exist in post-flame gases (i.e. OH and NO).
- Demonstrate the potential for systematic LITGS measurements under high temperature, high pressure conditions.
- Demonstrate the potential for spatially resolved measurements of temperature in flames.

The results of this investigation have been discussed in the previous chapters and highlight the potential as well as the limitations of LITGS as a tool for accurate and precise thermometry in reacting and non-reacting flows. The relationship between the local temperature rise in the LITGS probe volume detected by the absorption of energy as a function of the absorbing species mole fraction and laser pump intensity was investigated in Chapter 4 for two popular target species under cold-flow conditions, acetone and toluene. Systematic measurements of temperature in the burned gas regions of oxygen-enriched $CH_4/O_2/N_2$ flames for various conditions were demonstrated in Chapter 5 and spatially resolved measurements of temperature were acquired in the burned gas region of a high pressure stagnation plate stabilized CH_4/NH_3/air flame close to the water-cooled stagnation plate.

The primary conclusions drawn from the data acquired in the previous three chapters are as follows:

- LITGS can offer systematic measurements of temperature under a range of conditions in optically accessible, high pressure flames (demonstrated in $CH_4/O_2/N_2$ and CH_4/NH_3/air flames) with reasonable accuracy and precision. OH-LITGS measurements report measurement accuracies in the range of around 3 – 9% and a precision of 2 – 8% depending on the flame condition at which signal was

acquired. Flame conditions that produce low temperatures but high concentrations of OH in the burned gas produce stronger signal and hence more accurate measurements.

- The LITGS signal contrast and intensity suffers with an increase in temperature, making frequency extraction increasingly challenging at higher temperatures. However, LITGS can provide measurements in high temperature flames, demonstrated in this work under conditions where the flame temperature is as high as around 2800 K. This result highlights the potential for OH-LITGS as a tool for thermometry in rocket motors, where flames can contain large quantities of OH (e.g. H_2/O_2 combustion) and operate at higher pressures.

- LITGS measurements using resonant excitation of nitric oxide can be performed to acquire signals in both reacting and non-reacting environments with enough strength to evaluate temperature and potentially other thermodynamic parameters.

- Spatially resolved measurements of the burned gas temperature can be acquired using NO-LITGS in high pressure combustion environments that contain sufficient quantities of NO and have been demonstrated in a lean, premixed CH_4/NH_3/air flame.

- The accuracy of LITGS measurements is dependent on a knowledge of the gas composition in the measurement region. This limits the accuracy of measurements in flames that are difficult to model (e.g. flames that operate under fuel-rich conditions or flames where the detailed chemical mechanisms are not particularly well understood, such as in the case of CH_4/NH_3/air flames).

- The accuracy of LITGS measurements is also dependent on knowledge of the value of the grating spacing, Λ. Where possible, the grating spacing should

be calibrated under conditions where the temperature and gas composition are known. For the flames considered in Chapter 5, 3% inaccuracy in the value of the grating spacing can lead to 10% inaccuracy in the flame temperature measurements.

- The local temperature rise due to LITGS is proportional to $\frac{E_p \mathcal{A}}{\bar{c}_p T_0} \frac{\sigma}{A} X_v$ for both acetone/air and toluene/air mixtures. The efficiency of conversion of the incident laser energy into heat is around 7.8% for acetone. For toluene, the efficiency of conversion is around 4.4% for low pump powers and vapour mole fractions. Beyond $\frac{E_p \mathcal{A}}{\bar{c}_p T_0} \frac{\sigma}{A} X_v = 13.64$, the temperature rise saturates. High energies/ quantities of the absorbing species can lead to significant heating of the probe volume and inaccurate measurements, as shown in the cases of acetone and toluene absorption over a range of conditions.

- In order to obtain measurements that remain non-intrusive, one needs very small controllable pump powers and target species concentrations (of the order of ppm), but increased SNR to detect the disturbance in the probe volume due to LITGS. Hence, one requires a very good interaction zone (i.e. strong overlap) between the pump and probe beams, and a high power, low noise probe beam.

7.2 Future prospects

The work presented in this thesis demonstrates the potential of LITGS as an accurate, non-intrusive tool for the thermometry in reacting and non-reacting flows. The data presented here extends previous studies on LITGS thermometry in flames by demonstrating LITGS measurements using NO as an absorbing species and acquiring systematic measurements in high temperature, oxygen enriched combustion using OH as an absorber.

Further research into new applications for LITGS measurements and alternative target molecules with favourable absorption features is necessary to realise its full potential as a robust diagnostics tool. The following are suggestions for research avenues that are worth considering for future work to develop the LITGS diagnostic further:

Spatially resolved measurements through flame-front (NO doping)

In chapter 6, measurements mapping out the temperature profile in the burned gas region close to a water-cooled stagnation plate demonstrates the potential for spatially resolved thermometry in flames using LITGS. In combustion diagnostics, detailed observations of the local flame structure at the flame front are important for informing turbulent combustion models. Spatially resolved measurements of temperature using LITGS would require the existence of an absorbing species in both the fresh gas and burned gas region. Doping small quantities of NO in the reactant mixture could allow for measurements through the flame, with the main limiting factor being the spatial resolution achievable with LITGS.

For typical pump/probe powers and an optical geometry similar to the configuration employed in Chapter 6, at least 500 ppm of NO should be added to the burned gas to obtain signal at 0.5 MPa. Note that at high pressure, NO is reported to convert to NO_2 [117]. In such cases, NO_2 resulting from NO doping could also be targeted with 532 nm excitation.

Measurements through flame fronts would require careful consideration of the following challenges:

- Index gradients across the flame-front are likely to smear the grating. They will also make the probe beam cross in potentially unknown routes and the associated cylinder lens will cause it to bloom.
- The mix of collider molecules will change radically across a flame front, making accurate temperature determination very difficult given that the collisional partner (i.e. CO_2, N_2, O_2) directly affects the strength of the thermal grating [93].

Temporally resolved LITGS

In this thesis, all flame measurements were performed in the burned gas of laminar premixed flames where temporal fluctuations in temperature are considered minimal. The measurements presented here were acquired using a pump laser that operates at a repetition rate of 10 Hz, limiting the time resolution of the measurements.

Forster *et al.* [36] recently reported high-speed acquisition of LITGS signals (up to 10 kHz) in a static pressure cell where NO_2 is used as an absorbing species. Some combustion phenomena can be characterized by temporal fluctuations in temperature. As an example, entropy spots are pressure perturbations generated from unsteady heat

release in high pressure flames and travel with the mean flow until they are accelerated at the outlet nozzle of the combustion chamber [25].

High frequency LITGS measurements could be used to measure temporal fluctuations in temperature, which act as a marker for the the mechanism of the production of entropy waves, as well as the nature of their dispersion and diffusion. This is currently the subject of ongoing work in the Department of Engineering, University of Cambridge and Fig. 7.1 shows a single-shot of LITGS signal acquired as part of an effort to measure temperature fluctuations due to entropy waves at 1 kHz in air with small quantities of biacetyl added to the mixture for 355 nm pump excitation.

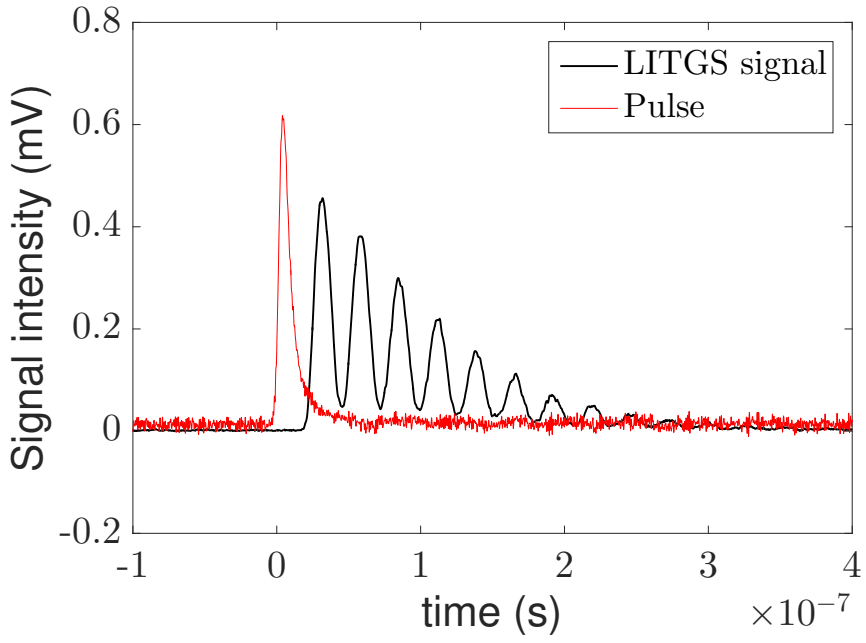

Fig. 7.1 Typical single-shot of biacetyl-LITGS acquired using high speed laser for measurements of entropy spots

References

[1] Aldén, M., Bengtsson, P.-E., Edner, H., Kröll, S., and Nilsson, D. (1989). Rotational CARS: a comparison of different techniques with emphasis on accuracy in temperature determination. *Appl. Opt.*, 28(15):3206–3219.

[2] Almodovar, C. A., Spearrin, R. M., and Hanson, R. K. (2017). Two-color laser absorption near 5 μm for temperature and nitric oxide sensing in high-temperature gases. *Journal of Quantitative Spectroscopy and Radiative Transfer*, 203:572 – 581.

[3] Ambrose, D., Sprake, C., and Townsend, R. (1974). Thermodynamic properties of organic oxygen compounds XXXIII. The vapour pressure of acetone. *The Journal of Chemical Thermodynamics*, 6(7):693–700.

[4] Attal-Trétout, B., Schmidt, S., Crété, E., Dumas, P., and Taran, J. (1990). Resonance CARS of OH in high-pressure flames. *Journal of Quantitative Spectroscopy and Radiative Transfer*, 43(5):351 – 364.

[5] Barker, P. F., Grinstead, J. H., and Miles, R. B. (1999). Single-pulse temperature measurement in supersonic air flow with predissociated laser-induced thermal gratings. 168(1):177 – 182.

[6] Battles, B. E. and Hanson, R. K. (1995). Laser-induced fluorescence measurements of NO and OH mole fraction in fuel-lean, high-pressure (1–10 atm) methane flames: Fluorescence modeling and experimental validation. *Journal of Quantitative Spectroscopy and Radiative Transfer*, 54(3):521 – 537.

[7] Bervas, H., Attal-Tretout, B., Boiteux, S. L., and Taran, J. P. (1992). OH detection and spectroscopy by DFWM in flames; comparison with CARS. *Journal of Physics B: Atomic, Molecular and Optical Physics*, 25(5):949.

[8] Besley, L. M., Standards, N., Wales, N. S., and Bottomley, G. A. (1974). Vapour pressure of toluene from 273.15 K to 298.15 K. *Journal of Chemical Thermodynamics*, 23:577–580.

[9] Bessler, W. and Schulz, C. (2004). Quantitative multi-line NO-LIF temperature imaging. *Applied Physics B*, 78(5):519–533.

[10] Beyrau, F., Bräuer, A., Seeger, T., and Leipertz, A. (2004). Gas-phase temperature measurement in the vaporizing spray of a gasoline direct-injection injector by use of pure rotational coherent anti-Stokes Raman scattering. *Opt. Lett.*, 29(3):247–249.

[11] Boretti, A. (2017). Novel dual fuel diesel-ammonia combustion system in advanced TDI engines. *International Journal of Hydrogen Energy*, 42(10):7071 – 7076.

[12] Brackmann, C., Bood, J., Afzelius, M., and Bengtsson, P.-E. (2004). Thermometry in internal combustion engines via dual-broadband rotational coherent anti-Stokes Raman spectroscopy. *Measurement Science and Technology*, 15(3):R13.

[13] Brackmann, C., Bood, J., Bengtsson, P.-E., Seeger, T., Schenk, M., and Leipertz, A. (2002). Simultaneous vibrational and pure rotational coherent anti-Stokes Raman spectroscopy for temperature and multispecies concentration measurements demonstrated in sooting flames. *Appl. Opt.*, 41(3):564–572.

[14] Brown, M. S., Li, Y., Roberts, W. L., and Gord, J. R. (2003). Analysis of Transient-Grating Signals for Reacting-Flow Applications. *Applied Optics*, 42(3):566.

[15] Cheng, T. S., Yuan, T., Lu, C.-C., and Chao, Y.-C. (2002). The application of spontaneous vibrational raman scattering for temperature measurements in high pressure laminar flames. *Combustion Science and Technology*, 174(5-6):111–128.

[16] Crutzen, P. J. (1979). The role of NO and NO_2 in the chemistry of the troposphere and stratosphere. *Annual Review of Earth and Planetary Sciences*, 7:443–472.

[17] Cummings, E. B. (1994). Laser-induced thermal acoustics: simple accurate gas measurements. *Optics Letters*, 19(17):1361.

[18] Cummings, E. B., Brown, M. S., DeBarber, P. A., and Hornung, H. G. (1995). Measurement of gas-phase sound speed and thermal diffusivity over a broad pressure range using laser-induced thermal acoustics. *Optics Letters*, 20(14):1577.

[19] Cédric, L., Goriaux, M., Tassel, P., Perret, P., André, M., and Liu, Y. (2016). Impact of aftertreatment device and driving conditions on black carbon, ultrafine particle and NOx emissions for Euro 5 diesel and gasoline vehicles. *Transportation Research Procedia*, 14:3079 – 3088. Transport Research Arena TRA2016.

[20] Daily, J. W. (1997). Laser induced fluorescence spectroscopy in flames. *Progress in Energy and Combustion Science*, 23(2):133 – 199.

[21] Danehy, P., Friedman-Hill, E., and Lucht, R. (1993). The effects of collisional quenching on degenerate four-wave mixing. *AAppl. Phys. B*, 57(4):243 – 248.

[22] Danehy, P. M., Paul, P. H., and Farrow, R. L. (1995). Thermal-grating contributions to degenerate four-wave mixing in nitric oxide. *J. Opt. Soc. Am. B*, 12(9):1564–1576.

[23] Dennis, C. N., Slabaugh, C. D., Boxx, I. G., Meier, W., and Lucht, R. P. (2016). 5 kHz thermometry in a swirl-stabilized gas turbine model combustor using chirped probe pulse femtosecond CARS . Part 1 : Temporally resolved swirl-flame thermometry. *Combustion and Flame*, 173:441–453.

[24] Dieke, G. and Crosswhite, H. (1962). The ultraviolet bands of OH fundamental data. *Journal of Quantitative Spectroscopy and Radiative Transfer*, 2(2):97 – 199.

[25] Domenico, F. D., Rolland, E. O., and Hochgreb, S. (2017). Detection of direct and indirect noise generated by synthetic hot spots in a duct. *Journal of Sound and Vibration*, 394:220 – 236.

[26] Dreier, T. and Rakestraw, D. J. (1990). Measurement of OH rotational temperatures in a flame using degenerate four-wave mixing. *Opt. Lett.*, 15(1):72–74.

[27] Dreizler, A., Dreier, T., and Wolfrum, J. (1995). Thermal grating effects in infrared degenerate four-wave mixing for trace gas detection. 2614(February).

[28] Eckbreth, A. (1996). *Laser Diagnostics for Combustion Temperature and Species*. CRC Press.

[29] Eckbreth, A. C., Bonczyk, P. A., and Verdieck, J. F. (1979). Combustion diagnostics by laser Raman and fluorescence techniques. *Progress in Energy and Combustion Science*, 5(4):253 – 322.

[30] Eichler, H.J, G. and P. Pohl, D. (1986). *Laser-Induced Dynamic Gratings*, volume 1. Springer Series in Optical Sciences.

[31] EPA (2012). Standards of performance for stationary combustion turbines. *US Federal Register*, 77(168).

[32] Ewart, P. and O'Leary, S. V. (1986). Detection of OH in a flame by degenerate four-wave mixing. *Opt. Lett.*, 11(5):279–281.

[33] Ewart, P. and Snowdon, P. (1990). Multiplex degenerate four-wave mixing in a flame. *Opt. Lett.*, 15(23):1403–1405.

[34] Farrow, R. and Rakestraw, D. (1999). Analysis of degenerate four-wave mixing spectra of NO in a $CH_4/N_2/O_2$ flame. *Applied Physics B*, 68(4):741–747.

[35] Flieser, J., Iskra, K., Morozov, A., Pichler, G., and Neger, T. (1998). Combustion flame diagnostics using degenerate four-wave mixing: the dipole moment power law and rotational temperature for nitric oxide. *Journal of Physics D: Applied Physics*, 31(4):402.

[36] Förster, F. J., Crua, C., Davy, M., and Ewart, P. (2017). Time-resolved gas thermometry by laser-induced grating spectroscopy with a high-repetition rate laser system. *Experiments in Fluids*, 58(7):87.

[37] Fuest, F., Barlow, R. S., Magnotti, G., Dreizler, A., Ekoto, I. W., and Sutton, J. A. (2015). Quantitative acetylene measurements in laminar and turbulent flames using 1-D Raman/Rayleigh scattering. *Combustion and Flame*, 162(5):2248–2255.

[38] Gao, Y., Bohlin, A., Seeger, T., Bengtsson, P.-E., and Kliewer, C. J. (2013). In situ determination of N_2 broadening coefficients in flames for rotational CARS thermometry. *Proceedings of the Combustion Institute*, 34(2):3637–3644.

[39] Gao, Y., Seeger, T., and Leipertz, A. (2015). ScienceDirect Development of temperature evaluation of pure Rotational Coherent Anti-Stokes Raman Scattering (RCARS) spectra influenced by spatial averaging effects. *Proceedings of the Combustion Institute*, 35(3):3715–3722.

[40] Giezendanner-Thoben, R., Meier, U., Meier, W., and Aigner, M. (2005). Phase-locked temperature measurements by two-Line OH-PLIF thermometry of a self-excited combustion instability in a gas turbine model combustor. *Flow, Turbulence and Combustion*, 75:317–333.

[41] Glassman, I. and Yetter, R. A. (2008). Chapter 8 - Environmental Combustion Considerations. In *Combustion (Fourth Edition)*, pages 409 – 494. Academic Press, Burlington.

[42] Govoni, D., Booze, J., Sinha, A., and Crim, F. (1993). The non-resonant signal in laser-induced grating spectroscopy of gases. *Chemical Physics Letters*, 216(3):525 – 529.

[43] Granovskii, M., Dincer, I., and Rosen, M. A. (2007). Greenhouse gas emissions reduction by use of wind and solar energies for hydrogen and electricity production: Economic factors. *International Journal of Hydrogen Energy*, 32(8):927 – 931.

[44] Grisch, F., Bouchardy, P., and Clauss, W. (2003). CARS thermometry in high pressure rocket combustors. *Aerospace Science and Technology*, 7(4):317 – 330.

[45] Gupta, M. and Ballato, J. (2006). *The Handbook of Photonics, Second Edition*. CRC Press.

[46] Haas, Y. (2004). Photochemical -cleavage of ketones : revisiting acetone. *Journal of Photochemistry and Photobiology A*, 57(1:3).

[47] Hanson, R. K., Seitzman, J. M., and Paul, P. H. (1990). Planar laser-fluorescence imaging of combustion gases. *Applied Physics B*, 50(6):441–454.

[48] Hayakawa, A., Gao, Y., Lowe, S., and Hochgreb, S. (2016). Quantitative temperature measurements of toluene/air mixtures using Laser Induced Thermal Grating Spectroscopy (LITGS). *Proceedings of the Mechanical Engineering Congress, 2016 Japan (MECJ-16)*, 16-1:G0600101.

[49] Hayakawa, A., Yamagami, T., Takeuchi, K., Higuchi, Y., Kudo, T., Lowe, S., Gao, Y., Hochgreb, S., and Kobayashi, H. (2018). Quantitative measurements of temperature in oxygen enriched $CH_4/O_2/N_2$ premixed flames using Laser Induced Thermal Grating Spectroscopy (LITGS) up to 1.0 MPa. *Proceedings of the Combustion Institute - submitted, draft available.*

[50] Helmut H. T., Angel González Ureña, R. J. (2007). *Laser Chemistry: Spectroscopy, Dynamics and Applications.* John Wiley & Sons.

[51] Hemmerling, B., Kozlov, D., Stel'makh, O., and Attal-Trétout, B. (2006). Diagnostics of water-containing gas mixtures using thermal laser-induced gratings. *Chemical Physics*, 320(2-3):103–117.

[52] Herring, G., Roberts, W. L. Brown, M., and DeBarber, P. A. (1996). Temperature measurement by degenerate four-wave mixing with strong absorption of the excitation beams. *Applied Optics*, 33:6544–6547.

[53] Hubschmid, W., Hemmerling, B., and Stampanoni-Panariello, A. (1995). Rayleigh and Brillouin modes in electrostrictive gratings. *Journal of the Optical Society of America B*, 12(10):1850.

[54] Hult, J., Burns, I. S., and Kaminski, C. F. (2005). Two-line atomic fluorescence flame thermometry using diode lasers. *Proceedings of the Combustion Institute*, 30(1):1535–1543.

[55] Hussong, J., Lückerath, R., Stricker, W., Bruet, X., Joubert, P., Bonamy, J., and Robert, D. (2001). Hydrogen CARS thermometry in a high-pressure H_2 air flame.

test of H_2 temperature accuracy and influence of line width by comparison with N_2 CARS as reference. *Applied Physics B*, 73(2):165–172.

[56] Jarrett, O., Antcliff, R. R., and Smith, M. W. (1991). CARS temperature measurements in turbulent and supersonic facilities. *JNASA Langley Research Centre*.

[57] Jiang, J. and Li, D. (2016). Theoretical analysis and experimental confirmation of exhaust temperature control for diesel vehicle NO_x emissions reduction. *Applied Energy*, 174:232 – 244.

[58] Johansen, C. T., McRae, C. D., Danehy, P. M., Gallo, E. C. A., Cantu, L. M. L., Magnotti, G., Cutler, A. D., Rockwell, R. D., Goyne, C. P., and McDaniel, J. C. (2014). OH-PLIF visualization of the UVA supersonic combustion experiment: configuration A. *Journal of Visualization*, 17(2):131–141.

[59] Jones, W. P. (1975). The effect of temporal fluctuations in temperature on nitric oxide formation. *Combustion Science and Technology*, 10(1-2):93–96.

[60] Joo, J., Lee, S., and Kwon, O. (2012). Effects of ammonia substitution on combustion stability limits and NO_x emissions of premixed hydrogen–air flames. *International Journal of Hydrogen Energy*, 37(8):6933 – 6941. III Iberian Symposium on Hydrogen, Fuel Cells and Advanced Batteries, HYCELTEC-2011.

[61] Jorgensen, F. R. A. and Zuiderwyk, M. (1985). Two-colour pyrometer measurement of the temperature of individual combusting particles. *Journal of Physics E: Scientific Instruments*, 18(6):486.

[62] Ju, J. J., seok Ryu, J., Park, C. W., and Hahn, J. W. (2001). Degenerate four wave mixing of C_2 in forward geometry: Spectral lineshape analysis and temperature determination. *Japanese Journal of Applied Physics*, 40(2R):841.

[63] Kaminski, C. F., Hughes, I. G., Lloyd, G. M., and Ewart, P. (1996). Thermometry of an oxy-acetylene flame using multiplex degenerate four-wave mixing of C_2. *Applied Physics B*, 62(1):39–44.

[64] Katsuki, M., Mizutani, Y., and Matsumoto, Y. (1987). An Improved Thermocouple Technique for Measurement of Fluctuating Temperatures in Flames. *Combustion and Flame*, 36:27–36.

[65] Kearney, S. P. (2015). Hybrid fs/ps rotational CARS temperature and oxygen measurements in the product gases of canonical flat flames. *Combustion and Flame*, 162(5):1748 – 1758.

[66] Khalil, A. E. and Gupta, A. K. (2014). Hydroxyl radical distribution in distributed reaction combustion condition. *Fuel*, 122:28 – 35.

[67] Khidr, K. I., Eldrainy, Y. A., and EL-Kassaby, M. M. (2017). Towards lower gas turbine emissions: Flameless distributed combustion. *Renewable and Sustainable Energy Reviews*, 67:1237 – 1266.

[68] Kiefer, J. and Ewart, P. (2011). Laser diagnostics and minor species detection in combustion using resonant four-wave mixing. *Progress in Energy and Combustion Science*, 37(5):525–564.

[69] Kiefer, J., Tröger, J. W., Li, Z., Seeger, T., Aldén, M., and Leipertz, A. (2012). Laser-induced breakdown flame thermometry. *Combustion and Flame*, 159(12):3576–3582.

[70] Kobayashi, H. (2002). Experimental study of high-pressure turbulent premixed flames. *Experimental Thermal and Fluid Science*, 26:375–387.

[71] Kobayashi, H., Nakashima, T., Tamura, T., Maruta, K., and Niioka, T. (1997). Turbulence measurements and observations of turbulent premixed flames at elevated pressures up to 3.0 MPa. *Combustion and Flame*, 108(1):104 – 117.

[72] Koch, J. D., Gronki, J., and Hanson, R. K. (2008). Measurements of near-UV absorption spectra of acetone and 3-pentanone at high temperatures. *Journal of Quantitative Spectroscopy and Radiative Transfer*, 109(11):2037–2044.

[73] Kohse-Höinghaus, K., Meier, U., and Attal-Trétout, B. (1990). Laser-induced fluorescence study of OH in flat flames of 1–10 bar compared with resonance CARS experiments. *Applied Optics*, 29(10):1560–1569.

[74] Kojima, J. and Nguyen, Q.-V. (2004). Measurement and simulation of spontaneous raman scattering in high-pressure fuel-rich H_2–air flames. *Measurement Science and Technology*, 15(3):565.

[75] Kremer, H., May, F., and Wirtz, S. (2001). The influence of furnace design on the NO formation in high temperature processes. *Journal of Energy Conversion and Management*, 42:1937–1952.

[76] Kristensson, E., Ehn, A., Bood, J., and Aldén, M. (2015). Advancements in Rayleigh scattering thermometry by means of structured illumination. *Proceedings of the Combustion Institute*, 35:3689–3696.

[77] Kulatilaka, W. D., Chai, N., Naik, S. V., Laurendeau, N. M., Lucht, R. P., Kuehner, J. P., Roy, S., and Gord, J. R. (2006). Measurement of nitric oxide concentrations in flames by using electronic-resonance-enhanced coherent anti-stokes Raman scattering. *Opt. Lett.*, 31(22):3357–3359.

[78] Kulatilaka, W. D., Chai, N., Naik, S. V., Roy, S., Laurendeau, N. M., Lucht, R. P., Kuehner, J. P., and Gord, J. R. (2007). Effects of pressure variations on electronic-resonance-enhanced coherent anti-Stokes Raman scattering of nitric oxide. *Optics Communications*, 274:441–446.

[79] Kumar, A., Uddi, M., and Sung, C.-j. (2012). Two-line thermometry and H_2O measurement for reactive mixtures in rapid compression machine. *Combustion and Flame*, 159(12):3493–3501.

[80] Köser, J., Becker, L. G., Goßmann, A.-K., Böhm, B., and Dreizler, A. (2017). Investigation of ignition and volatile combustion of single coal particles within oxygen-enriched atmospheres using high-speed OH-PLIF. *Proceedings of the Combustion Institute*, 36(2):2103 – 2111.

[81] Lafolletie, R. M., Hedman, P. O., and Smith, P. J. (1989). An analysis of coal particle temperature measurements with two-color optical pyrometers. *Combustion Science and Technology*, 66(1-3):93–105.

[82] Latzel, H., Dreizler, A., Dreier, T., Heinze, J., Dillmann, M., Stricker, W., Lloyd, G., and Ewart, P. (1998). Thermal grating and broadband degenerate four-wave mixing spectroscopy of OH in high-pressure flames. *Applied Physics B: Lasers and Optics*, 67(5):667–673.

[83] Laurendeau, N. M. (1988). Temperature measurements by light-scattering methods. *Progress in Energy and Combustion Science*, 14(2):147–170.

[84] Lee, T., Bessler, W. G., Kronemayer, H., Schulz, C., and Jeffries, J. B. (2005). Quantitative temperature measurements in high-pressure flames with multiline NO-LIF thermometry. *Appl. Opt.*, 44(31):6718–6728.

[85] Li, J., Huang, H., Kobayashi, N., He, Z., and Nagai, Y. (2014). Study on using hydrogen and ammonia as fuels: Combustion characteristics and NO_x formation. *International Journal of Energy Research*, 38(9):1214–1223. ER-13-3429.R1.

[86] Lindstedt, P. (1998). Modeling of the chemical complexities of flames. *Symposium (International) on Combustion*, 27(1):269 – 285. 27th International Sysposium on Combustion.

[87] Linstrom, P. J. and Mallard, W. G., editors (2005). *NIST Chemistry WebBook, NIST Standard Reference Database Number 69*. National Institute of Standards and Technology, Gaithersburg MD, 20899.

[88] Lloyd, G., Hughes, I., Bratfalean, R., and Ewart, P. (1998). Broadband degenerate four-wave mixing of OH for flame thermometry. *Applied Physics B*, 67(1):107–113.

[89] Maclean, D. I. and Wagner, H. G. (1967). The structure of the reaction zones of ammonia-oxygen and hydrazine-decomposition flames. *Symposium (International) on Combustion*, 11(1):871–878.

[90] Masquelet, M., Menon, S., Jin, Y., and Friedrich, R. (2009). Simulation of unsteady combustion in a LOX-GH 2 fueled rocket engine. *Aerospace Science and Technology*, 13(8):466–474.

[91] Mathieu, O. and Petersen, E. L. (2015). Experimental and modeling study on the high-temperature oxidation of ammonia and related NOx chemistry. *Combustion and Flame*, 162(3):554 – 570.

[92] McCormack, E., Pratt, S., Dehmer, P., and Dehmer, J. (1993). Double-resonance laser-induced grating spectroscopy of nitric oxide. *Chemical Physics Letters*, 211(1):147 – 155.

[93] McCormack, E. F., Dehmer, P. M., Dehmer, J. L., and Pratt, S. T. (1995). Multistate interactions in nitric oxide probed by laser-induced grating spectroscopy. *The Journal of Chemical Physics*, 102(12):4740–4746.

[94] Miller, J. A., Smooke, M. D., Green, R. M., and Kee, R. J. (1983). Kinetic modeling of the oxidation of ammonia in flames. *Combustion Science and Technology*, 34(1-6):149–176.

[95] Murphy, R., Lee, E., and Hart, A. (1975). Quenching of vibrationally excited nitric oxide by molecular oxygen and nitrogen. *Journal of Chemical Physics*, 63:2919–2925.

[96] Niioka, T., Tsukata, K., and J., S. (2001). *Fundamentals of Combustion*. Ohm. inc, 2nd edition.

[97] Okafor, E., Naito, Y., Colson, S., Ichikawa, A., Kuda, T., Hayakawa, A., and Kobayashi, H. (2017). Optimization and validation of detailed reaction mechanisms for CH_4-NH_3-Air premixed flames. *Heat transfer symposium*, 38(9).

[98] Patnaik, A. K., Roy, S., Lucht, R. P., and Gord, J. R. (2008). Collisional effects on molecular dynamics in electronic-resonance-enhanced CARS. *Journal of Modern Optics*, 55(19-20):3263–3272.

[99] Paul, P. H., Farrow, R. L., and Danehy, P. M. (1995). Gas-phase thermal-grating contributions to four-wave mixing. *Journal of the Optical Society of America B*, 12(3):384–392.

[100] Pratt, D. T. (1967). Performance of ammonia-fired gas-turbine combustors. *Technical Report No.9, DA-04-200-AMC-791(x), UC Berkeley.*

[101] Praveena, V. and Martin, M. L. J. (2017). A review on various after treatment techniques to reduce NOx emissions in a CI engine. *Journal of the Energy Institute*.

[102] Razykov, T., Ferekides, C., Morel, D., Stefanakos, E., Ullal, H., and Upadhyaya, H. (2011). Solar photovoltaic electricity: Current status and future prospects. *Solar Energy*, 85(8):1580 – 1608. Progress in Solar Energy 1.

[103] R.C.Weast (1972). *Handbook of Chemistry and Physics*. Chemical Rubber Pub., 53rd edition.

[104] Reaction-Design (2013). CHEMKIN-PRO - Release:15101. *San Diego*.

[105] Richardson, D. R., Bangar, D., and Lucht, R. P. (2012). Polarization suppression of the nonresonant background in femtosecond coherent anti-Stokes Raman scattering for flame thermometry at 5 kHz. *Opt. Express*, 20(19):21495–21504.

[106] Rosa, M. D. D., Klavuhn, K. G., and Hanson, R. K. (1996). LIF spectroscopy of NO and O_2 in high-pressure flames. *Combustion Science and Technology*, 118(4-6):257–283.

[107] Ross, D. (2006). Hydrogen storage: The major technological barrier to the development of hydrogen fuel cell cars. *Vacuum*, 80(10):1084 – 1089. The World Energy Crisis: Some Vacuum-based Solutions.

[108] Rothman, L., Gordon, I., Babikov, Y., Barbe, A., Benner, D. C., Bernath, P., Birk, M., Bizzocchi, L., Boudon, V., Brown, L., Campargue, A., Chance, K., Cohen, E., Coudert, L., Devi, V., Drouin, B., Fayt, A., Flaud, J.-M., Gamache, R., Harrison, J., Hartmann, J.-M., Hill, C., Hodges, J., Jacquemart, D., Jolly, A., Lamouroux, J., Roy, R. L., Li, G., Long, D., Lyulin, O., Mackie, C., Massie, S., Mikhailenko, S., Müller, H., Naumenko, O., Nikitin, A., Orphal, J., Perevalov, V., Perrin, A., Polovtseva, E., Richard, C., Smith, M., Starikova, E., Sung, K., Tashkun, S., Tennyson, J., Toon, G., Tyuterev, V., and Wagner, G. (2013). The HITRAN2012 molecular spectroscopic database. *Journal of Quantitative Spectroscopy and Radiative Transfer*, 130:4 – 50. HITRAN2012 special issue.

[109] Roy, S., Gord, J. R., and Patnaik, A. K. (2010). Recent advances in coherent anti-Stokes Raman scattering spectroscopy: Fundamental developments and applications in reacting flows. *Progress in Energy and Combustion Science*, 36(2):280 – 306.

[110] Roy, S., Meyer, T. R., Lucht, R. P., Belovich, V. M., Corporan, E., and Gord, J. R. (2004). Temperature and CO_2 concentration measurements in the exhaust stream of a liquid-fueled combustor using dual-pump coherent anti-Stokes Raman scattering (CARS) spectroscopy. *Combustion and Flame*, 138(3):273 – 284.

[111] Sahlberg, A.-L., Hot, D., Kiefer, J., and Aldén, M. (2016). Mid-infrared laser-induced thermal grating spectroscopy in flames. *Proceedings of the Combustion Institute*, in press:1–9.

[112] Sanjay, M. S. (1993). A review of NOx formation under gas-turbine combustion conditions. *Combustion Science and Technology*, 87(1-6):329–362.

[113] Savitzky, A. and Golay, M. J. E. (1964). Smoothing and differentiation of data by simplified least squares procedures. *Journal of Analytical Chemistry*, 36:1627–1639.

[114] Sepman, A. V., Toro, V. V., Mokhov, A. V., and Levinsky, H. B. (2013). Determination of temperature and concentrations of main components in flames by fitting measured raman spectra. *Applied Physics B*, 112(1):35–47.

[115] Shanker, T. and Singh, R. K. (2012). Wind energy conversion system: A review. In *2012 Conference on Engineering and Systems*, pages 1–6.

[116] Silfvast, W. T. (2004). *Laser Fundamentals*. Cambridge University Press, 2nd edition.

[117] Skalska, K., Miller, J. S., and Ledakowicz, S. (2010). Kinetics of nitric oxide oxidation. *Chemical Papers*, 64(2):269–272.

[118] Skovorodko, P. A., Tereshchenko, A. G., Knyazkov, D. A., Paletsky, A. A., and Korobeinichev, O. P. (2012). Experimental and numerical study of thermocouple-induced perturbations of the methane flame structure. *Combustion and Flame*, 159(3):1009–1015.

[119] Smith, G. P., Golden, D. M., Frenklach, M., Eiteener, B., Goldenberg, M., Bowman, C. T., Hanson, R. K., Gardiner, W. C., Lissianski, V. V., and Qin, Z. W. (2000). GRI-Mech 3.0 - http://www.me.berkeley.edu/gri_mech/.

[120] Smith, J. J., Schneider, G., Suslov, D., Oschwald, M., and Haidn, O. (2007). Steady-state high pressure LO_x/H_2 rocket engine combustion. *Aerospace Science and Technology*, 11(1):39:47.

[121] Spearrin, R. M., Schultz, I. A., Jeffries, J. B., and Hanson, R. K. (2014). Laser absorption of nitric oxide for thermometry in high-enthalpy air. *Measurement Science and Technology*, 25(12).

[122] Stampanoni-Panariello, A. and Kozlov, D.N., R. P. (2005). *Gas phase diagnostics by laser-induced gratings I: theory*, volume 81. Applied Physics B.

[123] Stelzner, B., Weis, C., Habisreuther, P., Zarzalis, N., and Trimis, D. (2017). Super-adiabatic flame temperatures in premixed methane flames: A comparison between oxy-fuel and conventional air combustion. *Fuel*, 201:148 – 155. 1st International Workshop on Oxy-Fuel Combustion.

[124] Stevens, R. and Ewart, P. (2004). Single-shot measurement of temperature and pressure using laser-induced thermal gratings with a long probe pulse. *Applied Physics B: Lasers and Optics*, 78(1):111–117.

[125] Stevens, R., Ewart, P., Ma, H., and Stone, C. (2007). Measurement of nitric oxide concentration in a spark-ignition engine using degenerate four-wave mixing. *Combustion and Flame*, 148(4):223 – 233.

[126] Stricker, W., Lückerath, R., Meier, U., and Meier, W. (2003). Temperature measurements in combustion—not only with CARS: a look back at one aspect of the european CARS workshop. *Journal of Raman Spectroscopy*, 34(12):922 – 931.

[127] Sutcliffe, L. H. and Walsh, A. D. (1953). The ultra-violet absorption spectrum of nitric oxide. *Proceedings of the Physical Society. Section A*, 66(3):209.

[128] Takeuchi, K., Nunome, Y., Tomioka, S., Tomita, T., Kudo, T., Hayakawa, A., and Kobayashi, H. (2016a). Application of OH (2,0) band excitation Planar Laser Induced Fluorescence (PLIF) to high pressure H_2/O_2 jet flames for rocket combustion. *Transactions of the Japan Society for Aeronautical and Space Sciences*, in press(xxx).

[129] Takeuchi, K., Nunome, Y., Tomioka, S., Tomita, T., Kudo, T., Hayakawa, A., and Kobayashi, H. (2016b). Development of a water-cooled multi-hole calibration burner for optical measurements of flames with high pressures and temperatures. *Proceedings of the Fifty-Fourth Symposium (Japanese) on Combustion*, 54:23–34.

[130] Tamura, M., Luque, J., Harrington, J., Berg, P., Smith, G., Jeffries, J., and Crosley, D. (1998). Laser-induced fluorescence of seeded nitric oxide as a flame thermometer. *Applied Physics B*, 66(4):503–510.

[131] Thurber, M. C., Grisch, F., Kirby, B. J., Votsmeier, M., and Hanson, R. K. (1998). Measurements and modeling of acetone laser-induced fluorescence with implications for temperature-imaging diagnostics. *Applied Optics*, 37(21):4963–4978.

[132] Thurber, M. C. and Hanson, R. K. (2001). Simultaneous imaging of temperature and mole fraction using acetone planar laser-induced fluorescence. *Experiments in Fluids*, 30(1):93–101.

[133] Unfccc, U. (2015). United nations framework convention on climate change. convention on climate change. http://www.unfccc.de/resource/conv/index.html unfccc. *Forest Science*.

[134] Vaidyanathan, A., Gustavsson, J., and Segal, C. (2009). O_2/H_2 – Planar-Laser-Induced Fluorescence Measurements and Accuracy Investigation in High-Pressure Combustion. *Journal of Propulsion and Power*, 25(4):864–874.

[135] Valera-Medina, A., Marsh, R., Runyon, J., Pugh, D., Beasley, P., Hughes, T., and Bowen, P. (2017). Ammonia–methane combustion in tangential swirl burners for gas turbine power generation. *Applied Energy*, 185:1362 – 1371.

[136] Verkamp, F. J., Hardin, M. C., and Williams, J. R. (1967). Ammonia combustion properties and performance in gas-turbine burners. *Symposium (International) on Combustion*, 11(1):985–992.

[137] Vestin, F., Afzelius, M., Berger, H., Chaussard, F., Saint-Loup, R., and Bengtsson, P.-E. (2007). Rotational CARS thermometry at high temperature (1800 k) and high pressure (0.1–1.55 MPa). *Journal of Raman Spectroscopy*, 38(8):963–968.

[138] Vestin, F., Sedarsky, D., Collin, R., Aldén, M., Linne, M., and Bengtsson, P.-E. (2008a). Rotational coherent anti-Stokes Raman spectroscopy (CARS) applied to thermometry in high-pressure hydrocarbon flames. *Combustion and Flame*, 154:143–152.

[139] Vestin, F., Sedarsky, D., Collin, R., Aldén, M., Linne, M., and Bengtsson, P.-E. (2008b). Rotational coherent anti-stokes Raman spectroscopy (CARS) applied to thermometry in high-pressure hydrocarbon flames. *Combustion and Flame*, 154(1):143 – 152.

[140] Vyrodov, A. O., Heinze, J., Dillmann, M., Meier, U. E., and Stricker, W. (1995). Laser-induced fluorescence thermometry and concentration measurements on NOA–X (0-0) transitions in the exhaust gas of high pressure CH_4/air flames. *Applied Physics B*, 61(5):409–414.

[141] Walker, D. J. W., Williams, R. B., and Ewart, P. (1998). Thermal grating velocimetry. *Optics Letters*, 23(16):1316.

[142] Wang, M., Wang, Z., Gong, X., and Guo, Z. (2014). The intensification technologies to water electrolysis for hydrogen production – a review. *Renewable and Sustainable Energy Reviews*, 29:573 – 588.

[143] Wilhelm, E., Faradjzadeh, A., and Grolier, J. E. (1982). Excess volumes and excess heat capacities of 2,3-dimethylbutane+benzene and + toluene. *Journal of Chemical Thermodynamics*, 1413:1199–1200.

[144] Williams, B. (2009). *Quantitative Laser Diagnostics for Combustion*. PhD thesis, University of Oxford.

[145] Williams, B., Edwards, M., Stone, R., Williams, J., and Ewart, P. (2014). High precision in-cylinder gas thermometry using Laser Induced Gratings: Quantitative measurement of evaporative cooling with gasoline/alcohol blends in a GDI optical engine. *Combustion and Flame*, 161(1):270–279.

[146] Williams, B. and Ewart, P. (2012a). Oxygen concentration effects on laser-induced grating spectroscopy of toluene. *Applied Physics B*, 109:317–325.

[147] Williams, B. and Ewart, P. (2012b). Photophysical effects on laser induced grating spectroscopy of toluene and acetone. *Chemical Physics Letters*, 546:40–46.

[148] Williams, S., Rahn, L. A., Paul, P. H., Forsmant, J. W., and Zare, R. N. (1994). Laser-induced thermal grating effects in flames. *Optics Letters*, 19(21):1681–1683.

[149] Willman, C. (2016). *Laser Diagnostics for Spatially Resolved Thermometry in Combustion and Flows*. PhD thesis, University of Oxford.

[150] Willman, C. and Ewart, P. (2016). Multipoint temperature measurements in gas flows using 1-D laser-induced grating scattering. *Experiments in Fluids*, 57(12):1–9.

[151] Woolf, L. (1991). Thermodynamic Properties of Propanone (Acetone) at Temperatures from 298 K to 323 K and Pressures up to 400 MPa. *J.Chem.Thermodyn.*, 23:867 – 876.

[152] Xu, Z., Tian, X., and Zhao, H. (2017). Tailor-making thermocouple junction for flame temperature measurement via dynamic transient method. *Proceedings of the Combustion Institute*, 36(3):4443 – 4451.

[153] Yano, T., Tomioka, S., Kino, Y., and Nunome, Y. (2016). Laser induced fluorescence thermometry with OH (2 , 0) band excitation. *Journal of Fluid Science and Technology*, 11(4):16–00129.

[154] Zabeti, S., Drakon, a., Faust, S., Dreier, T., Welz, O., Fikri, M., and Schulz, C. (2014). Temporally and spectrally resolved UV absorption and laser-induced fluorescence measurements during the pyrolysis of toluene behind reflected shock waves. *Applied Physics B*, 118(2):295–307.

[155] Zamfirescu, C. and Dincer, I. (2009). Ammonia as a green fuel and hydrogen source for vehicular applications. *Fuel Processing Technology*, 90(5):729 – 737.

[156] Zhao, F.-Q. and Hiroyasu, H. (1993). The application of laser Rayleigh scattering to combustion diagnostics. *Progress in Energy and Combustion Science*, 19(6):447 – 485.

[157] Zhou, B., Brackmann, C., Li, Z., Aldén, M., and Bai, X.-S. (2015). Simultaneous multi-species and temperature visualization of premixed flames in the distributed reaction zone regime. *Proceedings of the Combustion Institute*, 35(2):1409 – 1416.

[158] Zhukov, V. P. and Suslov, D. I. (2016). Measurements and modelling of wall heat fluxes in rocket combustion chamber with porous injector head. *Aerospace Science and Technology*, 48:67–74.

Appendix A

Derivation of Eq. 4.6

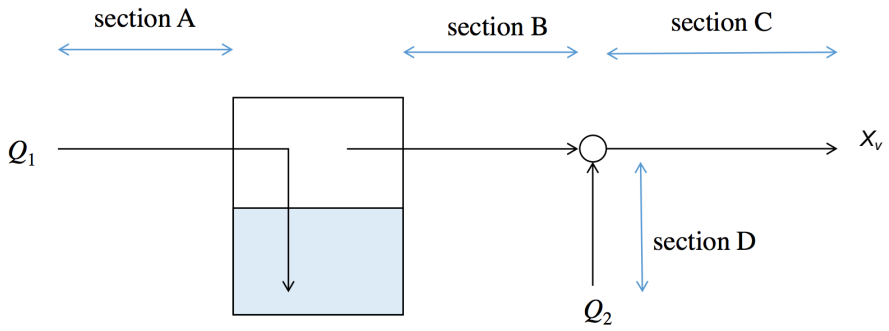

Fig. A.1 Jet layout

The following derivation gives the relationship between the flow rate ratio (ξ) and the target species vapour mole fraction (X_v)(in this case, acetone or toluene) at the exit of the jet used in Chapter 4. Fig. A.1 gives a schematic representation of the bubbler and jet configuration. Sections A and B represent the bubbler inlet and outlet, respectively. Section D represents the dilution line and section C is the jet outlet (i.e. the LITGS measurement location). The flow rate ratio, ξ is defined as:

$$\xi = \frac{Q_1}{Q_1 + Q_2} \tag{A.1}$$

where Q_1 and Q_2 are the volumetric flow rates (m^3/s) at the inlet of the bubbler and the dilution line, respectively.

Nomenclature

Q_1 : Bubbler line air flow rate (m^3/s)
Q_2: Dilution line air flow rate (m^3/s)
Q: volumetric flow rate of air at outlet (sec. C)
$\xi =$: flow rate ratio (-)
X : Mole fraction (-)
Y: Mass fraction (-)
$\dot{m}$: Mass flow rate (kg/s)
P: Pressure (Pa)
T: Temperature (K)
X_v,s Saturated acetone concentration (-)
W: molecular weight (kg/mol)
ρ: density (kg/m^3)
$X_{v,s}$ Mole fraction of vapour at saturated conditions

Suffixes

A : Section A
B: Section B
C: Section C
D: Dilution line
v: vapour (acetone or toluene)
a: air

The air mass conservation before and after dilution is:

$$\dot{m}_{a,B} + \dot{m}_{a,D} = \dot{m}_{a,C} \tag{A.2}$$

Here, by definition, $\dot{m}_{a,A} = \dot{m}_{a,B} = \dot{m}_1$, $\dot{m}_{a,D} = \dot{m}_2$ and $\dot{m}_{a,C} = \dot{m}_a$ Therefore, the conservation of mass of air is:

$$\dot{m}_1 + \dot{m}_2 = \dot{m}_a \tag{A.3}$$

Equation A.3 can be expressed in terms of density and volumetric flow rate as:

$$\rho_{a,A} Q_{a,A} + \rho_{a,D} Q_{a,D} = \rho_{a,C} Q_{a,C} \tag{A.4}$$

Hence,

$$\rho_{a,A} Q_1 + \rho_{a,D} Q_2 = \rho_{a,C} Q \tag{A.5}$$

If the pressure and temperature in the system are constant, the air density is kept constant for all sections. Then, $\rho_0 = \rho_{a,A} = \rho_{a,B} = \rho_{a,C} = \rho_{a,D}$

Hence, Eq. A.5 can be expressed as:

$$\rho_0 Q_1 + \rho_0 Q_2 = \rho Q \tag{A.6}$$

Therefore,

$$Q_1 + Q_2 = Q \tag{A.7}$$

Now, the vapour mass flow rate in section B and section C must be conserved. Therefore:

$$\dot{m}_{v,B} = \dot{m}_{v,C} \tag{A.8}$$

Mass fraction in section B can be expressed by the mass flow rate:

$$Y_{v,B} = \frac{\dot{m}_{v,B}}{\dot{m}_{a,B} + \dot{m}_{v,B}} \tag{A.9}$$

$$\dot{m}_{v,B} = \frac{Y_{v,B}}{1 - Y_{v,B}} \dot{m}_{a,B} \tag{A.10}$$

Since $\dot{m}_{a,B} = \dot{m}_1$,

$$\dot{m}_{v,B} = \frac{Y_{v,B}}{1 - Y_{v,B}} \dot{m}_1 \tag{A.11}$$

The mass fraction of the vapour at section B can also be expressed by the molecular weight and mole fraction:

$$Y_{v,B} = \frac{X_{v,B} W_v}{X_{a,B} W_a + X_{v,B} W_v} \tag{A.12}$$

Substituting Eq. A.12 into Eq. A.11, we have:

$$\dot{m}_{v,B} = \frac{X_{v,B} W_v}{X_{a,B} W_a} \dot{m}_1 \tag{A.13}$$

The mass fraction of vapour in section C is given by:

$$Y_{v,C} = \frac{\dot{m}_{v,C}}{\dot{m}_{a,C} + \dot{m}_{v,C} + \dot{m}_{a,D}} = \frac{X_{v,C} W_v}{X_{a,C} W_a + X_{v,C} W_v} \tag{A.14}$$

From Eq. A.14, $Y_{v,C}(\dot{m}_{a,C} + \dot{m}_{v,C} + \dot{m}_{a,D}) = \dot{m}_{v,C}$, so:

$$\dot{m}_{v,C} = \frac{Y_{v,C}}{1 - Y_{v,C}}(\dot{m}_{a,C} + \dot{m}_a, D) = \frac{Y_{v,C}}{1 - Y_{v,C}}(\dot{m}_1 + \dot{m}_2) = \frac{Y_{v,C}}{1 - Y_{v,C}}\dot{m} \tag{A.15}$$

Substituting Eq. A.14 into Eq. A.15 we obtain:

$$\dot{m}_{v,C} = \frac{X_{v,C}W_v}{X_{a,C}W_a} \tag{A.16}$$

and vapour mass conservation can be expressed as:

$$\frac{X_{v,B}W_v}{X_{a,B}W_a}\dot{m}_1 = \frac{X_{v,C}W_v}{X_{a,C}W_a}\dot{m} \tag{A.17}$$

so,

$$X_{v,C} = \frac{X_{a,C}X_{v,B}}{X_{a,B}}\frac{\dot{m}_1}{\dot{m}} \tag{A.18}$$

Here we assume constant pressure and temperature in the system,

$$\frac{\dot{m}_1}{\dot{m}} = \frac{Q_1}{Q_1 + Q_2} = \xi \qquad \Rightarrow \qquad X_{v,C} = \frac{X_{a,C}X_{v,B}}{X_{a,B}}\xi \tag{A.19}$$

Since $X_{a,C} = 1 - X_{v,C}$ and $X_{a,B} = 1 - X_{v,B}$, substituting and re-arranging yields:

$$\left(1 + \frac{X_{v,B}\xi}{1 - X_{v,B}}\right)X_{v,C} = \frac{X_{v,B}\xi}{1 - X_{v,B}} \tag{A.20}$$

Re-arranging for $X_{v,C}$ and substituting $X_{v,B}$ for $X_{v,s}$ (mole fraction of vapour at saturated conditions), we arrive at:

$$X_{v,C} = X_v = \frac{X_{v,s}\xi}{1 - X_{v,s} - \xi X_{v,s}} \tag{A.21}$$